Seismic Response of Structures on Shallow Foundations over Soft Clay Reinforced by Soil-Cement Grids

Mohammad Khosravi

Dissertation submitted to the faculty of the Virginia Polytechnic Institute and State University in partial fulfillment of the requirements for the degree of

Doctor of Philosophy
In
Civil Engineering

Guney C. Olgun, Chair

Ross W. Boulanger, Co-Chair

Daniel W. Wilson

Joseph E. Dove

Adrian Rodriguez-Marek

Matthew Mauldon

August 4th, 2016

Blacksburg, VA

Keywords: Soil-Cement Grid, Soil Response, Structural Response, Rocking Foundation, Soil-Cement Cracking, Soil-Cement Crushing, Centrifuge Testing, FLAC3D Modeling

Seismic Response of Structures on Shallow Foundations over Soft Clay Reinforced by Soil-Cement Grids

Mohammad Khosravi

ABSTRACT

This study uses dynamic centrifuge tests and three-dimensional (3D), nonlinear finite-difference analyses to: (1) evaluate the effect of soil-cement grid reinforcement on the seismic response of a deep soft soil profile, and (2) to examine the dynamic response of structures supported by shallow foundations on soft clay reinforced by soil-cement grids. The soil profile consisted of a 23-m-thick layer of lightly over-consolidated clay, underlain and overlain by thin layers of dense sand. Centrifuge models had two separate zones for a total of four different configurations: a zone without reinforcement, a zone with a "embedded" soil-cement grid which penetrated the lower dense sand layer and had a unit cell area replacement ratio A_r = 24%, a zone with an embedded grid with A_r = 33%, and a zone with a "floating" grid in the upper half of the clay layer with A_r = 33%. Models were subjected to a series of shaking events with peak base accelerations ranging from 0.005 to 0.54g. The results of centrifuge tests indicated that the soil-cement grid significantly stiffened the site compared to the site with no reinforcement, resulting in stronger accelerations at the ground surface for the input motions used in this study. The response of soil-cement grid reinforced soft soil depends on the area replacement ratio, depth of improvement and ground motion characteristics. The recorded responses of the structures and reinforced soil profiles were used to define the dynamic moment-rotation-settlement responses of the shallow foundations across the range of imposed shaking intensities. The results from centrifuge tests indicated that the soil-cement grids were effective at controlling foundation settlements for most cases; onset of more significant foundation settlements did develop for the weakest soil-cement grid configuration under the stronger shaking intensities which produced a rocking response of the structure and caused extensive crushing of the soil-cement near the edges of the shallow foundations. Results from dynamic centrifuge tests and numerical simulations were used to develop alternative analysis methods for predicting the demands imposed on the soil-cement grids by the inertial loads from the overlying structures and the kinematic loading from the soil profile's dynamic response.

Seismic Response of Structures on Shallow Foundations over Soft Clay Reinforced by Soil-Cement Grids

Mohammad Khosravi

GENERAL ABSTRACT

This study uses dynamic centrifuge tests and three-dimensional (3D), nonlinear finite-difference analyses to: (1) evaluate the effect of soil-cement grid reinforcement on the seismic response of a deep soft soil profile, and (2) to examine the dynamic response of structures supported by shallow foundations on soft clay reinforced by soil-cement grids. The results of centrifuge tests indicated that the soil-cement grid significantly stiffened the site compared to the site with no reinforcement, resulting in stronger accelerations at the ground surface for the input motions used in this study. It was also found from the results of the dynamic centrifuge tests that the soil-cement grids were effective at controlling foundation settlements for most cases; onset of more significant foundation settlements did develop for the weakest soil-cement grid configuration under the stronger shaking intensities which produced a rocking response of the structure and caused extensive crushing of the soil-cement near the edges of the shallow foundations. Results from dynamic centrifuge tests and numerical simulations were used to develop alternative analysis methods for predicting the demands imposed on the soil-cement grids by the inertial loads from the overlying structures and the kinematic loading from the soil profile's dynamic response.

Dedicated to my Mom.

To my mom, my brothers, Ali and Mehdi, and my sister, Elham, whom I love the most.

Mom, you have inspired me the most in my life.

Acknowledgments

This work was supported by the National Science Foundation (NSF) through the George E. Brown, Jr. Network for Earthquake Engineering Simulation (NEESR) under Grant No. CMMI-1208117, Pacific Earthquake Engineering Research Center (PEER), Deep Foundation Institute (DFI), Hayward Baker Inc., Japan Society for the Promotion of Science (JSPS), Disaster Prevention Research Institute (DPRI), Kyoto University, and Key Laboratory of Earthquake and Engineering Vibration, Institute of Engineering Mechanics, CEA, China. Any opinions or conclusions expressed herein are those of the authors and do not necessarily reflect the views of any of the above organizations.

This work would not have been possible without the support and encouragement of many people throughout my 4 years of PhD journey between years 2012 and 2016. First, I'd like to thank my advisors, Prof. Ross Boulanger, Dr Daniel Wilson, and Dr Guney Olgun. I express my most sincere and gratitude to them who trusted me and provided me with this opportunity to work on this project. I am also extremely grateful to Dr Shuji Tamura from Tokyo Institute of Technology, and Dr Lisheng Shao from Hayward Baker Inc., whom I learnt alot during this process.

I am grateful to all staffs and students at the center for geotechnical modeling at UC Davis, who guided me through centrifuge testing, without their help and advice I would not be able to complete the centrifuge tests in less than a year. I would also like to thank the dogs in the center, in particular Haward and Pistol for bringing life and energy to the office.

I'd like to thank Deepak Rayamajhi, graduate researcher form Oregon State University, Yongzhi Wang, visiting researcher from Institute of Engineering Mechanics in China, and Soheil Kamalzareh, PhD candidate from Virginia Tech, for helping me during the centrifuge tests. I'd also like to thank all my friends in Blacksburg and Davis who were my family here, while I was far from my country.

I'd like to thank my mom, I owe her everything that I have in my life. I would also like to thank my other family members, my brothers, Mehdi and Ali, and my sister, Elham, for all they supports in these years.

Mohammad Khosravi,

July 2016

Davis, CA

Table of Contents

1 Introduction

1.1 Background

Soil-cement grids constructed by deep mixing method (DMM), trenching, jet grouting, or other techniques can be an effective method for improving soft soil profiles for support of overlying structures or to reduce potential ground deformations under static or seismic loading. Design issues include the ability of the soil-cement grids to withstand applied forces and stresses without excessive damage and for the composite soil and soil-cement system to limit settlements or deformations to acceptable levels. Design methods for soil-cement grids, as structural foundations or slope reinforcements, are not as well developed for seismic loading conditions as those for static loading conditions.

Case histories from past earthquakes have shown that ground reinforcement can be an effective method for mitigation of earthquake-induced ground displacements. Soil-cement grids were, for example, found to have been effective in reducing earthquake damages during the 1995 Kobe earthquake (Tokimatsu et al., 1996, Suzuki et al. 1996). Tokunaga et al. (2015) evaluated the performance of a total number of 789 sites treated by soil-cement reinforcement with different configurations (block, grid, wall, and column types) after the 2011 Tohoku earthquake, and found that the soil-cement reinforced facilities experienced no significant damage during the earthquake.

Dynamic centrifuge model tests have been used to investigate the effects of soil-cement ground reinforcement on earthquake-induced settlements or other ground failure modes in soft or liquefiable soils (Almeida et al. 1985, Babasaki et al. 1991, 1992, Miyake et al., 1991, Kitazume et al., 1996, 2000, Adalier et al., 1998, Hausler et al., 2002, Kitazume and Maruyama, 2006, Takahashi et al., 2006, Ishikawa and Asaka, 2006, Takahashi et al., 2009, Rayamajhi et al., 2014b,c, Rayamajhi et al., 2015, Karimi and Dashti, 2015a,b). In all of these studies, prefabricated soil-cement or acrylic grids have been used. Babasaki et al. (1991 and 1992), O' Rourke and Goh (1997), and Takahashi and Kitazume (2006) illustrated the importance of grid spacing on maximum excess pore pressure ratios. Takahashi et al (2006) examined the role of shaking intensity and depth of reinforcement

in design of soil-cement grids. The importance of an external stability analysis of the reinforced zone (e.g. sliding, overturning or bearing failures) when a floating soil-cement grid is used underneath an embankment slope was demonstrated in tests by Matsuo et al. (1996), Adalier et al. (1998), and Kitazume and Terashi. (2014).

Numerical analyses have been used to evaluate overall deformation mechanisms and critical aspects of the seismic response of soil-cement reinforced soil deposits subjected to strong ground shaking, including 2D analyses (Babasaki et al. 1991, O' Rourke and Goh 1997) and 3D analyses (Fukutake and Ohtsuki 1995, Namikawa et al. 2007, Bradley et al. 2013, Nguyen et al. 2013, Puebla et al. 2006). These studies illustrated the importance of area replacement ratio (A_r = area of soil-cement divided by total area), depth of improvement, and stiffness of the improved soils on the response of the enclosed soil. Some studies also indicated that grid improvement caused an increase in amplitude of the surface ground motion which would result in higher inertial loading for the overlying superstructure in comparison to the unreinforced soil profile (Bradley et al. 2013). Namikawa et al. (2015) investigated the dynamic behavior of soil-cement grid reinforcement and observed concentrated tensile stress at the corner and mid-length of the soil-cement walls. Namikawa et al. (2007) found that partial failure of the improved ground was not critical in the provided level of liquefaction mitigation. Numerical analyses have also been used to develop simplified analysis methods for preliminary design (Nguyen et al., 2013, Rayamajhi et al., 2014a).

Current allowable stress based design procedures (e.g., Bruce et al., 2014) do not explicitly allow partial damage to the soil-cement grid system. Allowable stress design procedures focus on the ability of the soil-cement grid reinforcement to withstand applied forces and stresses without excessive damage. The effect of partial damage and cracking of soil-cement grids on their ability to limit settlements or deformations to acceptable levels has not been well studied. This consideration requires an evaluation of the composite behavior of the grid reinforced soil and the internal distribution of stresses and strains that would develop during shaking. The limited experimental and case history data do not provide sufficient information to quantify the shear reinforcement mechanisms of soil-cement grids in soft or liquefiable soils during strong earthquake loading.

In this study, a series of dynamic centrifuge model tests combined with 3D nonlinear finite difference numerical modeling are conducted to examine: (1) the effect of soil-cement grid reinforcement on the seismic response of a deep, lightly over-consolidated clay profile, (2) the dynamic response of structures supported by shallow foundations on soft clay reinforced by soil-cement grids, and (3) the effect of partial damage and cracking of soil-cement grids on their ability to limit settlements or deformations. The results of the experiments and analyses provide insight on the dynamic performance of soil-cement grids and an archived dataset for evaluating design procedures.

1.2 Objectives

In this study, the current challenges in seismic design of soil-cement ground reinforcement has been addressed which include:

1. The effect of soil-cement ground reinforcement on seismic behavior of soft soils;

   Bradley et al. (2013) studied the response of soil-cement grid reinforced liquefiable soil using 3D finite element analysis and showed that ground improvement caused an increase in amplitude of the surface ground motion. This would result in higher inertial loading for the overlying superstructure for short to moderate vibration periods of the ground motion. In this study, the effect of different types of soil-cement ground reinforcement (e.g. grid, and column) on seismic response of soft and liquefiable soils is investigated using dynamic centrifuge modeling.

2. The seismic response of a structure located on a soft clay site reinforced by soil-cement grid reinforcement;

   Rocking foundations have been recently proposed as an alternative seismic design philosophy for bridges or buildings (Anastasopoulos et al. 2012, Deng et al. 2014). Since Housner (1963), many researchers have investigated the advantages and disadvantages of using rocking foundations, as well as methods of predicting their behavior and performance. The benefits of the rocking mechanism are the natural re-centering tendency, well-defined moment capacity, significant energy dissipation which reduces damaging ductility demand of the super-structure (Anastasopoulos et al. 2010, Gajan et al. 2010, Gajan et al. 2005, Deng and Kutter 2012, Anastasopoulos et

al. 2012, Allmond and Kutter 2013). One concern of rocking foundation systems is the potential for significant accumulation of settlement or residual rotations in poor soil condition (e.g., submerged, soft, or liquefiable soil). Studies have suggested that ground improvement can help control settlements (Deng and Kutter 2012, Anastasopoulos et al. 2012, Allmond and Kutter 2014). In this study, centrifuge tests were conducted to examine the dynamic responses of structures over soil-cement grid including moment-rotation-settlement responses of the shallow foundations; and damaged patterns in the soil-cement grids and their relationship with footing settlements. The results are used to evaluate alternative analysis methods for predicting the demands imposed on soil-cement grids by overlying structures.

3. Possible effect of partial damage to the soil-cement grid reinforcement on its ability to withstand applied forces and stresses;

Damage to the soil-cement grid could be caused either due to excessive shallow foundation contact stresses which develop under the inertial loads from the overlying structure or excessive dynamic kinematic loads which develop because of the stiffness contrast between the grid and surrounding soils. Currently available experimental and case history data do not provide sufficient information to quantify the possible effects of partial damage to the soil-cement grids on their ability to limit the shallow foundation settlements. In this study, methods for analyzing these loading cases are evaluated for their ability to distinguish between the occurrence and absence of crushing or cracking of the soil-cement grids.

1.3 Overview and outline

Chapter 2 describes the centrifuge model construction procedure for a soft clay profile reinforced by soil-cement grids and presents the results and observations of seismic site response during a preliminary dynamic centrifuge test. The tests presented in this chapter involved soft clay profiles with and without grids carried out with a 1-m radius centrifuge at the UC Davis Center for Geotechnical Modeling. The small centrifuge tests provided a basis for refining the design and establishing the model construction procedures of the larger and more detailed models to be tested on the 9-m radius centrifuge in the next phase of this study. The centrifuge models and testing programs are described, followed by a

discussion of the soil-cement mixture design and the soil-cement grid construction process. Finally, some preliminary results focusing on the reinforcing effects of the grids as reflected in the acceleration, pore pressure generation and settlement responses of both unreinforced and reinforced soil profiles are presented.

Chapter 3 describes the large centrifuge model construction procedure for a soil-cement grid supporting a structure over soft clay and the system's dynamic response to shaking motions of varying intensity. The test showed that centrifuge models of soil-cement grid reinforced soil could be constructed using trenching and excavation technique and the results could be used to examine system-level performance, including the effects of grid cracking. In the next part of this chapter, a new crack detection mechanism and its validation process in centrifuge testing to estimate the formation of cracks in soil-cement ground reinforcement is discussed and investigated in more details. The issue of concern was how cracking patterns observed in the soil cement panels could be related to the imposed shaking and response of the structure.

Chapter 4 summarizes results of dynamic centrifuge model tests examining the effect of soil-cement grid reinforcement on the seismic response of a deep, lightly over-consolidated clay profile. The effects of the soil-cement grids on the nonlinear dynamic responses of the soil profile and the internal interactions between the soil-cement grids and enclosed soils are examined using (1) time series of accelerations, shaking-induced excess pore water pressures, and post-shaking reconsolidation settlements, (2) response spectra and spectral ratios, (3) back-calculated composite stress-strain responses, (4) analyses of internal stress distributions between the grids and enclosed soils, and (5) dynamic crack detections and post-test crack mapping in the soil-cement grids. The results of these experiments and analyses provide insights on the dynamic performance of soil-cement grids and the internal interactions between the grids and enclosed soils. These results were used to develop a simplified procedure to evaluate potential for tensile stresses and cracking in the longitudinal soil-cement walls.

Chapter 5 summarizes results of centrifuge model tests examining the dynamic response of structures supported by shallow foundations on soft clay reinforced by soil-cement grids. The models were designed to examine the ability of the soil-cement grids to

limit settlement of the shallow foundations even when the dynamic loading causes significant damage to the soil-cement grids. The dynamic responses of the structures and reinforced soil profiles are described, including the dynamic moment-rotation-settlement responses of the shallow foundations across the range of imposed shaking intensities. Damage to the soil-cement grids, which included extensive crushing near the edges of the shallow foundations and minor cracking at larger depths for the weakest soil-cement grid at the strongest shaking intensities, is described and related to the observed foundation settlements. Alternative analysis methods for predicting the demands imposed on the soil-cement grids by the inertial loads from the overlying structures and the kinematic loading from the soil profile's dynamic response are evaluated for consistency with the observed damage patterns.

Chapter 6 describes three-dimensional nonlinear finite difference analyses of a series of dynamic centrifuge tests investigating the response of structures supported on shallow foundations on a soft soil foundation layer treated with soil-cement grids. The analysis parameters were validated using the rocking response of structures, and performance of the soil-cement grid during dynamic centrifuge tests. The validated model was then used to perform a parametric evaluation of relevant terms to (1) evaluate and validate model ability to estimate stress distribution and damage in the soil-cement grid due to stresses imposed due to rocking foundation; and (2) evaluate the parameters that control stress distribution from the top sand layer to the grid and its surrounding soil beyond those covered in centrifuge tests. The results were used to develop a simple design model for estimating stress transfer for rocking foundation from the sand layer to the top of soil-cement grid. This guidance with combination with the knowledge of the strength of the soil-cement grid give an estimate of if damage to the soil-cement grid is expected.

Chapter 7 summarizes the dissertation with the significance of the work and future prospects.

2 Dynamic Centrifuge Tests on Soft Clay Reinforced by Soil-Cement Grids

This chapter is produced from two conference papers, Khosravi et al. 2015 (With permission from ASCE), and Tamura et al. 2015. First paper was presented in the International Foundations Congress and Equipment Expo 2015 in San Antonio, TX, and the second one was presented in 6th International Conference on Earthquake Geotechnical Engineering (6ICEGE) in Christchurch, New Zealand.

Khosravi, M., Tamura, S., Boulanger, R. W., Wilson, D. W., Olgun, C. G., Rayamajhi, D., Wang, Y. (2015). "Dynamic Centrifuge Tests on Soft Clay Reinforced by Soil-Cement Grids." *IFCEE 2015*, 2349-2358.

Tamura, S., **Khosravi, M.,** Boulanger, R.W., Wilson, D. W., Olgun, C.G., Rayamajhi, D., Wang, Y. (2015). "Seismic response of Soft Clay Reinforced by Soil-Cement Grid Based on Dynamic Centrifuge Tests", *6ICEGE*, Christchurch, New Zealand.[1]

Abstract. This chapter describes the centrifuge model construction procedure for a soft clay profile reinforced by soil-cement grids and presents the results and observations of seismic site response during a preliminary dynamic centrifuge test. These tests are the first in a series of centrifuge tests investigating the stiffening effect of soil-cement grid reinforcement on the seismic response of soft clay sites. The results showed that for high intensity base motions, soil nonlinearity reduced the soil peak horizontal acceleration (PHA) in an unreinforced soil profile, while in a reinforced profile, the surface PGA was greater than the base peak acceleration. The soil-cement grid with A_r=30% and Improvement Depth / Grid Spacing = 0.7 did not help reduce the induced excess pore water pressure and settlement in the surrounding soil. However, the settlement of the soil-cement grid was significantly smaller than the surrounding soil settlement.

Keywords: small centrifuge test; soil-cement grid; dynamic response of clay; soil-cement cracking.

[1] Mohammad Khosravi conducted all the tests, and performed all data analysis, and was involved in review process.

2.1 Introduction

Mitigation of earthquake damage potential at soft soil sites remains a challenge in earthquake engineering. Earthquake damage potential at soft soil sites can be reduced by reinforcing them to support overlying structures, increase their composite shear strength, or reduce the seismic stresses and strains in the enclosed soils (e.g., using stone columns, cement soil mixing, jet grouting), or by removing and replacing the soft soils with competent soils (Mitchell 2008).

Soil-cement grids constructed by deep mixing method (DMM), jet grouting, or other methods can be an effective ground reinforcement technique for reducing earthquake damage potential. Few studies in the literature have documented the effect of soil-cement reinforcement on seismic response of soft clay sites. Previous studies on soil-cement reinforcement include case histories of field performance (Hausler and Sitar 2001), centrifuge tests (Babasaki et al. 1991), numerical analyses (Babasaki et al. 1991, Namikawa et al. 2007), and state-of-practice reports (Porbaha et al. 1998). These studies illustrate the beneficial effects of soil-cement ground reinforcement on reducing settlements or other ground failure modes in soft or liquefiable soils.

This chapter describes the preliminary stages of a study to investigate the reinforcing mechanisms of soil-cement grids in soft soils using dynamic centrifuge testing. The tests presented herein involved soft clay profiles with and without grids carried out with a 1-m radius centrifuge at the UC Davis Center for Geotechnical Modeling. The small centrifuge tests provided a basis for refining the design and establishing the model construction procedures of the larger and more detailed models to be tested on the 9-m radius centrifuge in the next phase of this study. The centrifuge models and testing programs are described, followed by a discussion of the soil-cement mixture design and the soil-cement grid construction process. Finally, some preliminary results focusing on the reinforcing effects of the grids as reflected in the acceleration, pore pressure generation and settlement responses of both unreinforced and reinforced soil profiles are presented.

2.2 Small Centrifuge Test Program

A series of small centrifuge model tests was performed in a "flexible shear beam container" (FSB). The inner dimensions of the container in prototype scale were 24.7 m

length, 11.8 m width, and 9.0 m height. All the models were tested at a 50g gravitational acceleration field. All data are presented in prototype units unless otherwise specified. The numeric quantities within this chapter have been converted into prototype units according to the scaling laws described by Schofield (1981) and Kutter (1995).

In the first test, the model soil profile was subjected to a series of small to medium intensity shaking events (Model 1) to establish the baseline untreated response. The same soil profile was then reinforced with soil-cement panels and was further subjected to a similar series of ground motions in the second test (Model 2).

The soil profile consisted of 6-m thick layer of coarse kaolinite (Hydrite Flat DS, manufactured by the Imerys Company) underlain by 1-m thick saturated dense sand (Dr≈90%) for drainage purpose. Properties of the kaolinite include (Stringer et al. 2012): Liquid Limit, LL = 47; Plastic Index, PI = 19; specific gravity of solids, $G_s = 2.58$; median particle size of 4.0 μm; and a coefficient of consolidation, $C_v = 0.7$ mm2/s in virgin loading and 2.3 mm^2/s in unloading/reloading.

The clay profile was constructed in two lifts. First, the clay was batch-mixed in a small vacuum mixer at an initial water content of approximately 80%. Each lift was then placed and pre-consolidated in a press with the vertical pressure equivalent to self-weight at the bottom of the layer at 50g. This made the clay layer slightly overconsolidated on average. The pre-consolidation stage significantly reduced the settlement and the time required for in-flight consolidation compared to starting from a slurry. A thin layer of wet sand was placed on the surface to prevent drying of the clay surface during spinning.

Models were instrumented with accelerometers (ICP), pore pressure transducers (PPTs), and linear potentiometers (LPs). Two PPTs (PPT-1 & PPT-2) were placed in the clay to record the pore water pressure generated during the tests. Two LPs (LP-1 and LP-2) were used to record ground surface settlement in both tests. Two LPs (LP-3 and LP-4) were added in reinforced cases to record soil-cement column settlements. One accelerometer (ICP-7) was used in all models to compare the response of the FSB container with the clay profile. Instrumented model layouts of the unreinforced test model and

reinforced test model with area replacement ratio (A_r) of 30% within the reinforced area is presented in Figure 2.1.

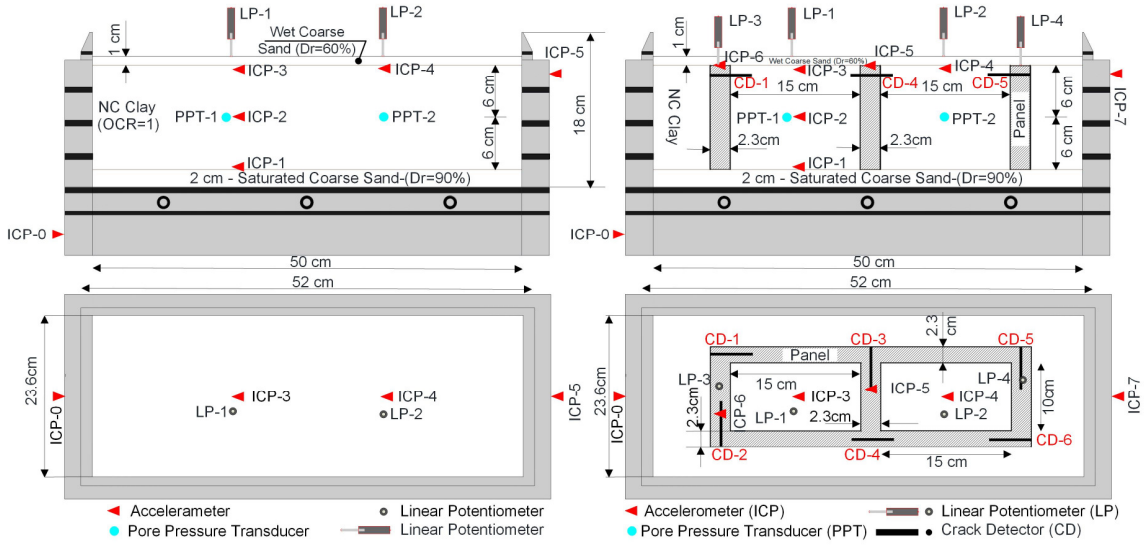

(a) Model 1 **(b) Model 2**

Figure 2.1. Model Layouts of: (a) Unreinforced Model Test, (b) Reinforced Model Test with Soil-Cement Grid and Ar = 30% (dimensions are in model scale)

2.2.1 Soil-Cement Mixture

A soil-cement mixture with reasonable strength, workability, and initial setting time had to be developed in order to perform the experimental research program. One of the most important parameters in the design of soil-cement mixture is the strength of the soil-cement. The critical factors influencing the strength gain of the soil-cement mixture are: 1) type of cement, 2) soil-cement-water ratio, 3) temperature, and 4) curing environment (e.g., Bruce et al. 2013). A high early strength cement was used for the soil-cement mixture to reduce the initial curing time, which was only 24 to 72 hours, depending upon temperature and the soil-cement-water ratio.

Two candidate mixtures with different water-soil ratios but similar water/cement ratios were evaluated (Table 2.1). Unconfined Compressive Strength (UCS) tests were performed on soil-cement specimens and the results are presented in Figure 2.2. Unconfined compressive strengths in the range of 400 to 700 kPa were obtained in 7 days (curing time). It can be seen in Figure 2.2 that the unconfined compressive strengths of the two mixtures are close as the water-cement ratio is similar (Table 2.2). Increasing the water-soil ratio in

Mix 2, however, increased the workability of the soil-cement mixture and minimized internal and surface voids at interface between the soil and the panels (Figure 2.3) in the constructed specimen. It also postpones the initial setting time, which facilitates instrument placement on and inside the soil-cement panels. Therefore, Mix 2 selected as the soil-cement mixture for the centrifuge tests.

Table 2.1. Soil Cement Mixtures

Mix No.	Mixture (parts by weight) Cement : Clay : Water
M1	1.0 : 2.5 : 3.0
M2	1.0 : 1.9 : 3.1

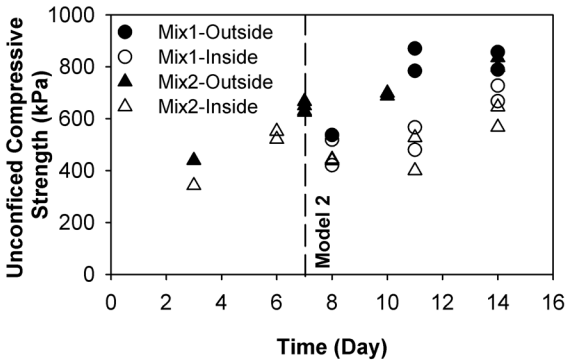

Figure 2.2. Unconfined Compressive Test Results For Two Candidate Mixes Cured Inside Clay Model and Outside in Plastic Mold

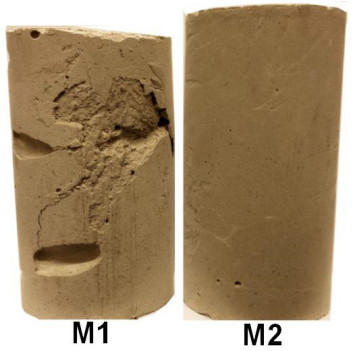

Figure 2.3. Two Candidate Soil-Cement Mixture Showing the Effect of Workability

Two series of cylindrical soil-cement samples were prepared to investigate possible effects of curing environment on the soil-cement strength: 1) cylindrical samples cast and cured in a plastic mold outside the clay profile (Figure 2.3), and 2) cylindrical samples cast and cured inside a clay profile (Figure 2.4), which better represents the curing environment expected for the centrifuge tests. UCS test results showed that strength of the samples which were cured within the clay model were 20-30% less than those prepared and cured outside the clay which could be attributed to the effect of humidity and temperature (Figure 2.2). This suggests that to achieve a specific strength in the model, the curing time should be increased as the soil-cement grids are cast in place in the centrifuge models.

2.2.2 Soil-Cement Panel Construction

One challenge for the centrifuge model tests was the soil-cement grid construction. In the soil-cement grid reinforcement, transfer of loads between panels requires a proper

connection linking perpendicular elements. Connections are critical to the integrity of a grid type of soil-cement ground reinforcement. Two different approaches were investigated for construction of the grids in the clay model, 1) Auger Soil Mixing Method (Figure 2.5), and 2) Trench and Excavation Method (Figure 2.6).

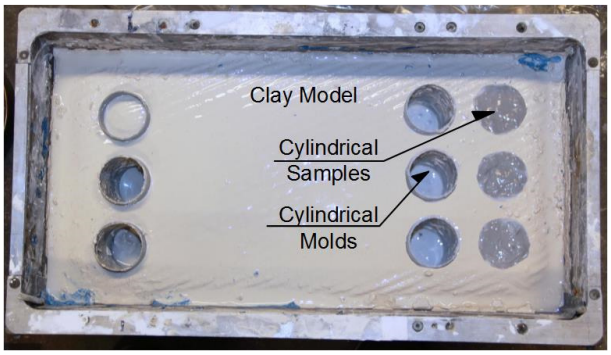

Figure 2.4. Prepared Soil-Cement Samples Cast Inside Clay Model for UCS Tests

In the first approach, the panel was constructed using an auger driven by a hand drill. Primary holes were spaced horizontally at 5 cm to prevent disturbing the holes during excavating the adjacent holes. The primary holes were filled with soil-cement slurry and allowed to cure. Secondary holes were then constructed in between and overlapping with the primary holes to form interlocking joints (Figure 2.5). This approach suffered from two main problems. It is shown in Figure 2.5(a) that the disturbance of the primary holes during drilling the secondary holes happened even after the soil-cement slurry obtained significant strength. Moreover, it is shown in Figure 2.5(b) that the thickness was not uniform along the depth of the panel, with thickness about 40% higher at upper levels.

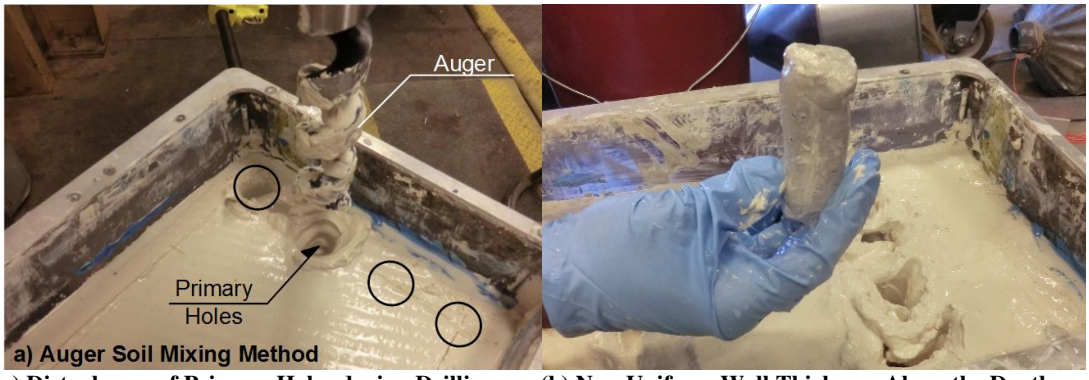

(a) Disturbance of Primary Holes during Drilling Secondary Holes **(b) Non-Uniform Wall Thickness Along the Depth**

Figure 2.5. Method 1: Auger Soil Mixing

In the second approach, two thin stainless steel plates were inserted into a clay layer at specified spacing equal to the required thickness for the soil-cement panels. The metal

sheets were tied together either by spacers or studs to strengthen them laterally. Excavation was performed with spatula and spoon. Once sufficient excavation was complete, the excavation was filled with soil-cement slurry and the metal sheets were removed (Figure 2.6). Using this approach a good connection between the two perpendicular panels was obtained. Therefore, the soil-cement grids in the centrifuge test model were constructed using Trench and Excavation method.

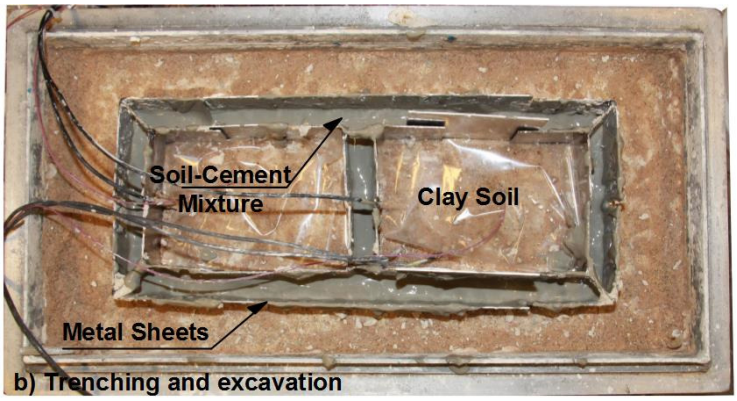

Figure 2.6. Method 2: Trenching and Excavation

2.3 Dynamic Response of Centrifuge Models

The effect of reinforcement on the seismic response of a soft clay site was studied by comparing the dynamic responses of an unreinforced (Model 1) and a reinforced (Model 2) soil profile. Both models were shaken with the same sequence of shaking events consisting of sine sweep motion, earthquake motions of varying intensity (Peak Base Acceleration of 0.036g - 0.54g) and frequency. The sine sweep motions contained continuously varying frequencies between 1 and 7 Hz (progressing from lower to higher frequencies). The earthquake motions were scaled versions of the recordings at station TCU-078 during the 1999 Chi-Chi earthquake. Model 2 were also subjected with a series of strong sine motions to investigate the effects of soil-cement damages on the site response. Nonlinearities in the dynamic responses and interaction mechanisms are examined using (1) time series of accelerations, shaking-induced excess pore water pressures, and post-shaking reconsolidation settlements, (2) response spectra and spectral ratios, and (3) dynamic crack detections and post-test crack mapping in the soil-cement grids.

2.3.1 Small sine sweep motion

The recorded responses from the sine sweep motions were used to evaluate the natural periods of the system at low levels of shaking. Peak base accelerations (PBA) were 0.007 g and 0.008 g for Models 1 and 2, respectively. The sine sweep motion contained thirty frequencies between 1 to 7 Hz and 7 cycles of each frequency.

Spectral amplification ratios for Models 1 and 2 during sine sweep motion are shown in Figure 2.7. The spectral amplification ratios are the spectra (linear elastic, 5% damping, pseudo spectral acceleration) for motions recorded near the ground surface divided by those for the base motion. The responses of the unreinforced soil and the soil inside the grid were all similarly amplified relative to the base motion at all periods. The natural periods of the clay layers for Models 1 and 2 were 0.36 s and 0.32 s, respectively. The estimated shear wave velocities estimated based on the natural periods (T) and the formula $T=4\times H/V_S$ (where H = clay layer thickness and V_S = shear wave velocity) for Models 1 and 2 were 67 m/s and 75 m/s, respectively. The average shear wave velocity of the clay layer with the soil-cement grid was 12% higher than what estimated in the unreinforced clay layer.

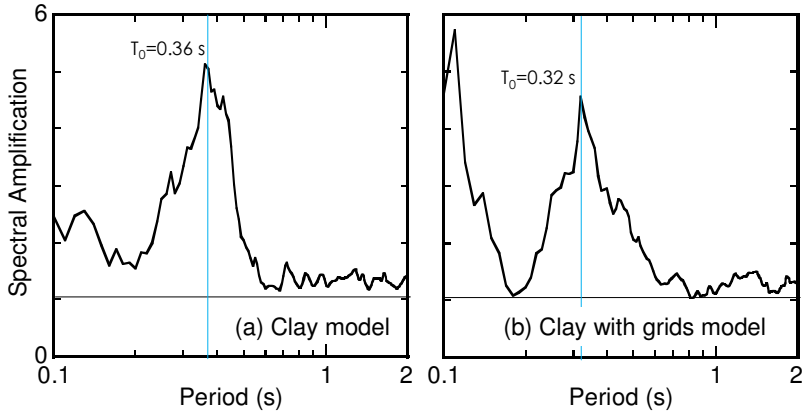

(a) Model 1 **(b) Model 2**

Figure 2.7. Spectral amplification factors for a small sine sweep motion

2.3.2 Chi-Chi motion with PBA = 0.06 g

The effect of soil-cement grid reinforcement on the seismic response of soft soil during small shaking events was investigated with TCU (Chi-Chi) motion with a peak base acceleration (PBA) of = 0.06 g for Model 1 and 0.04g for Model 2. The acceleration

response of the unreinforced soil (Model 1), and the soil-cement grid reinforced model (Model 2) are presented in Figure 2.8. Figure 2.8 displays motions recorded near the ground surface on the unreinforced soil, on the mid points of the transverse walls of the grid, the soil inside the grid cells, and the base motion (base). Both unreinforced (Model 1) and reinforced (Model 2) soil surfaces had a PHA = 0.09g producing amplification ratios of 2.4 and 1.5, respectively. The waveforms of accelerations recorded on the soil inside the grid, and on the mid points of the transverse walls of the grid in Model 2 were similar, indicating that the clay response was affected by the soil-cement grid.

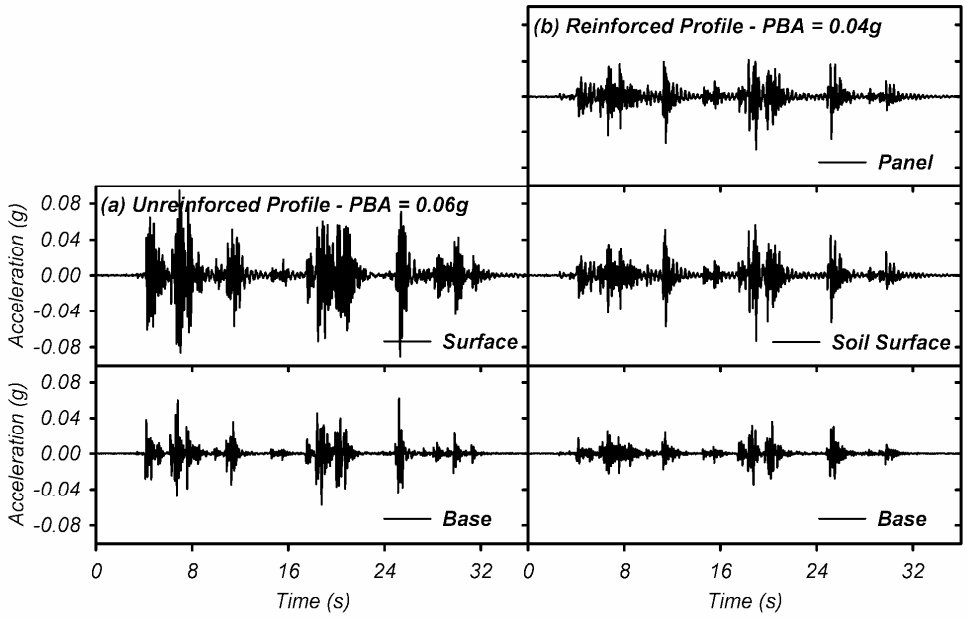

(a) Model 1 **(b) Model 2**

Figure 2.8. Time histories of the input motion and the motion at the clay surface and top of the soil-cement grid for a small Chi-Chi motion

Spectral amplification ratios for Models 1 and 2 during small TCU motions (PBA of 0.04-0.06g) are shown in Figure 2.9. The natural periods of Models 1 and 2 were 0.48 s and 0.34 s, respectively. The estimated average shear wave velocity of the clay profile for Model 1 was 50 m/s, which was 25% less than what estimated during the small sine sweep motion. For Model 2, the estimated average shear wave velocity of the reinforced soil was 71 m/s, which was almost the same as the initial shear wave velocity. This suggests that the soil-cement grid reduced the dynamic stresses and strains imposed on the enclosed soil at this low shaking level. The other major peak in spectral amplification ratio for Model 1 was 0.16s, corresponding to 1/3 of the natural period. Therefore, this peak is the 1st higher

mode. The 1st higher mode period for Model 2 was about 0.13 s. The amplification factor at the natural period for Model 2 was about half of the one for Model 1. This is consistent with the fact that the impedance contrast of Model 2 is small as the soil-cement grid mitigate the reduction of the shear wave velocity of the clay layer during the shaking. On the other hand, the amplification factor at the 1st higher mode period for Model 2 was 50% higher than in Model 1 in spite of the small impedance contrast. The red dotted line in Figure 2.9 shows the spectral amplification factors between the top of the soil-cement grid and the sand base layer for Model 2. The amplification factor of the soil-cement grid, which is similar to the clay layer, is higher near the 1st higher mode period. This suggests that the soil-cement grid increased the clay site amplification at the 1st higher mode period.

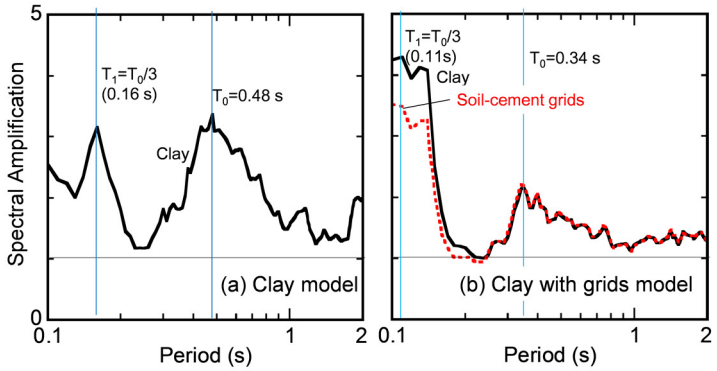

(a) Model 1 **(b) Model 2**

Figure 2.9. Spectral amplification factors for a small Chi-Chi motion

2.3.3 Strong Chi-Chi motion

The dynamic responses of the clay models during a TCU motion with a peak base acceleration (PBA) of 0.43g for Model 1 and 0.31 for Model 2, are presented in Figure 2.10. The peak horizontal accelerations (PHA) were deamplified through the unreinforced soil profile by 46%, reaching a value of 0.23g at the soil surface in Model 1. In Model 2, however, the PHA on the soil surface was 0.39g, 26% greater than the PBA. Overall, the presence of the grids in Model 2 increased the PHA at the ground surface.

The excess pore water pressure (EPWP) within the clay layer (see Figure 2.1) reached peak values of 15 kPa and 13.5 kPa at 3.5 m depth in Model 1 and Model 2, respectively. The EPWPs began dissipating after the end of shaking, with the dissipation being faster in Model 2 than in Model 1. The faster rate of dissipation for Model 2 could be due to preferential seepage paths which might have formed along the sides of the panels or due to

stiffness contrast between the soft soil and soil-cement panels, which can accelerate pore pressure dissipation by transferring vertical loads from the soft clay to the panels during consolidation. The average soil surface settlements were about 5.7 cm in Model 1 and 5.6 cm in Model 2. The occurrence of almost similar EPWP and settlement in Model 2 despite having lower PBA value comparing to Model 1 suggests that the soil-cement grid with A_r = 30% and Improvement Depth/Grid Spacing = 0.7 did not help reduce the peak EPWP or settlement in the surrounding soil (Figure 2.10). However, the settlement of the soil-cement grid (average of 0.7 cm) was significantly smaller than the surrounding soil settlement of 5.6 cm. This would be expected to significantly reduce the vertical settlement of any superstructure located on the grids.

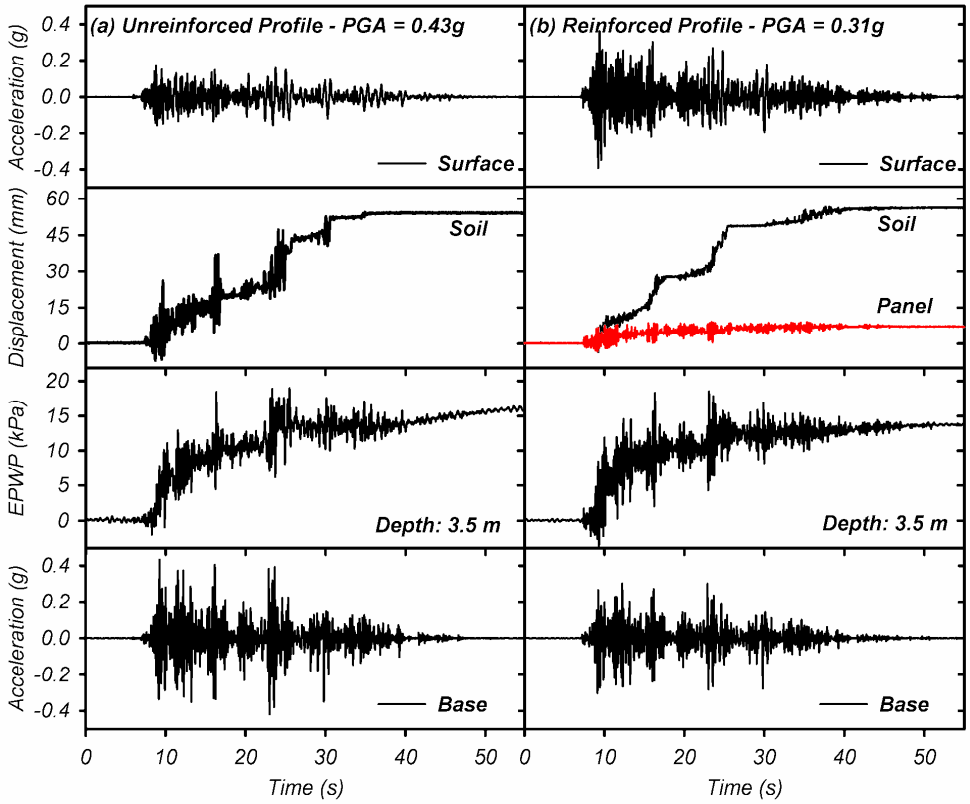

Figure 2.10. Recorded Time Histories in Unreinforced and Reinforced Soil Sites

Spectral amplification ratios for Models 1 and 2 during TCU motion with a peak base acceleration (PBA) of 0.43g for Model 1 and 0.31 for Model 2, are presented in Figure 2.11. The natural period for Model 1 was 1.17 s. The estimated shear wave velocity was 21 m/s. This is attributed to the soil-cement grids stiffening the soil profile and thereby reducing induced shear strains and soil nonlinearity. The natural period for Model 2 was

not clear. The amplification factor at the natural period for Model 1 was higher than that for Model 2, because of the high impedance contrast. The amplification factor at the 1st higher mode period for Model 1 was small, probably because the effect of the soil damping was dominant for the short periods.

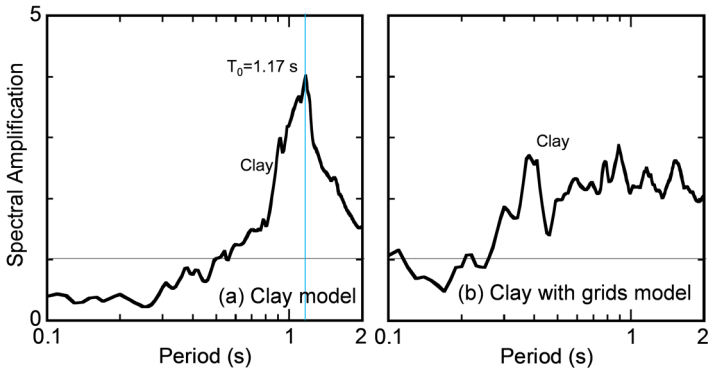

(a) Model 1 **(b) Model 2**

Figure 2.11. Spectral amplification factors for a large Chi-Chi motion

Acceleration response spectra (linear elastic, 5% damping, pseudo spectral acceleration) for TCU motion with a peak base acceleration (PBA) of 0.43g for Model 1 and 0.31 for Model 2 are shown in Figure 2.12 to clarify the reason why the PGA for Model 1 was smaller than for Model 2 in spite of the larger amplification factor at the natural period. Spectra for motion on the transverse wall in Model 2 is also shown in Figure 2.12b. The predominant period of the base layer motions for both models were about 0.15-0.3 s. The amplification factor for Model 2 was about 0.6-1.8 at the predominant period as shown in Figure 2.11(b). In contrast, the amplification factor for Model 1 was less than 0.5 at the predominant period; this difference is attributed to greater soil nonlinearity and higher soil damping. Therefore, the PGA for Model 1 was smaller than that for Model 2.

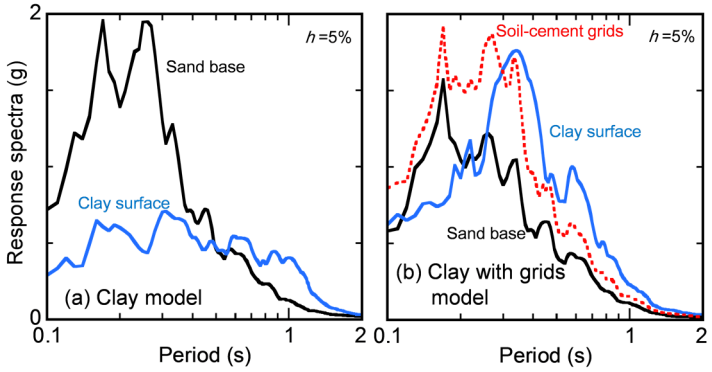

(a) Model 1 **(b) Model 2**

Figure 2.12. Pseudo acceleration response spectra for a large Chi-Chi motion

Acceleration time histories of base (over base sand layer), surface of soil inside soil-cement grid, and transverse soil-cement wall for a time span of 2 seconds (t=1-3 s) are shown in Figure 2.13. The acceleration response of soil surface and soil-cement wall were similar until t = 2.1 s when the base acceleration amplitudes were small. The soil-cement grid response tended to be faster than the clay response after t=2.1 s, indicating that seismic waves propagated through the soil-cement grid. Additionally, the spectral acceleration response of the soil inside the grid was more similar to the response of soil-cement grid than the response of the base layer, especially at periods smaller than 0.3 s (Figure 2.12b). These suggest that the clay surface response consisted of seismic waves propagating not only in the clay layer but also in the soil-cement grid, as illustrated in Figure 2.14. This is consistent with the fact that the clay layer with the soil-cement grid does not have a clear natural period. The seismic wave didn't propagate well through the soft clay layer because of its high damping at the short period.

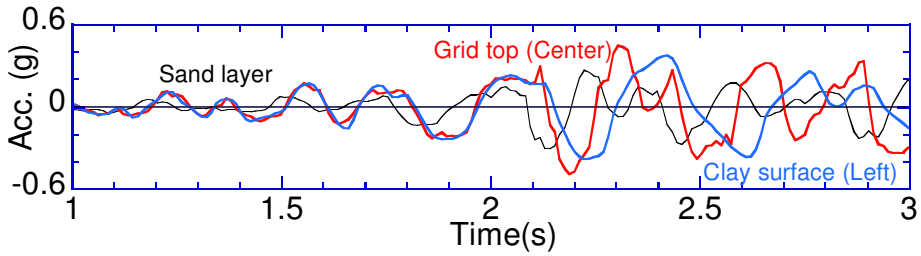

Figure 2.13. Time histories of sand layer, clay surface and grid

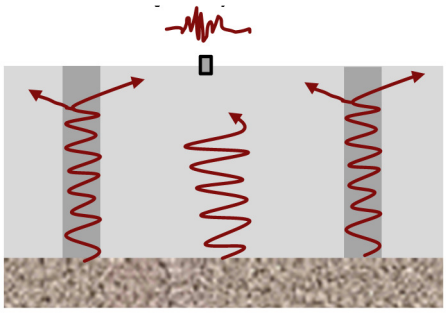

Figure 2.14 Seismic waves propagating clay with the grid

2.4 Soil-Cement Panel Performance

To investigate the effect of partial damage of the soil-cement grid on the response of soft soil reinforced with soil-cement grid, Model 2 was shaken with a series of strong sine motions with frequency of 2 Hz and PBA=1.0 g. Figure 2.15 shows the displacement time histories of the soil surface inside the grid and soil-cement grid. The displacements were

estimated by double integration of acceleration. Based on results from crack detectors, Crack-S and Crack-N (Figure 2.16a) occurred at t = 9 s and t = 14 s, respectively. No considerable change in displacements of soil, and grid were observed after cracking of Crack-S. When soil-cement grid experienced cracking in Crack-N location, the displacement amplitudes of the soil-cement grid increased but no change in displacement amplitude of soil was observed. The above responses indicate that cracking at one side of the wall did not affect the wall displacement. Cracking at both edges of the wall increased the displacement of the wall but had a negligible effect on the soil displacement. Test results are consistent with the numerical analysis result of Namikawa et al. (2007), which found that partial failure of improved ground is not critical in the provided level of liquefaction mitigation.

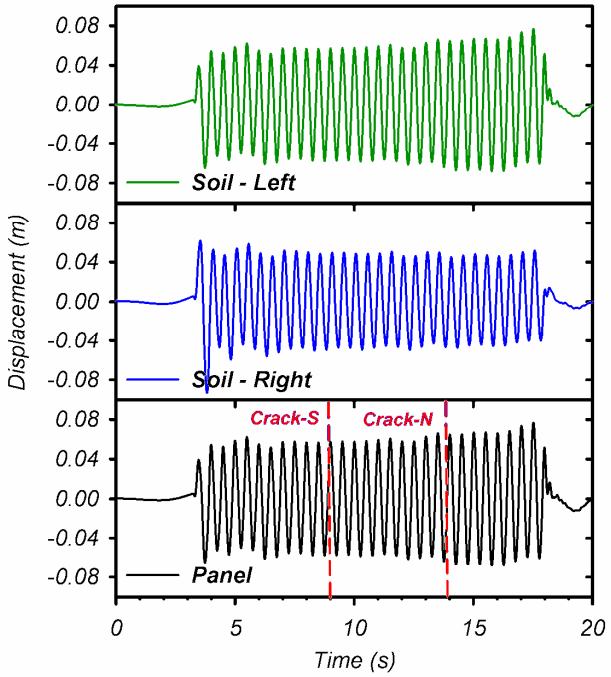

Figure 2.15. Time histories of displacement of clay surface and soil-cement grid top for a strong sine motion

The soil surrounding the grids was excavated and the cracking patterns in the panels were mapped following the test to investigate shaking-induced damage to the soil-cement grids. Cracks were an easily observed indication of the effect of shaking on the panels. Cracking patterns, location, orientation, number and distribution of the cracks provided information about the performance of the grids and possible failure modes. In Figure 2.16, plan and 3D views of soil-cement panels with cracks are presented. The soil-cement grids

had to resist the inertia force of the soil mass within the grids and the dynamic earth pressures exerted by the soils outside of the grids. These forces can cause large tensile and shear stresses inside the soil-cement panels and can be expected to lead to cracks, especially at joints and within walls which are perpendicular to the shaking (Figure 2.16b). Cracks were found to have propagated along the whole depth of the soil-cement panels. An issue for future study is the performance of a damaged soil-cement grid in subsequent shaking events.

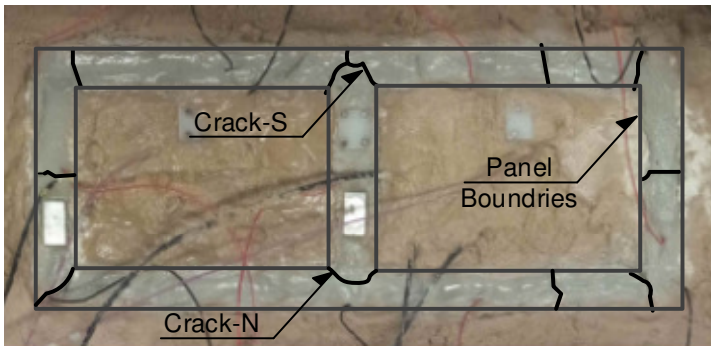

(a) Plan View

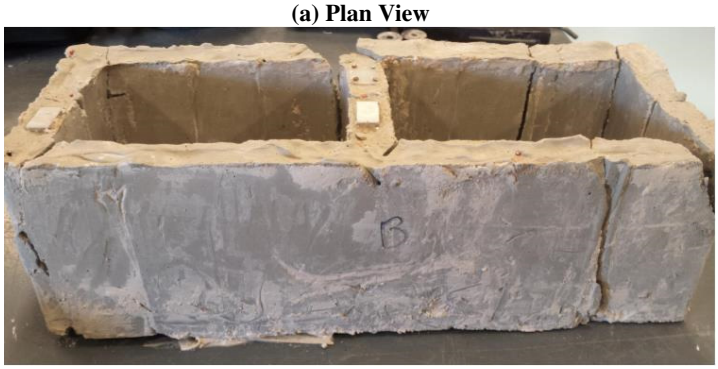

(b) Side View

Figure 2.16. Soil-Cement Grid after Tests

2.5 Conclusion

At the preliminary stages of this study, a series of small centrifuge tests were carried out to develop: (1) soil-cement mix designs; (2) soil-cement construction technique for centrifuge model tests; and (3) a crack detection technique to track the crack propagation along the height and length of soil-cement panels. Preliminary dynamic centrifuge tests were also performed to evaluate the testing efficacy. Different soil-cement mixtures were examined and it was found that the critical factors influencing the strength gain of the mixture are the cement type, curing environment and soil-cement-water ratio. Strength, workability and setting time of the soil-cement mixture are the key parameters which were

considered in the selection of the soil cement mix to be used in the planned centrifuge tests. The tests also showed that centrifuge models of soil-cement grid reinforced soil could be constructed using trenching and excavation technique and the results could be used to examine system-level performance, including the effects of grid cracking.

3 Simple Method for Detecting Cracks in Soil-Cement Ground Reinforcement for Geotechnical Centrifuge Tests

This chapter is produced from two papers, Khosravi et al. 2015, presented in the Deep Mixing 2015 Conference, and Tamura et al. 2016, prepared for International Journal of Physical Modeling.

Khosravi, M., Boulanger, R. W., Wilson, D. W., Tamura, S., Olgun, C. G., Wang, Y., (2015). "Seismic Performance of Soil-Cement Grid Supporting a Structure over Soft Clay." The Deep Mixing 2015 Conference, San Francisco, CA, 631-640.

Tamura, S., **Khosravi, M.,** Boulanger, R. W., Wilson, D. W., Olgun, C. G., D. Rayamajhi, Wang, Y. (2016). "Simple Method for Detecting Cracks in Soil-Cement Mixture in Centrifuge Modeling", Journal of Geotechnical Testing (In Preparation)[2]

Abstract: This chapter describes the centrifuge model construction procedure for a soil-cement grid supporting a structure over soft clay in the large centrifuge test and a new crack detection mechanism and its validation process to estimate the formation of cracks in soil-cement ground reinforcement. Centrifuge test models included a 23.4 m thick clay profile reinforced with an "embedded" soil-cement grid which penetrated the underlying dense sand layer. A single degree of freedom structure was located on a square shallow foundation over the central part of the soil-cement grid system. The models were subjected to a series of shaking events with peak base accelerations (PBAs) ranging from 0.006 to 0.546 g. The test showed that centrifuge models of soil-cement grid reinforced soil could be constructed using trenching and excavation technique and the results could be used to examine system-level performance, including the effects of grid cracking. The proposed crack detection mechanism is a brittle conductor providing a binary indication of if, and when, a sensor is cracked. Performance of the proposed crack detection system during shaking was investigated using 1) time series of accelerations, displacements, and footing rotation (2) change in resistance of crack detector before and after the tests measured using

[2] Mohammad Khosravi conducted all the tests, and performed all data analysis and provided all data, and was involved in figure preparation and review process.

multimeter, (3) change in potential difference measurements (voltage output) during shaking and after testing, and (4) post-test crack mapping in the soil-cement grids.

Keywords: Soil-Cement Grid Construction, Soil-Cement Cracking, Pencil Lead,

3.1 Introduction

Dynamic centrifuge model tests have been used to investigate the effects of soil-cement ground reinforcement on settlements or other ground failure modes in soft or liquefiable soils (e.g., Babasaki et al. 1992, Adalier et al. 1998, Kitazume and Maruyama 2006, Takahashi et al. 2006, Ishikawa and Asaka 2006). In each of these studies, prefabricated soil-cement or acrylic grids have been used as the reinforcing elements due to its known and uniform physical and mechanical properties. The limited experimental and case history data do not provide sufficient information to quantify the effect of partial damage and cracking of soil-cement ground reinforcement on their ability to limit settlements or deformations to acceptable levels.

Cracks are an easily observed indication of the effect of loading (e.g. earthquake loading) on the response of concrete structures. Cracking patterns, location, orientation, number and distribution of the cracks provide information about the performance of the structure and possible failure modes. Different techniques have been used to properly estimate if and where cracking occurs in a concrete structure. These techniques are either based on the change in response of the structure due to cracking such as change in natural frequency (Salawu, 1997), and antiresonant frequency (Dilena and Morassi 2004), or using new technologies such as image processing (Li et al. 1991, Sinha and Fieguth 2006), acoustic emission (AE) (Gu et al. 2000, Shiotani et al. 2001), and fiber-optic sensor (Gu et al. 2000, Habel and Krebber 2011). Visual inspection of cracking of underground structures (e.g. ground reinforcement) is impossible during the test. Post-test inspection of the cracks after excavation of the soil surrounding the structure provides useful information about overall performance of the underground structure, but limited information can be obtained about possible failure modes, and time of cracking. Change in frequency content of the system is not a reliable technique to estimate cracking of underground structures, since it can be affected by the response of surrounding soil and the interaction between the soil and underground structure. Using acoustic emission (AE) and fiber-optic sensors in

geotechnical centrifuge is also difficult and expensive. An alternative inexpensive approach for estimating cracking in centrifuge testing is strain measurement. A large change in strain value is an indication of cracking in the structure. A strain gauge, however, measures strain at a local point and also difficult to be installed on cast-in-place underground structures such as soil-cement ground reinforcement (e.g. grid or column).

This chapter describes a new crack detection mechanism and its validation process in centrifuge testing to estimate the formation of cracks in soil-cement ground reinforcement. The proposed mechanism is a brittle conductor providing a binary indication of if, and when, a sensor is cracked. The crack detection system was used in a series of dynamic centrifuge tests, to investigate the performance of soil-cement grid during earthquake loading. Centrifuge test models included a 41 cm thick clay profile reinforced with an "embedded" soil-cement grid which penetrated the underlying dense sand layer. A single degree of freedom structure was located on a square shallow foundation over the central part of the soil-cement grid system. The models were subjected to a series of shaking events with peak base accelerations (PBAs) ranging from 0.006 to 0.546 g. Performance of the proposed crack detection system during shaking was investigated using 1) time series of accelerations, displacements, and footing rotation (2) change in resistance of crack detector before and after the tests measured using multimeter, (3) change in potential difference measurements (voltage output) during shaking and after testing, and (4) post-test crack mapping in the soil-cement grids.

3.2 Proposed Crack Detection Technique in Soil-Cement Ground Reinforcement[3]

A crack detection mechanism was developed to estimate the formation of crack in a soil-cement column and grid during and after earthquake shaking for centrifuge modelling. The mechanism includes a brittle conductor (painted on soil-cement column or embedded in the soil-cement column or wall) providing a binary indication of if, and when, a sensor is cracked. The sensor shows a large change in conductivity if an open crack develops

[3] Tamura et al. 2016.

anywhere along its length. The change in conductivity is temporary if the crack later closes and contact is re-established between both sides of the cracked conductor.

Two different approaches were used to develop a crack detector in centrifuge testing: (1) a thin strip of conductive carbon painted along the longitudinal direction of a soil-cement column (Figure 1a), and (2) a 2-mm-diameter (model scale) pencil lead embedded in the soil-cement column or wall (Figures 1b, and c).

In the first approach, we painted a thin strip of conductive carbon along the longitudinal direction of soil-cement column. Two wires were attached to the strip at both ends using five minute epoxy and cable ties as shown in Figure 3.1. This approach only works for prefabricated soil-cement columns and grids in tests with sand. Using prefabricated soil-cement is not possible in clay since the clay profile needs to be consolidated prior to soil-cement grid construction.

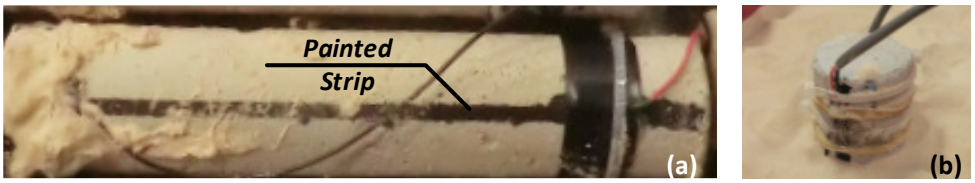

Figure 3.1. First Approach: Using Conductive Carbon Painting on a Soil-Cement Column, (a) Column with Painted Strip after Test, (b) Details of the Top of the Column in Soil Model

In the second approach, we embedded a 2-mm diameter pencil lead in the soil-cement column or wall as shown in Figure 3.2b and c. Two wires connect to both ends of the pencil lead using heat-shrink tubes. The wires connect to the centrifuge DAQ system using a strain type sensor to measure the voltage change during the tests. Pencil lead forms a strong bond with the surrounding soil-cement material during curing. Pencil lead also has a lower tensile strength compared to the soil-cement material, and its electric resistance is less than of the soil-cement material. Therefore, the crack detection mechanism in the centrifuge test was developed using 2-mm diameter pencil lead.

3.3 Overview of Centrifuge Test Program

The performance of crack detector was examined using dynamic centrifuge tests of a soft soil treated with soil-cement grid. Centrifuge tests were performed using the 9.1-m radius centrifuge at the University of California at Davis, Center for Geotechnical Modelling using a “Hinged-Plate model Container (HPC)” under 57 g centrifugal

acceleration. The detail of the centrifuge tests was described in the preliminary report (Khosravi et al., 2015c, d).

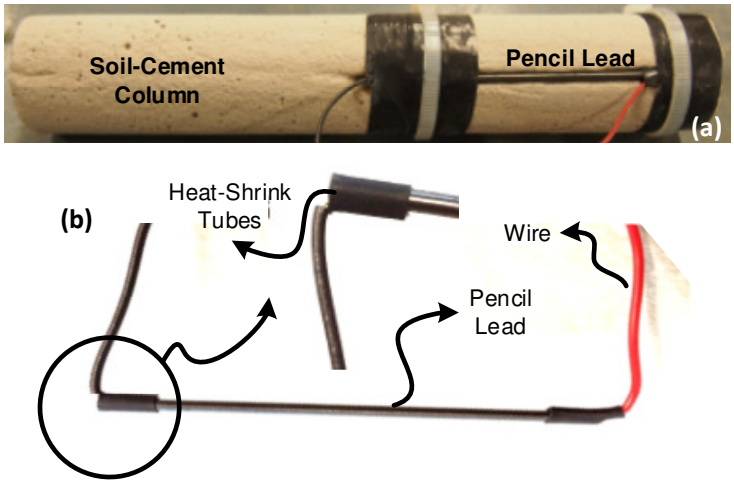

Figure 3.2. Second Approach: Using Pencil Lead, (a) Column with Pencil Lead, (b) Details of the Crack Detectors

The centrifuge models examined a lightly over-consolidated clay profile with an unreinforced soil profile on the left half of the container and an "embedded" soil-cement grid which penetrated the underlying dense sand layer on the right half as shown in Figure 3.3a. Model MKH01, before placement of the single degree of freedom (SDOF) structures on top of the grids, were shaken with 13 different motions with PBA of 0.006 to 0.18 g and peak base velocities (PBV) ranging from 0.9 to 24 cm/s as shown in Table 3.1 (prototype scale). These shaking events were used to examine the effect of the soil-cement grids on dynamic site response. The dynamic responses of the reinforced soil profiles during those events and analyses of the soil-cement grids' reinforcing effects are described in Khosravi et al. (2016).

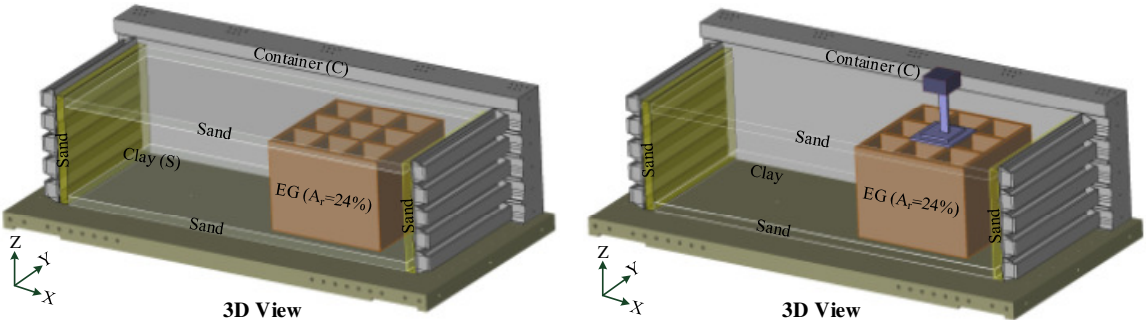

Figure 3.3. Model configurations with dimensions in prototype scale

The SDOF structure was then placed over the central part of the grid system over the sand layer in test MKH02 as shown in Figure 3.3b. The SDOF structures were comprised

of aluminum square footings, aluminum rectangular hollow columns, and aluminum and steel block superstructures (Figure 3.4). The mass of the superstructure, column, and footing were 4.8 kg, 0.2 kg, and 2.1 kg, respectively. The natural period of the structure was 71 Hz under fixed base condition. The footing with dimensions of 20 cm × 20 cm was placed on the center grid. The model, with the SDOF structures in place, was shaken with a sequence of 12 shaking events. The sequence of shaking events and their PVA, and PBAs are provided in Table 1. Input motions were step motion, sine sweep motions, the 1999 Chi-Chi earthquake (TCU-078) and the 1995 Kobe earthquake.

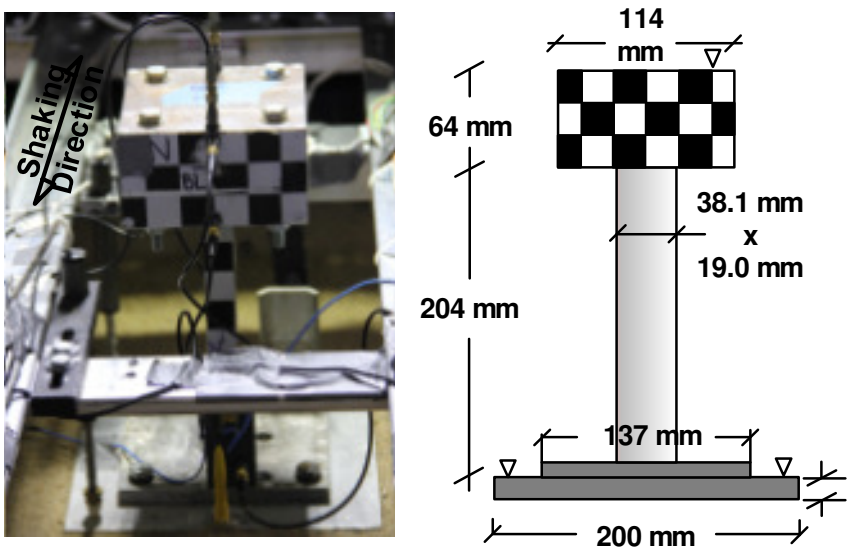

a) SDOF System **b) Parallel to shaking**

Figure 3.4. SDOF Structure (Model Scale)

The soil consists of a 41 cm thick layer of kaolinite (Hydrite Flat DS) underlain by 4 cm thick saturated dense sand (Dr ≈ 90%) for drainage purpose. A 4 cm thick layer of course Monterey sand was placed over the soil-cement grids as a bearing layer for the SDOF structures. The water table was 1 cm below the ground surface for all models. Properties of the kaolinite include: Liquid Limit, LL=47; Plastic Index, PI=19; specific gravity of solids, G_s=2.58; median particle size of 4.0 m; and a coefficient of consolidation, C_v=0.7 mm^2/s in virgin loading and 2.3 mm^2/s in unloading/reloading (Khosravi et al. 2015a).

The clay layer was constructed by pre-consolidating the clay in six lifts using a hydraulic press. First, a clay slurry was batch-mixed in a vacuum mixer at an initial water content of approximately 80%. The slurry was then poured into the container and pre-

consolidated in a press with a vertical pressure equivalent to the self-weight of the clay at the bottom of the layer at 57 g. The pre-consolidation process for each lift of clay was monitored using LPs and the model was allowed to consolidate until approximately 95 percent of the ultimate consolidation settlement had occurred.

Table 3.1. Ground Motions at the Base of the Model Containers for Model MKH01 and MKH02

Event No.	*Motion Name*	*MKH01*		*Event No.*	*Motion Name*	*MKH02*	
		PBA g	*PBV cm/s*			*PBA g*	*PBV cm/s*
1	Step	0.005	0.86	1	Step	0.006	0.81
2	SW7-333	0.025	4.32	2	SW7-333	0.03	3.77
3	TCU 078	0.074	6.5	3	TCU 078	0.083	7.5
4	Kobe 0807	0.042	6.64	4	Kobe 0807	0.042	6.67
5	SW7-333	0.025	3.49	5	SW7-333	0.031	3.71
6	TCU 078	0.174	15.02	6	TCU 078	0.178	15.57
7	Kobe 0807	0.09	12.35	7	Kobe 0807	0.089	12.79
8	SW7-333	0.029	3.65	8	SW7-333	0.031	3.58
9	TCU 078	0.316	25.3	9	TCU 078	0.323	26.18
10	Kobe 0807	0.181	24.33	10	Kobe 0807	0.188	23.86
11	SW7-333	0.03	5.15	11	SW7-333	0.033	4.09
12	SW7-333	0.03	3.59	12	Kobe 0807	0.546	58.58
13	SW7-333	0.031	3.76	13	SW7-333	-	-

3.3.1 Soil-Cement Grid Construction

A soil-cement grid was constructed to improve the soft clay enough to support a model structure. The construction of the grid was a challenge for the current centrifuge testing program. Using prefabricated soil-cement or plastic grids was not possible in clay since the clay profile needed to be consolidated prior to soil-cement grid construction. A series of small centrifuge tests were performed using the 1-m radius centrifuge at the Center for Geotechnical Modeling (CGM) at UC Davis to establish a soil-cement construction procedure in soft clay for centrifuge tests (Khosravi et al 2015a, b). A soil-cement mixture with reasonable strength, workability, and initial setting time had to be developed in order to perform the experimental research program. Furthermore, observations from these tests suggested that the trench and excavation method produced more uniform wall thicknesses along the grid depth and a better connection between perpendicular panels in the model grid (Khosravi et al 2015a, b). The soil-cement mix and grid construction for MKH02 are described below.

For MKH02 a soil-cement mixture with high water-cement ratio of 3.1:1.0 (by weight) was used to produce soil-cement with high fluidity to facilitate the soil-cement grid construction. The soil-cement ratio was 1.9:1.0 (by dry weight). Unconfined compressive strengths in the range of 450 to 600 kPa were obtained in 7 days (curing time).

Soil-cement grids were constructed using the trench and excavation method (Khosravi et al. 2015a,b, c). In this method, first a mold consisting of nine 15cm × 15cm stainless steel square grids were fabricated. One wood frame was used to hold and align the steel grids during the process of inserting them into the consolidated clay model. The spacing between the mold walls was equal to the required thickness for the soil-cement panels. The inside surface of the grids were covered by 0.012" thick Wear-Resistant Slippery UHMW tape to reduce friction between the metal and clay. The UHMW tape provides a nonstick, low-friction surface similar to the more common PTFE tape but with higher abrasion and impact resistance. The mold (Figure 3.5a) was pushed into the clay (Figure 3.5b) using a hydraulic press. The clay within the mold was excavated by hand using a spatula. Once sufficient excavation was complete, the mold walls were filled with soil-cement slurry (Figure 3.5c). The steel plate grids were then pulled out and sensors were placed into the slurry at the target location (Figure 3.5c). Eighteen crack detectors were placed in the soil-cement slurry at the locations and depths shown in Figure 3.6. The numbers following sensor ID in parenthesis show the depth of crack detectors from the top of soil-cement grid (model scale, cm). The soil-cement grid after construction with crack detectors embedded inside the grid is presented in Figure 3.5d. Figure 3.5e shows the soil model and container at the end of centrifuge arm shortly before testing.

3.4 Results and Discussion

Performance of crack detectors embedded in the soil-cement grid were examined using (1) time series of accelerations, displacements, and footing rotation (2) change in resistance of crack detector before and after the tests measured by multimeter, (3) change in potential difference measurements (voltage output) during shaking and after testing, and (4) post-test crack mapping in the soil-cement grids.

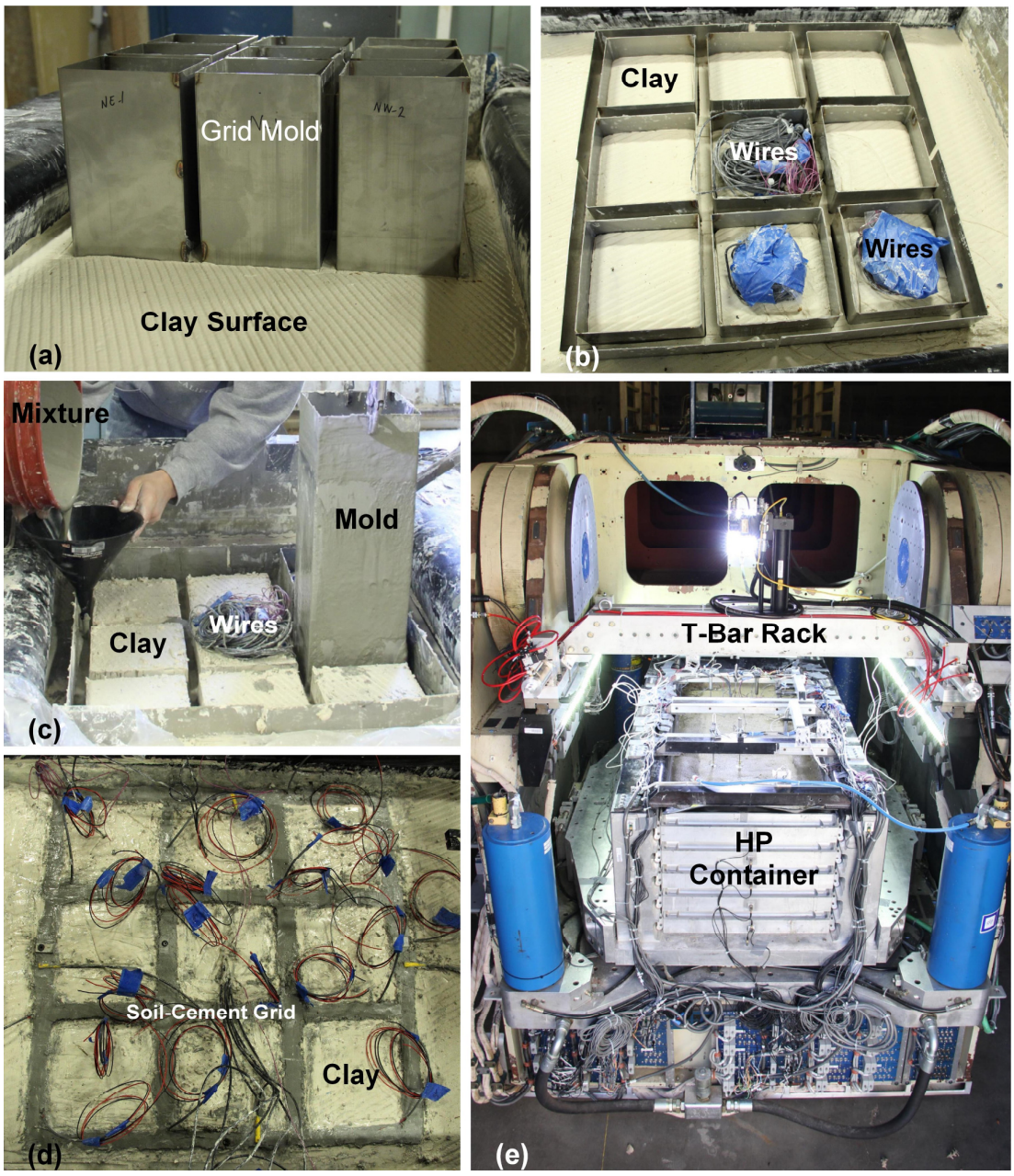

Figure 3.5. Soil-Cement Grid Construction Process: a) Grid Mold Inside the Clay, c) Purring the Soil-Cement Mixture, d) Soil-Cement Grid After Construction, and e) Sample on the Centrifuge Arm

3.4.1 Change in Resistance of the Crack Detector

The electric resistance of the crack detectors was measured using a multimeter before (MKH01) and after the tests (MKH02) to evaluate and verify the performance of the crack detectors. Figure 3.7 shows the electric resistance values before the tests (MKH01). The range of the electric resistance was between 9 and 71. Figure 3.8 shows the values of the electric resistance after the centrifuge tests (MKH02). Based on the results presented in

this figure, the electric resistance values of CD3, 4, 6, 11, 12, and 13 jumped to more than 10k, indicating the occurrence of cracking. The electric resistance values of CD1, 2, 5, 7, 8, 9, 10, 14, 15 and 16 were less than 500, suggesting that cracking of the soil-cement grid did not occur at those locations. There were some differences in the values of electric resistance measured by the multimeter before and after the tests, which could be due to deterioration of the connecting wire in the soil-cement grid. In the case of CD17, the multimeter measured an electric resistance value of 1400. This makes it unclear whether cracking occurred or not. Figure 3.9 shows the ratios of the electric resistance of the crack detectors before the test (MKH01) to that after the test (MKH02). As presented in this figure, the ratios of electric detectors for CD3, 4, 6, 11, 12, 13 and 17 were more than 100, while they were less than 15 for the other ones.

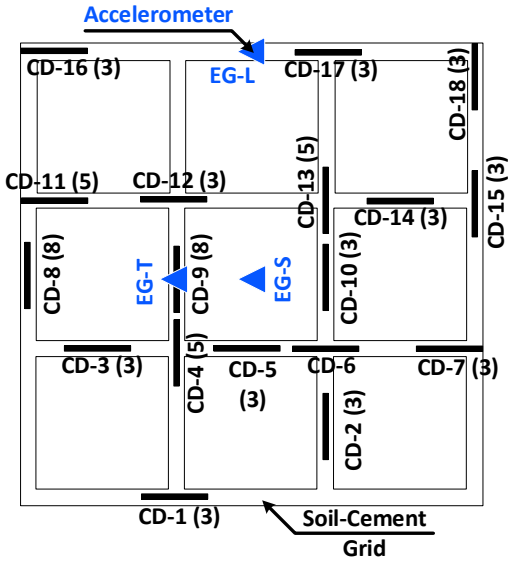

Figure 3.6. Plan View of the Location and Depth of Crack Detectors Embedded in Soil-Cement Grid

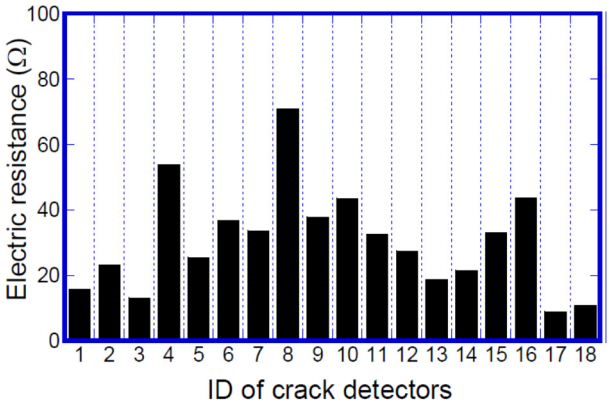

Figure 3.7. Electric Resistance of Crack Detectors before Test MKH01 (Without structure model)

3.4.2 Post-Test Crack Mapping in the Soil-Cement Grids

The performance of the proposed crack detecting technique in this study was validated through visual observation and mapping of the cracks on the soil-cement grid after the test. In this regard, after completion of tests MKH01 and MKH02, sand over the soil-cement grids was carefully removed and the cracking locations on the grids were marked with a black sharpie. Figure 3.10 shows sketches of the locations of shaking-induced cracks on the top of the soil-cement grid after tests MKH01 (W/O structure) and MKH02 (With

Structure). The blue lines show the cracks after test MKH01, and the red lines are those after test MKH02. The location of the cracks on the embedded grids are also presented in Figure 3.11 after test MKH02. As presented in Figure 3.10, the soil-cement grid experienced slight cracking after test MKH01. In this case, hairline cracking was occurred at the joint near the location of CR4, and some minor cracks were observed on the surface of the soil-cement grid. Unfortunately, cracks related to tests MKH01 were mostly observed in locations with no crack detector and accordingly, it wasn't possible to identify the time cracking was initiated.

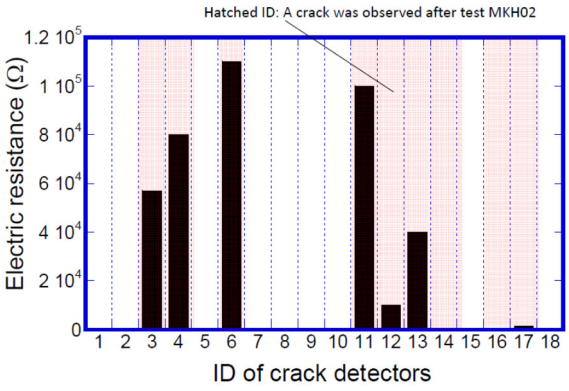

Figure 3.8. Electric resistance of crack detector after the test MKH02 (With structure model)

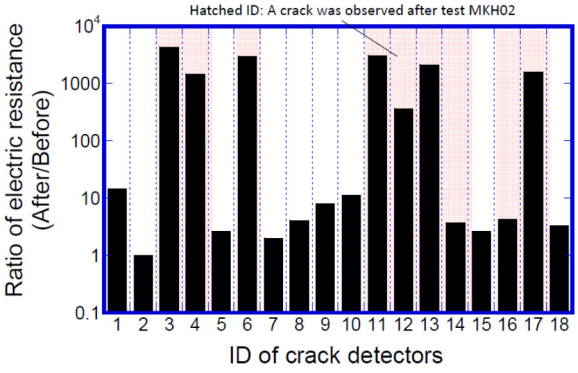

Figure 3.9. Ratios of electric resistance before MKH01 to that after MKH02

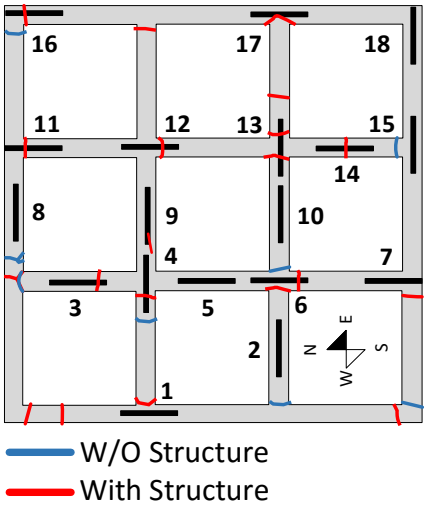

Figure 3.10. Location of Cracks at top of soil-cement grid after Test MKH01 (Blue Lines) and after Test MKH02 (Red lines).

The cracking scheme presented in Fig. 3.10 indicated that most of cracking happened during the test MKH02, indicating the significant effect of SDOF structure on the response of the soil-cement grid during shaking. Table 3.2 summarizes the conditions of the soil-

cement grid at the location of the crack detectors. The IDs of crack detectors which showed cracking in post-test inspection were hatched as shown in Figures 3.8 and 3.9. Based on the results, most of cracking happened at the locations of CR3, 4, 6, 11, 12, 13 and 17, where the electric resistance ratios (Figure 3.9) were more than 100. For those locations where the electric resistance ratios (CR1, 2, 7, 8 and 18) were less than 15, there was no sign of cracking of the soil-cement grid. From these observations, it may be concluded that the electric resistance ratio may be a proper term indicating cracking development in the soil-cement grid. Observations from post-test inspection of the soil-cement grid were consistent with the results from crack detectors in most cases. There were some cases where the crack detectors failed to recognize crack initiation. For example, post-inspection of the grid showed some cracks parallel to the crack detectors at the locations of CR5, 9, 10, with no crack detector crossing, or for the crack detectors, CR14 and 16, the electric resistance measurements showed small changes in value after shaking, suggesting that no cracking should have occurred in those locations. However, post-test inspection of the grid showed cracks crossing the crack detectors in those locations.

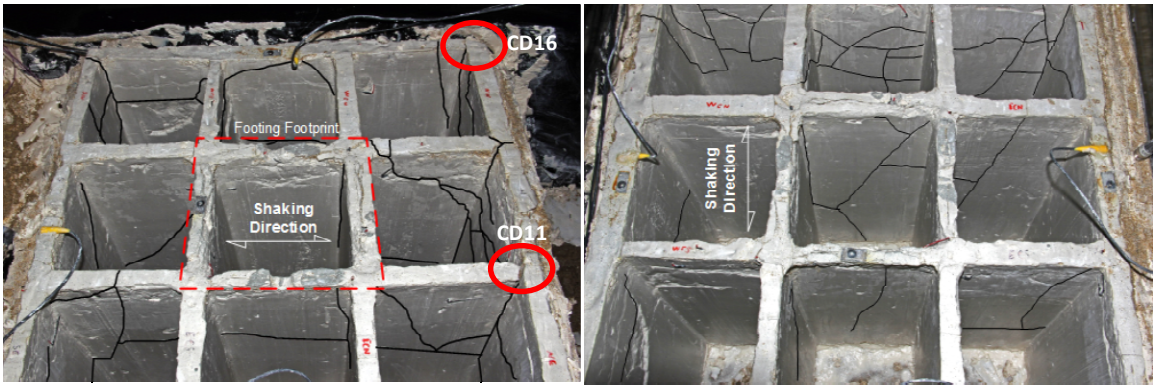

Figure 3.11. Post-testing photographs of the embedded soil-cement grid in MKH02 with any visible cracks highlighted for clarity.

3.4.3 Change in Potential Difference Measurements (voltage output)

Based on Ohm's law, for a circuit with constant current flow, any change in conductivity of a crack detector can be monitored using the electric potential difference between the two ends of the crack detector (ΔV). For graphite with a resistance of approximately zero ohm, the electric potential difference between the two ends of crack detector should be also zero (or close to zero) before any open crack develops along its length. An open "crack" (discontinuity) in the crack detector changes conductivity, and

electric potential difference between the two ends of crack detector. Figure 3.12 summarizes the potential difference measurements (voltage outputs) between the two ends of crack detector before and after test MKH01. As can be seen, initial voltage outputs for all crack detectors were close to zero. Change in voltage output in crack detector was only observed in CR4 during Kobe motion with PBA = 0.18 g. A hairline crack was observed near the location of CR4 in post-test inspection of the soil-cement grid after test MKH01. The crack detector was at a depth of 4-cm (model-scale) from the top of the soil-cement grid. The results indicated that the crack propagated through the depth, and crossed the crack detector.

Table 3.2. Conditions of soil-cement grid at the location of crack detectors

CD No.	Condition near crack detectors
CD-1	No Crack
CD-2	No Crack
CD-3	Cracks all around CD
CD-4	Cracked
CD-5	Horizontal cracks, no cracking pass through CD
CD-6	Cracked
CD-7	No Crack
CD-8	No Crack
CD-9	Cracks parallel to CR, but no cracking pass through CD
CD-10	Cracks parallel to CR, but no cracking pass through CD
CD-11	Big crack was observed cutting crack detector
CD-12	Vertical crack pass through CR
CD-13	Vertical crack pass through CR
CD-14	Hairline crack
CD-15	Vertical crack stop at CR
CD-16	Vertical cracks is wide open on the surface, but not major in lower depth
CD-17	Hair cracks around CR
CD-18	No Crack

Dynamic responses of the embedded grid in model MKH01 (EG with A_r = 24%) are shown in Figure 3.13 for Kobe motion with peak base accelerations (PBA) of 0.19 g. This figure shows the input base motion, horizontal acceleration and displacement time histories near the ground surface on the soil inside the grid cells (EG-S), and the mid points of the transverse walls of the grid (EG-T), and the voltage output of CR4 in which cracking of the soil-cement grid was observed. Relative displacement between the soil inside the grid cell and transverse wall is also presented in Figure 3.13b. As shown in Figure 3.13b and c, the waveform of accelerations and displacements on the transverse wall (EG-T), and

enclosed soil (EG-S) were similar, suggesting that soil was constrained by soil-cement grid. As shown in Figure 3.13a and b, the peak horizontal acceleration (PHA) on the soil surface (EG-S) and transverse wall (EG-T) was PHA = 0.43 g producing an amplification factor of 2.4 comparing to the base motion. Based on the results, the transverse walls developed greater displacements than the soil. The differences in the displacements of transverse wall (EG-T) and soil surface (EG-S) are greatest at time equal to 13 sec when crack detector showed cracking of the soil-cement grid. These results suggest that the soil inside the grid acts as an external force, causing cracking of the soil-cement grid. Crack detector showed that the crack closed during cyclic load reversals as the contact between both sides of the cracked conductor was re-established. The mechanism of the soil-cement grid damage is described in Khosravi et al., 2016.

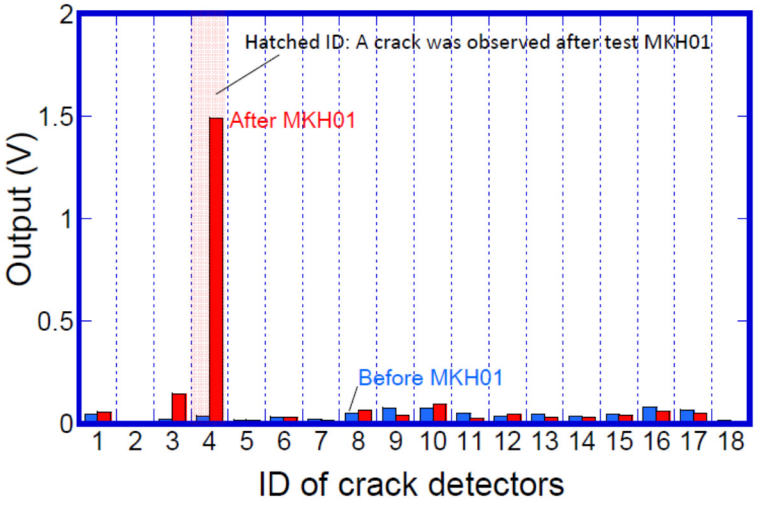

Figure 3.12. Voltage output of crack detectors before and after the test MKH01

The potential difference measurements (voltage outputs) between the two ends of crack detectors in the embedded grid in model MKH02 (EG with Ar = 24%) are shown in Figure 3.14 for Kobe motions with peak base accelerations (PBA) of 0.19 g and 0.54 g, and TCU motion with PBA of 0.32 g. During TCU motion with PBA = 0.32 g, crack detectors CR6, CR11, CR12, and CR13 which were at or close to the intersections of transverse and longitudinal walls experienced cracking. No new cracking developed during Kobe motion with PBA = 0.19 g. During Kobe motion with PBA = 0.54 g, four new crack detectors, CD3, CD14, CD16, and CD17, indicated cracking of the soil-cement grid. Among these four new crack detectors, CD3 and CD14 were in longitudinal walls, while the other two were at the joints.

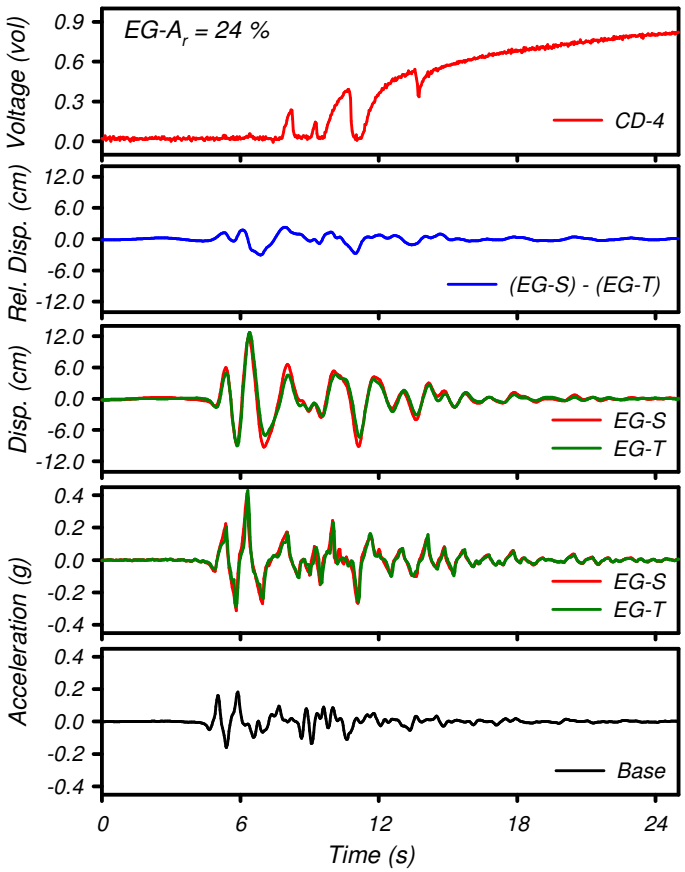

Figure 3.13. Time histories of acceleration, displacement and voltage output of CR4, Kobe (0.16g), MKH01.

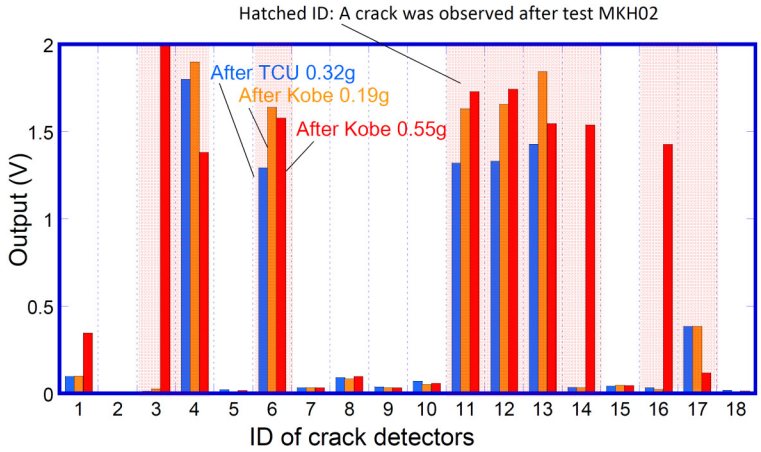

Figure 3.14. Voltage output of crack detectors after TCU(0.32g), Kobe(0.18g) and Kobe(0.55g) during the test MKH02

Acceleration responses of the embedded grid and supported structure in model MKH02 are shown in Figure 3.15 for Kobe motion with peak base acceleration of 0.54 g (Figure 3.15b). This figure presents horizontal motions recorded near the ground surface on the

soil inside the grid cells (EG-S), on the footing (EG-Ft), at the center of gravity of the superstructure (EG-St), and the input base motion. Relative displacement between the soil inside the grid cell and transverse wall and the voltage output of two crack detectors, CR14 and CR16, are also presented in Figure 3.15. As shown in Figure 3.15b and e, the soil surface (EG-S) had a PHA = 0.39 g (28% less than the PBA) and the superstructure (EG-St) had a PHA = 0.50g (7% less than the PBA). The surface acceleration had stronger long-period components than the base acceleration, which is attributed to softening of the soil and partial damage of the soil-cement grid, resulting in an effective lengthening of the reinforced soil system's effective natural period. As shown in Figure 3.15e, cracking started in CR14 at the time of 11 sec, which associated with the maximum rotation of the footing. Crack detector CR16 showed cracking of the grid at time equal to 13.2 sec, when relative displacement of soil to soil-cement grid reached its maximum. These results showed that both inertial loads from the super structure and kinematic force from the soil inside the soil-cement grid should be considered when evaluating cracking of the soil-cement grid.

The results from potential difference measurements during shaking were different from those measured using multimeter before and after tests for two crack detectors, CR16, and CR14. As mentioned earlier, the change in conductivity of crack detector is temporary if the crack later closes. Therefore, the difference between the results could also be attributed to possible reestablishment of the contact between both sides of the cracked crack detector after the test in those two crack detectors.

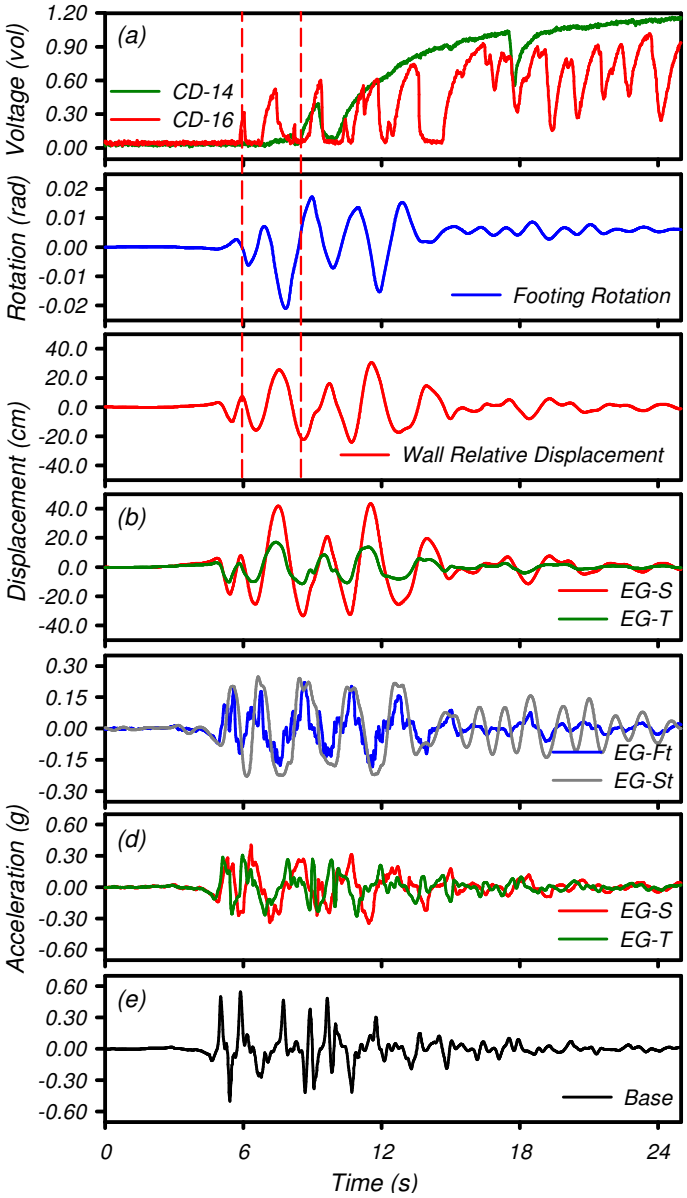

Figure 3.15. Time histories of acceleration, displacement and voltage output of CR14 and 16, Kobe (0.55g), MKH02

4 Dynamic Centrifuge Tests of Soft Clay Reinforced by Soil-Cement Grids

This chapter is from Khosravi et al. 2016, which is published in the Journal of Geotechnical and Geoenvironmental Engineering (With permission from ASCE).

Khosravi, M., Boulanger, R. W., Wilson, D. W., Tamura, S., Olgun, C. G., Wang, Y., (2016). " Dynamic Centrifuge Tests of Soft Clay Reinforced by Soil-Cement Grids." Journal of Geotechnical and Geoenvironmental Engineering, 10.1061/(ASCE)GT.1943-5606.0001487, 04016027.

Abstract. A pair of large centrifuge tests were conducted to evaluate the effect of soil-cement grid reinforcement on the seismic response of a deep soft soil profile. The soil profile consisted of a 23-m-thick layer of lightly over-consolidated clay, underlain and overlain by thin layers of dense sand. Each centrifuge model had two separate zones for a total of four different configurations: a zone without reinforcement, a zone with a "embedded" soil-cement grid which penetrated the lower dense sand layer and had a unit cell area replacement ratio A_r = 24%, a zone with an embedded grid with A_r = 33%, and a zone with a "floating" grid in the upper half of the clay layer with A_r = 33%. Models were subjected to 13 different shaking events with peak base accelerations ranging from 0.005 to 0.31g. This chapter examines the effect of the soil-cement grids on the global responses of the soil profiles, and the internal interaction between soil-cement grids and their enclosed soils. Nonlinearities in the dynamic responses and interaction mechanisms are examined using (1) time series of accelerations, shaking-induced excess pore water pressures, and post-shaking reconsolidation settlements, (2) response spectra and spectral ratios, (3) back-calculated composite stress-strain responses, (4) analyses of internal stress distributions between the grids and enclosed soils, and (5) dynamic crack detections and post-test crack mapping in the soil-cement grids. The results provide insights on the dynamic performance of soil-cement grids and an archived dataset for evaluating design procedures and numerical analysis methods.

4.1 Introduction

Soil-cement grids constructed by deep mixing method (DMM), trenching, jet grouting, or similar methods can be an effective method for improving soft soil profiles for support

of overlying structures or to reduce potential ground deformations under static or seismic loading. Design issues include the ability of the soil-cement grids to withstand applied forces and stresses without excessive damage and for the composite soil and soil-cement system to limit settlements or deformations to acceptable levels. Design methods for soil-cement grids, as structural foundations or slope reinforcements, are not as well developed for seismic loading conditions as those for static loading conditions.

Case histories from past earthquakes have shown that ground reinforcement can be an effective means for mitigation of earthquake-induced ground displacements. Soil-cement grids were, for example, found to have been effective in reducing earthquake damages during the 1995 Kobe earthquake (Tokimatsu et al. 1996).

Dynamic centrifuge model tests have been used to investigate the effects of soil-cement ground reinforcement on settlements or other ground failure modes in soft or liquefiable soils (e.g., Babasaki et al. 1992, Adalier et al. 1998, Kitazume and Maruyama 2006, Takahashi et al. 2006, Ishikawa and Asaka 2006, Rayamajhi et al. 2014b). In each of these studies, prefabricated soil-cement or acrylic grids have been used as the reinforcing elements. Babasaki et al. (1992) and Takahashi et al. (2006) illustrated the importance of grid spacing on maximum pore water pressure ratios. Takahashi et al. (2006) examined the role of shaking intensity and depth of reinforcement in design of soil-cement grids. Tests by Matsuo et al. (1996), Adalier et al. (1998), and Kitazume and Terashi (2014) demonstrated the importance of an external stability analysis of the reinforced zone (e.g. sliding, overturning or bearing failures) when a floating soil-cement grid is used underneath an embankment slope. Numerical analyses have been used to evaluate overall deformation mechanisms and critical aspects of the seismic response of improved soil deposits subject to severe ground shaking, including 2D analyses (O'Rourke and Goh 1997) and 3D analyses (Fukutake and Ohtsuki 1995, Namikawa et al. 2007, Bradley et al. 2013, Nguyen et al. 2013, Puebla et al. 2006). These studies illustrated the importance of area replacement ratio (A_r = area of soil-cement divided by total area), depth of improvement, and stiffness of the improved soils on the response of the enclosed soil. Some studies also indicated that grid improvement caused an increase in amplitude of the surface ground motion which could result in higher inertial loading for the overlying superstructure (Bradley et al. 2013).

Namikawa et al. (2007) investigated the dynamic behavior of soil-cement grid reinforcement and observed concentrated tensile stress at the corner and mid-length of the soil-cement walls. Namikawa et al. (2007) found that partial failure of the improved ground did not notably reduce the provided level of liquefaction mitigation. Numerical analyses have also been used to develop simplified analysis methods for preliminary design (Nguyen et al. 2013, Rayamajhi et al. 2014a,c).

Current allowable stress based design procedures (e.g., Bruce et al. 2014) do not explicitly allow partial damage to the soil-cement grid system. Allowable stress design procedures focus on the ability of the soil-cement grid reinforcement to withstand applied forces and stresses without excessive damage. The effect of partial damage and cracking of soil-cement grids on their ability to limit settlements or deformations to acceptable levels has not been well studied. This consideration requires an evaluation of the composite behavior of the grid reinforced soil and the internal distribution of stresses and strains. The limited experimental and case history data do not provide sufficient information to quantify the shear reinforcement mechanisms of soil-cement grids in soft or liquefiable soils during strong earthquake loading.

This chapter summarizes results of dynamic centrifuge model tests examining the effect of soil-cement grid reinforcement on the seismic response of a deep, lightly over-consolidated clay profile. Two large centrifuge models were used to examine four configurations: a zone without reinforcement, a zone with an "embedded" soil-cement grid which penetrated the underlying dense sand layer and had a unit cell area replacement ratio A_r = 24%, a zone with an embedded grid with A_r = 33%, and a zone with a "floating" grid in the upper half of the clay layer with A_r = 33%. Models were subjected to 13 shaking events with peak base accelerations ranging from 0.005 to 0.30g. The effects of the soil-cement grids on the nonlinear dynamic responses of the soil profile and the internal interactions between the soil-cement grids and enclosed soils are examined using (1) time series of accelerations, shaking-induced excess pore water pressures, and post-shaking reconsolidation settlements, (2) response spectra and spectral ratios, (3) back-calculated composite stress-strain responses, (4) analyses of internal stress distributions between the grids and enclosed soils, and (5) dynamic crack detections and post-test crack mapping in

the soil-cement grids. The results of the experiments and analyses provide insights on the dynamic performance of soil-cement grids and an archived dataset for evaluating design procedures and numerical analysis methods.

4.2 Centrifuge Testing

Two centrifuge tests were performed using the 9-m radius centrifuge at the University of California at Davis Center for Geotechnical Modeling and the data archived for distribution (Khosravi et al. 2015c). The tests were performed at a centrifugal acceleration of 57g. The recorded data and model dimensions were converted into prototype units according to the scaling laws described by Kutter (1995). All data are presented in prototype units unless otherwise specified.

All tests were performed in a hinged-plate model container. This container allows large and permanent shear strains while limiting lateral strains under static loading. The inner dimensions of the container in model scale were 175.5 cm long (100.0 m in prototype), 65.0 cm wide (37.0 m in prototype), and 51.6 cm tall (29.4 m in prototype). A 3-mm-thick rubber membrane (model scale) was attached inside the container to make it water tight.

The tests consisted of two models as shown in Figure 4.1. Model MKH01 had an unreinforced soil profile (S) on the left half of the container and an embedded soil-cement grid (EG) on the right half as shown in Figure 4.1a. The embedded grid in MKH01 had nine square cells in a three-by-three pattern. The 1.2-m wide soil-cement walls were spaced 9.8 m center-to-center apart, for an average $A_r = 24\%$. Model MKH03 had a floating soil-cement grid (FG) on the left half of the container and an embedded soil-cement grid (EG) on right half as shown in Figure 4.1b. The embedded and floating grids in MKH03 each had 16 square cells in a four-by-four pattern. The 1.2-m wide soil-cement walls were spaced 6.9-m center-to-center apart for an average $A_r = 33\%$ for both grids. The soil profile in each model consisted of a 23.4-m thick layer of kaolinite (Hydrite Flat DS, manufactured by the Imerys Company) underlain by a 2.3-m thick saturated dense coarse sand (relative density, $D_r \approx 90\%$), used to provide drainage. In each case, the soil-cement grids were flush with the top of the clay layer, and in both models, the entire profile was overlain by a 2.3-m thick dense coarse sand layer ($D_r \approx 90\%$) to represent the working surface typically required in field applications. The water table was about 0.5 m below the ground surface

for both models. Properties of the kaolinite include: Liquid Limit, LL = 47; Plastic Index, PI = 19; specific gravity of solids, G_s = 2.58; median particle size of 4.0 μm; and a coefficient of consolidation, C_v = 0.7 mm^2/s in virgin loading and 2.3 mm^2/s in unloading/reloading (Khosravi et al. 2015a). Water was used as the pore fluid in this study, which means that the prototype permeability of the soil should be scaled to 57 times the model permeability based on the combined scaling laws for dynamics and diffusion (Kutter 1995). The scaled prototype permeability of the clays is, however, still sufficiently small that the soil acts as almost perfectly undrained during earthquake shaking (based on computed time factors as well as on observed dissipation rates). Higher viscosity fluids are commonly used with sands for consistent scaling of dynamics and diffusion, but are avoided for clays because of their unavoidable physical-chemical interactions with the clay minerals.

The clay profile was constructed by pre-consolidating the clay in six lifts using a hydraulic press. First, a clay slurry was batch-mixed in a vacuum mixer at an initial water content of approximately 80%. A single lift of clay slurry was placed in the container and then pre-consolidated in the press with the applied stress equivalent to the effective vertical stress expected at the bottom of the lift at 57g. The pre-consolidation process for each lift of clay was monitored using LPs and the model was allowed to consolidate until approximately 95 percent of the ultimate consolidation settlement had occurred. This means that the upper portion of each lift was slightly over-consolidated on average at 57g. The pre-consolidation stage was used to significantly reduce the amount of settlement and the time required for in-flight consolidation compared to starting from a slurry without pre-consolidation.

Soil-cement grids were constructed using the trench and excavation method as described in Khosravi et al. (2015a,b,c). A soil-cement mixture with high water-cement ratio of 3.1:1.0 (by weight) was used to produce soil-cement with high fluidity to facilitate the soil-cement grid construction. The soil-cement ratio was 1.9:1.0 (by weight). Unconfined compressive strengths in the range of 450 to 770 kPa were obtained in 7 days (curing time). A mold consisting of a series of stainless steel square grids was pressed down into the clay model using the press with a wood guide frame to maintain alignments. The

inside surfaces of the steel square grids were covered by 0.03 mm (0.012") thick Wear-Resistant Slippery UHMW tapes to reduce the friction between the metal and clay during insertion and excavation. The spacing between the mold walls was equal to the required thickness for the soil-cement panels. After the mold was pressed into place, the clay between the steel grid walls was excavated by hand using a spatula. The excavated space was then filled with soil-cement slurry, followed by extraction of the mold. Sensors were then embedded in the soil-cement walls at their target locations. After 7 days, during which time the soil-cement grid cured, the model was moved to the centrifuge, its sensors connected, and then subjected to a 57 g centrifugal acceleration. Settlements and pore water pressures were monitored until an average degree of consolidation greater than 95% was attained.

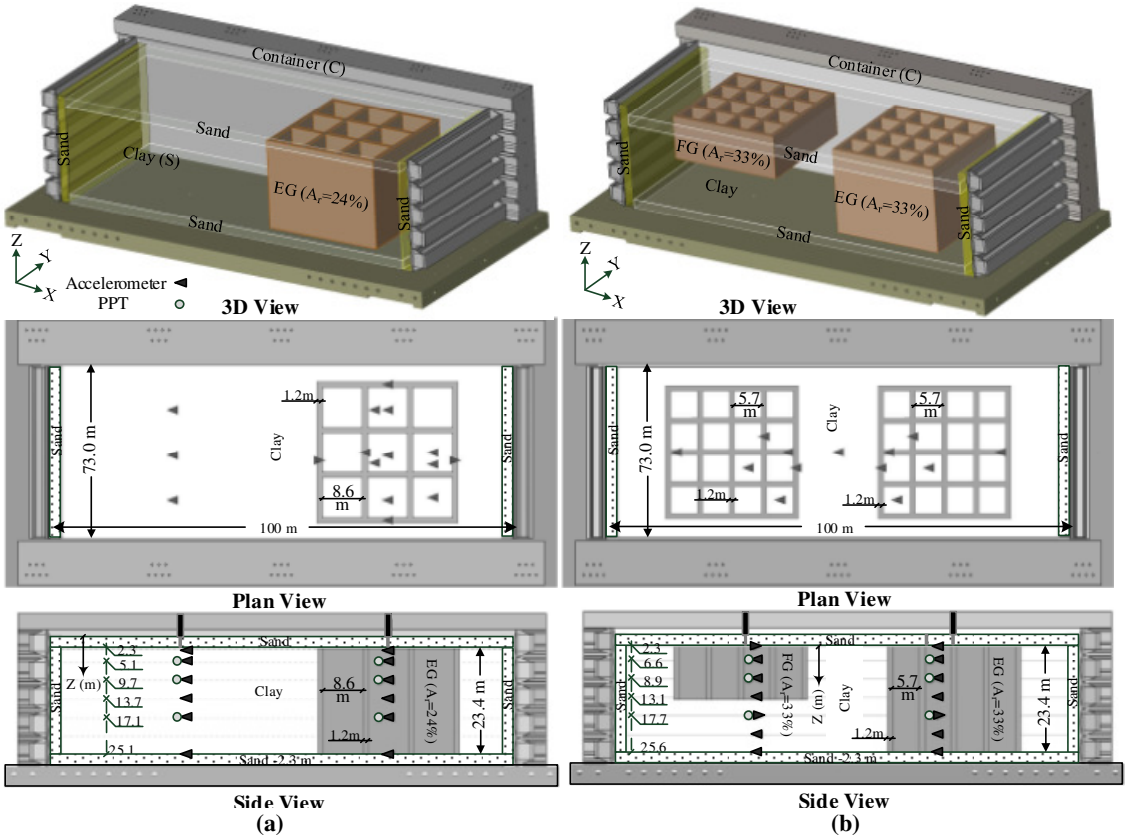

Figure 4.1. Model configurations with dimensions in prototype scale: (a) MKH01, (b) MKH03

Both models were shaken with the same sequence of 13 shaking events consisting of one step motion, six sine sweep motions, and six earthquake motions of varying intensity and frequency. The sine sweep motions contained continuously varying frequencies

between 0.1 and 6 Hz (progressing from lower to higher frequencies). The horizontal peak base accelerations (PBAs) during the sine sweep motions as measured at the base of the container ranged from 0.03 to 0.06g, which were small enough to not generate excess pore water pressures (EPWP). The recorded responses from the sine sweep motions were used to estimate the natural frequency of the soil profile at small strain levels, and also to investigate how that natural frequency was affected by the intervening strong shaking events. The earthquake motions were scaled versions of the recordings at station TCU-078 during the 1999 Chi-Chi earthquake and at Port Island (Kobe-0807) during the 1995 Kobe earthquake. These motions were high-pass filtered to remove low-frequency displacements that were outside the range of the shaking table's capacity. The sequence of shaking events and their PBAs for both models are provided in Table 1. Sufficient time was allowed after each strong shaking event for pore water pressure to return to the initial hydrostatic water pressure and thus fully dissipate any EPWP generated during the shaking.

Table 4.1. Ground Motions at Base

Event No.	Motion Name	MKH01		MKH03	
		PBA g	PBV cm/s	PBA g	PBV cm/s
1	Step	0.005	0.86	0.006	0.76
2	SW7-333	0.025	4.32	0.030	3.82
3	TCU 078	0.074	6.50	0.090	8.59
4	Kobe 0807	0.042	6.64	0.040	7.32
5	SW7-333	0.025	3.49	0.030	4.38
6	TCU 078	0.174	15.02	0.180	15.50
7	Kobe 0807	0.090	12.35	0.070	12.38
8	SW7-333	0.029	3.65	0.030	4.15
9	TCU 078	0.316	25.30	0.310	24.69
10	Kobe 0807	0.181	24.33	0.160	22.98
11	SW7-333	0.030	5.15	0.030	3.74
12	SW7-333	0.030	3.59	0.030	3.98
13	SW7-333	0.031	3.76	0.030	3.89

Models were instrumented with accelerometers, pore water pressure transducers (PPTs), linear potentiometers (LPs), and crack detectors (CDs) as described in Khosravi et al. (2015c). Instrument layouts are shown in Figure 4.1. Accelerometers were placed to record horizontal and vertical motions in the soil, the soil enclosed in the soil-cement grids, and the soil-cement grids. PPTs were placed in the clay to record the pore water pressure

generated during tests. LPs were used to record the ground surface and soil-cement grid settlements. The lateral response of the rings of the hinge-plate container were recorded using accelerometers and LPs.

4.3 Dynamic Responses

The dynamic responses of the two models, MKH01 and MKH03, are presented together to illustrate the effect of the soil-cement grids on the seismic response of the soft clay profile. Results from a scaled Kobe motion with low to high shaking level is presented, whereas responses for TCU motions and other shaking levels can be found in the data reports (Khosravi et al. 2015c,e) Supplement Figures (Appendix C).

4.3.1 Acceleration Responses

The acceleration responses of the unreinforced soil and the embedded grid (EG, A_r = 24%) sides of model MKH01 are shown together in Figure 4.2 for Kobe motions with PBA = 0.04 g (Figure 4.2a) and 0.18 g (Figure 4.2b). Each figure displays motions recorded near the ground surface on the soil (S), on the longitudinal walls of the grid (EG-L), the mid points of the transverse walls of the grid (EG-T), the soil inside the grid cells (EG-S), and the base motion (base). The unreinforced soil surface (S) had a PHA = 0.096g in the PBA = 0.04 g event (an amplification ratio of 2.4) and a PHA = 0.22g in the PBA = 0.18g event (an amplification ratio of 1.22). The much lower amplification ratio and richer long-period components for the surface motion (S) in the stronger shaking event are attributed to soil nonlinearity resulting in a lengthening of the soil system's effective natural period and increase in damping. The reinforced soil surface (EG-S) had a PHA = 0.069g in the PBA = 0.04g event (an amplification ratio of 1.72) and a PHA = 0.37g in the PBA = 0.18g event (an amplification ratio of 2.06). Thus, the reinforced soil (EG-S) produced a smaller amplification of motions compared to the unreinforced soil (S) at the low shaking level, but a significantly greater amplification at the stronger shaking level. The accelerations on the longitudinal walls (EG-L), transverse walls (EG-T), and enclosed soil (EG-S) were all similar for the PBA = 0.04g event. The accelerations on the transverse walls (EG-T) and enclosed soil (EG-S) remained similar (PHA = 0.40g versus 0.37g) in the PBA = 0.18g event, but the accelerations on the longitudinal walls (EG-L) were significantly lower (PHA = 0.19g). The differences and similarities in the various wall and enclosed soil

motions suggest that the transverse walls must have deformed significantly in flexure relative to the longitudinal walls. The acceleration responses of the embedded grid side (EG, A_r = 24%) in test MKH01 during an intermediate Kobe motion with PBA = 0.09 g are shown in Figure S1a.

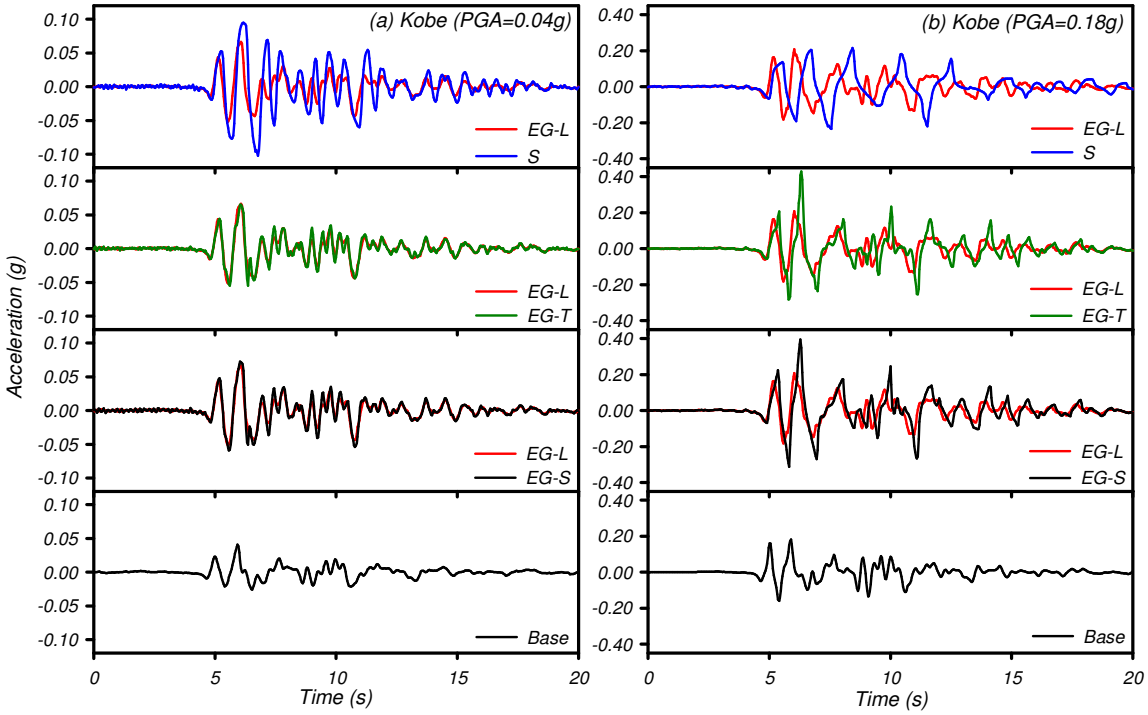

Figure 4.2. Recorded accelerations in the soil and embedded grid sides (EG with A_r = 24%) of MKH01 during (a) Kobe motion with PBA = 0.04g, (b) Kobe motion with PBA = 0.18g.

The acceleration responses of the embedded grid side (EG, A_r = 33%) in test MKH03 are shown in Figure 4.3 for Kobe motions with a PBA = 0.04 g (Figure 4.3a) and 0.16 g (Figure 4.3b). The reinforced soil surface (EG-S) had a PHA = 0.066g in the PBA = 0.04 g event (an amplification ratio of 1.65) and a PHA = 0.20g in the PBA = 0.16g event (an amplification ratio of 1.25). The slightly lower amplification ratio at the stronger shaking level would be consistent with the expected effect of some nonlinearity in the system. The accelerations on the longitudinal walls (EG-L), transverse walls (EG-T), and enclosed soil (EG-S) are all similar, suggesting that the transverse walls in these tests with A_r = 33% did not develop the degree of flexure observed in the test with A_r = 24%. The acceleration responses during an intermediate Kobe motion with PBA = 0.07 g are shown in Figure S1b.

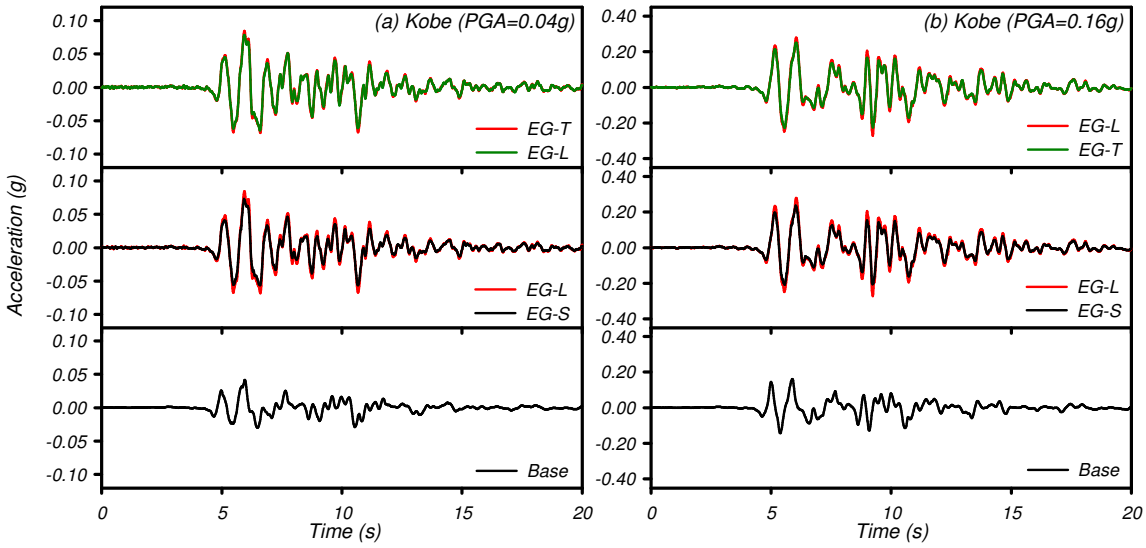

Figure 4.3. Recorded accelerations in the embedded grid side (EG with Ar = 33%) of MKH03 during (a) Kobe motion with PBA = 0.04g, (b) Kobe motion with PBA = 0.16g.

The acceleration responses of the floating grid (FG, A_r = 33%) in test MKH03 are shown in Figure 4.4 for Kobe motions with PBA = 0.04 g (Figure 4.4a) and 0.16 g (Figure 4.4b). The reinforced soil surface (FG-S) had a PHA = 0.073g in the PBA = 0.04 g event (an amplification ratio of 1.83) and a PHA = 0.17g in the PBA = 0.16g event (an amplification ratio of 1.06). The significantly lower amplification ratio at the stronger shaking level is again attributed to the effects of nonlinearity in the system, likely in the clay underneath the grid. The accelerations on the longitudinal walls (FG-L), transverse walls (FG-T), and enclosed soil (FG-S) are all similar, again suggesting that the transverse walls in these tests with A_r = 33% did not develop the degree of flexure observed in the test with A_r = 24%.

4.3.2 Pore Water Pressures and Settlements

The pore water pressures measured in the unreinforced soil and embedded grid sides (EG, A_r = 24%) of model MKH01 are shown in Figure 4.5 for the same Kobe motions with PBA = 0.04g (Figure 4.5a) and 0.18g (Figure 4.5b). For the PBA = 0.04g event, the EPWP ratios, $r_u = \Delta u/\sigma'_{vc}$, ranged from 0.04 to 0.17 in the unreinforced soil and from 0.03 to 0.06 inside the embedded grid. The maximum r_u values occurred at a depth of 5.1 m (σ'_{vc} = 42 kPa) on both sides. The r_u values were slightly lower inside the embedded grid (EG, A_r = 24%) than in the unreinforced soil (S), which may be because the embedded grid had a

lower PHA (0.069g versus 0.096g; Figure 4.2a); this suggests that the soil-cement grid reduced the dynamic stresses and strains imposed on the enclosed soil at this low shaking level. For the PBA = 0.18g event, the r_u values ranged from 0.23 to 0.65 in the unreinforced soil and from 0.28 to 0.62 inside the embedded grid, with the higher r_u values occurring at the shallowest depths on both sides. These r_u values are similar despite the embedded grid having a much greater PHA (0.37g versus 0.22g); this suggests the soil-cement grid may have reduced the dynamic stresses and strains imposed on the enclosed soils by an amount that compensated for the stronger shaking. The differences in EPWPs in the unreinforced soil and inside the grids may also have been affected by differences in their local drainage boundary conditions, although these effects are likely to have been small during the time of shaking. Partitioning of the dynamic loads between the soil-cement grid and enclosed soil is discussed in more detail in following sections.

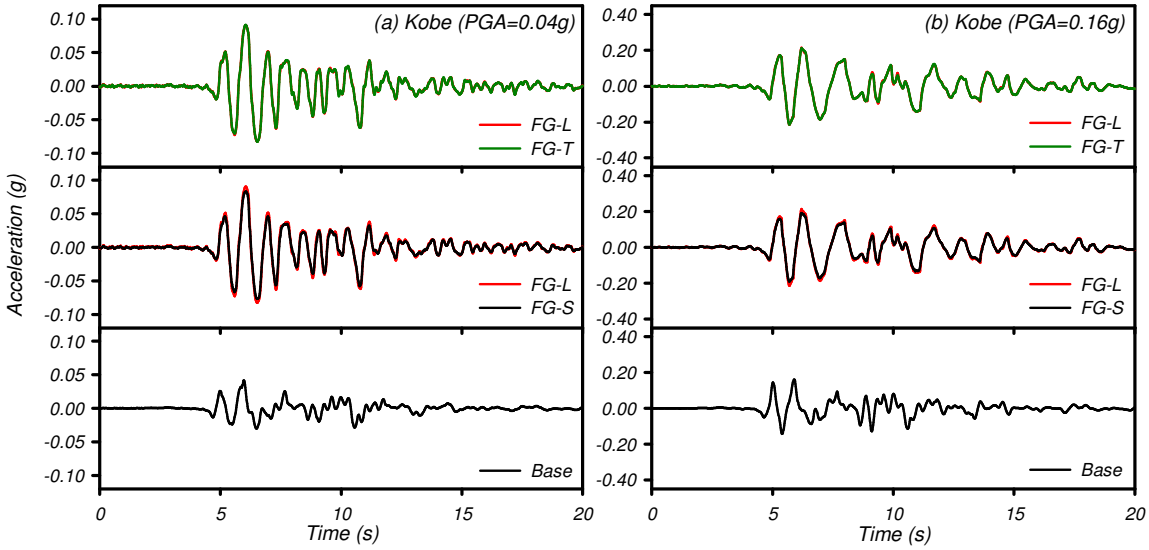

Figure 4.4. Recorded accelerations in the floating grid side (FG with A_r = 33%) of MKH03 during (a) Kobe motion with PBA = 0.04g, (b) Kobe motion with PBA = 0.16g.

The pore water pressures measured on the floating grid (FG, A_r = 33%) and embedded grid (EG, A_r = 33%) sides in model MKH03 are shown in Figure 4.6 for the same Kobe motions as in Figures 3 and 4. Note that the EPWP measured at a depth of 17.7 m (σ'_{vc} = 150 kPa) is below the soil-cement grid on the floating grid side. For the PBA = 0.04g event, the r_u values in the floating and embedded grids were all less than about 0.06. For the PBA = 0.16g event, the r_u values ranged from 0.24 to 0.32 inside the floating grid and from 0.21 to 0.27 inside the embedded grid; the r_u values inside the floating grid are slightly greater

although it developed a slightly lower PHA (0.17g versus 0.20g). The r_u value was 0.18 in the clay below the floating grid compared to 0.24 inside the embedded grid at the same depth (i.e., σ'_{vc} = 150 kPa in Figure 4.6).

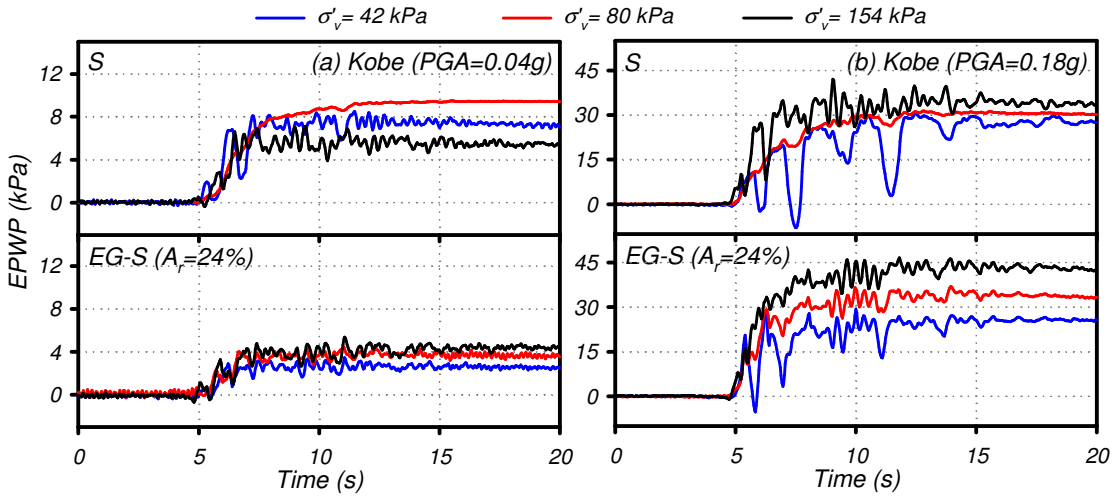

Figure 4.5. Excess pore water pressures in the soil and embedded grid sides (EG with Ar = 24%) of MKH01 during (a) Kobe motion with PBA = 0.04g, (b) Kobe motion with PBA = 0.18g.

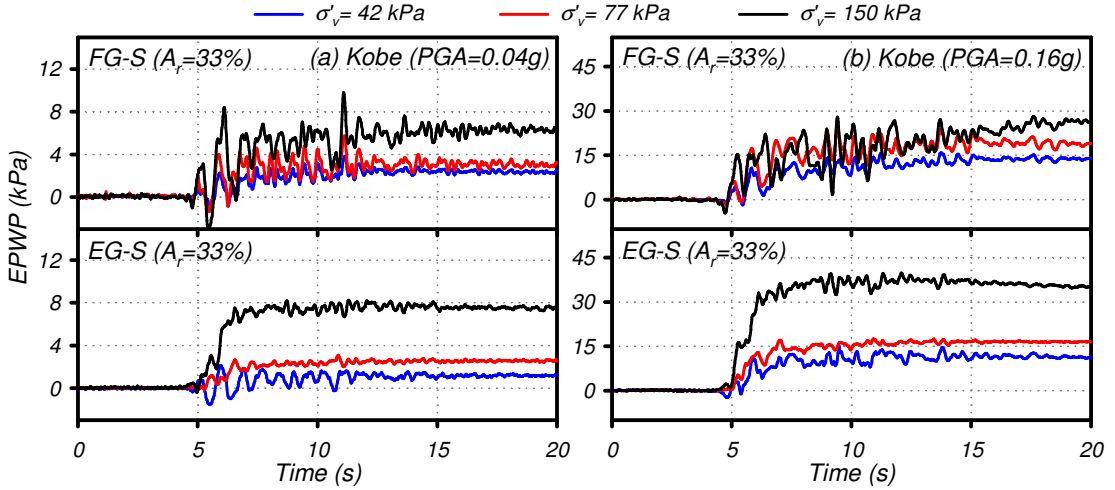

Figure 4.6. Excess pore water pressures in floating and embedded grid sides (FG and EG with A_r = 33%) of MKH03 during (a) Kobe motion with PBA = 0.04g, (b) Kobe motion with PBA = 0.16g.

Incremental settlements for the soil, embedded grids, and floating grid for both MKH01 and MKH03 are summarized in Figure 4.7. Incremental shaking-induced settlements measured above the soil-cement panels were found significantly lower than those observed in the unreinforced soft clay. For the reinforced sides of MKH01 and MKH03, incremental settlements of embedded and floating grids were generally smaller than 3 cm, while for the soil side of MKH01 during a Kobe motion with PBA = 0.18 g, settlement of 15.0 cm was measured. The Kobe motion produced greater settlements than the TCU motion for the

same PHA because it is richer in low frequency content and this produced a stronger dynamic response and greater shear strains for these models. These settlements were measured on small reaction plates embedded in the thin sand layer placed over top of the soil and soil-cement grids, and thus some of the measured settlement may be attributed to movement of these plates relative to the soil-cement panels themselves.

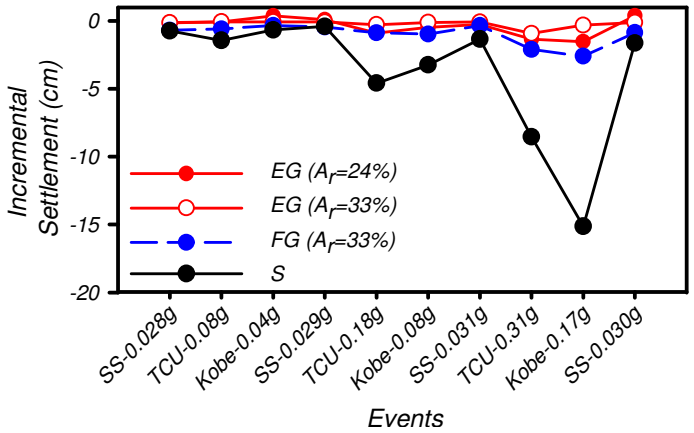

Figure 4.7. Incremental settlements of soil and embedded grid (EG with A_r = 24%) in MKH01 and floating and embedded grids (FG and EG with A_r = 33%) in MKH03 during all shaking events

4.3.3 Response Spectra

Acceleration response spectra (linear elastic, 5% damping, pseudo spectral acceleration) for motions recorded in MKH01 for a Kobe motion with PBA = 0.18g are shown in Figure 4.8. Spectra for motions on the embedded grid side (EG, A_r = 24%), are shown in Figure 4.8a, including the container base (Base), ground surface (EG-S; 6 recordings), longitudinal walls (EG-L; 2 recordings), and transverse walls (EG-T; 2 recordings). The wall motions generally correspond to points located midway between grid intersections, as shown by the sensor positions in Figure 4.1. The spectral values for the soil surface (EG-S) and walls (EG-T and EG-L) were all amplified relative to the base motion for all periods. The spectral values for the enclosed soil (EG-S) and transverse walls (EG-T) were similar, and were approximately twice as large as the spectra values for the longitudinal (EG-L) walls. These differences in response suggest that the transverse walls and the soil inside the grids were moving relative to the longitudinal walls, which again implies significantly flexural deformation within the transverse walls. Spectra for motions on the unreinforced soil side are shown in Figure 4.8b, including the container base, ground surface (S), and the top ring of the container (C). For the unreinforced soil profile (S), the

spectral values at periods larger than about T = 0.8 sec were strongly amplified relative to the base motion, whereas the spectral values at shorter periods were similar to those for the base motion (Figure 4.8b). The greatest amplification of spectral values at the soil surface was at periods of about 1.5 sec, which corresponds to the estimated effective natural period of the unreinforced soil profile. The spectral values for the top container ring (C) were comparable to that for the longitudinal walls (EG-L) and considerably different from those for the unreinforced soil (S). The large differences in responses between the top container ring (C) relative to the various points on the soil and embedded grid sides of the model (Figures 4.8a and 4.8b) illustrate that dynamic analyses of these models will need to explicitly include the container to capture these complex interactions.

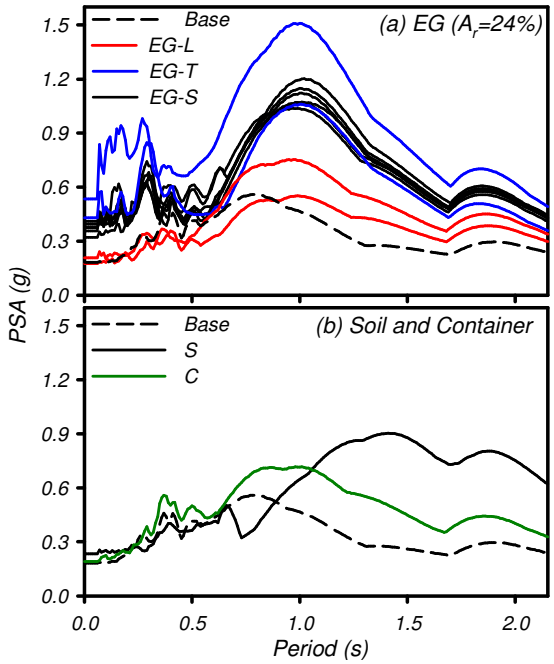

Figure 4.8. Pseudo spectral accelerations in MKH01 during Kobe motion with PBA = 0.18g: (a) on the embedded grid side, (b) on the soil side and the container top ring

Acceleration response spectra for motions recorded in MKH03 for the Kobe motion with PBA=0.16g are shown in Figure 4.9. Spectra for motions on the embedded grid side are shown in Figure 4.9a, including the container base (Base), the enclosed soil (EG-S; 2 recordings), longitudinal walls (EG-L; 2 recordings), and transverse walls (EG-T; 2 recordings). The responses of the embedded grid and the soil inside the grid are all similarly amplified relative to the base motion at all periods, with the responses on the transverse walls (EG-T) being slightly greater than on the longitudinal walls (EG-L), which in turn

are slightly greater than on the soil inside the grids (EG-S). Spectra for motions on the floating grid side are shown in Figure 4.9b, including the container base, enclosed soil (FG-S; 2 recordings), longitudinal walls (FG-L; 2 recordings), and transverse walls (FG-T; 2 recordings). The responses of the transverse and longitudinal walls (FG-T and FG-L) are comparable to each other at all periods, are comparable to the base motion at periods less than about 0.7 s, and are amplified relative to the base motion at longer periods. The response of the soil inside the floating grid (FG-S) is comparable to those of the grid walls at periods less than 0.7 s, and slightly less than those for the grid walls at longer periods. The differences in the response spectra for the floating grid (Figure 4.9b) and embedded grid (Figure 4.9a) are consistent with the expected effects of nonlinearity in the soft clay beneath the floating grid; i.e., a lengthening of the system's effective period producing less amplification of short-period motions and greater amplification of longer-period motions. The similarity of the response spectra for the transverse and longitudinal walls for the embedded grid (Figure 4.9a) and for the floating grid (Figure 4.9b) suggest that flexural deformation of the transverse walls in these grids with A_r = 33% was much smaller than for the embedded grids of test MKH01 with the smaller A_r = 24% (Figure 4.8). Spectra for the top container ring (C), as shown in Figure 4.9c, are most comparable to the spectra for the floating grid (Figure 4.9b) and lack the short period motions evident in the spectra for the embedded grid (Figure 4.9a).

Spectral amplification ratios for test MKH01 with the small, intermediate, and strong Kobe motions (PBA of 0.04, 0.09, and 0.18g) are shown in Figure 4.10. The spectral amplification ratios are the spectra for motions recorded near the ground surface divided by those for the base motion. For unreinforced soil profiles (S, Figure 4.10a), the low amplitude base motion of PBA ≈ 0.04g produced amplification of spectral values at all periods. With increasing intensity of base motion, the effective period of the soil profile lengthened and the spectral amplification ratios at periods less than about 1.0 s progressively decreased. For the embedded grid (EG, A_r = 24%), the spectral amplification ratios for the PBA = 0.18g event showed greater differences from those for the lower intensity motions, suggesting that the grid system, with its smaller A_r, was developing nonlinearity at this shaking level (Figure 4.10b).

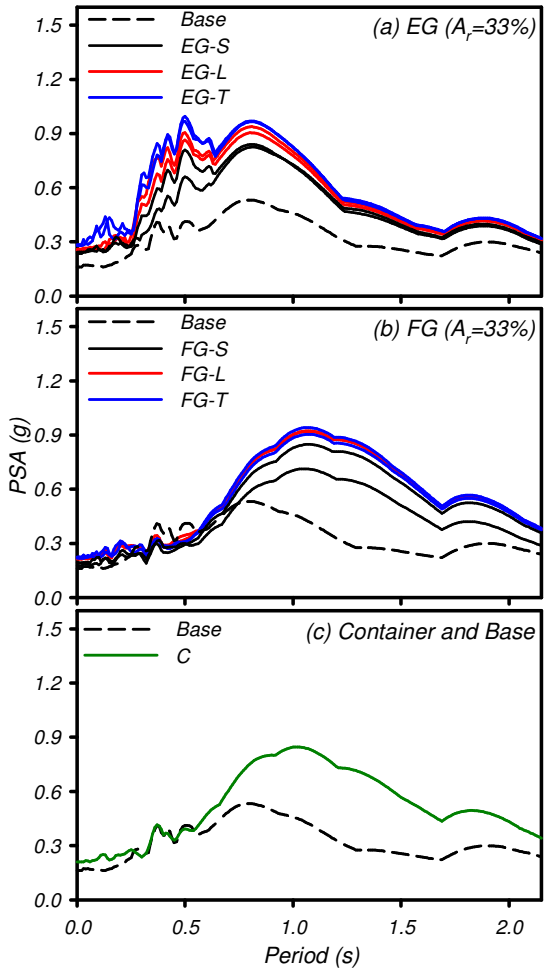

Figure 4.9. Pseudo spectral accelerations in MKH03 during Kobe motion with PBA = 0.16g: (a) on the embedded grid side, (b) on the floating grid side, and (c) on the container top ring and base

Spectral amplification ratios for test MKH03 with the small, intermediate, and strong Kobe motions (PBA of 0.04, 0.07, and 0.16g) are shown in Figure 4.11. For the embedded grid (EG, A_r = 33%), the spectral amplification ratios were similar at all periods and did not vary significantly with shaking intensity (Figure 4.11b), which suggests a relatively stiff and linear response for this grid system. For the floating grid (FG, A_r = 33%), the spectral ratios were intermediate to those for the unreinforced soil (Figure 4.10a) and the embedded grid systems (Figures 4.10b and 4.11b).

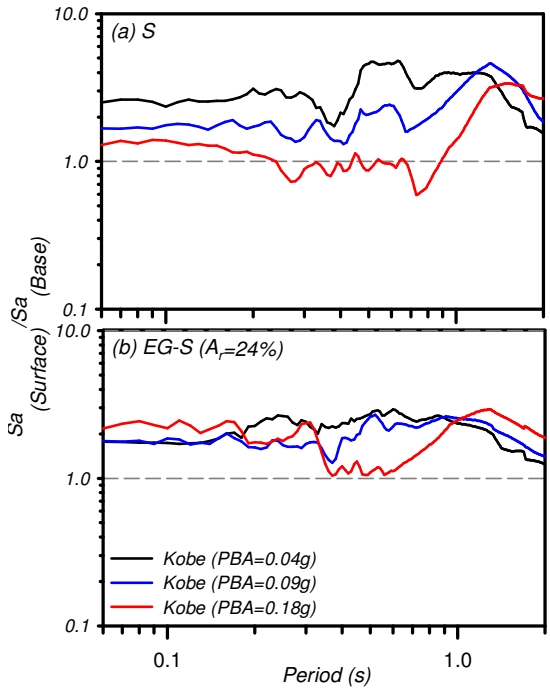

Figure 4.10. Pseudo spectral amplification ratios between the ground surface and the container base in MKH01 during Kobe motions with PBA of 0.04g, 0.09g, and 0.18g: (a) on the soil side, (b) on the soil inside the embedded grid (EG with A_r = 24%)

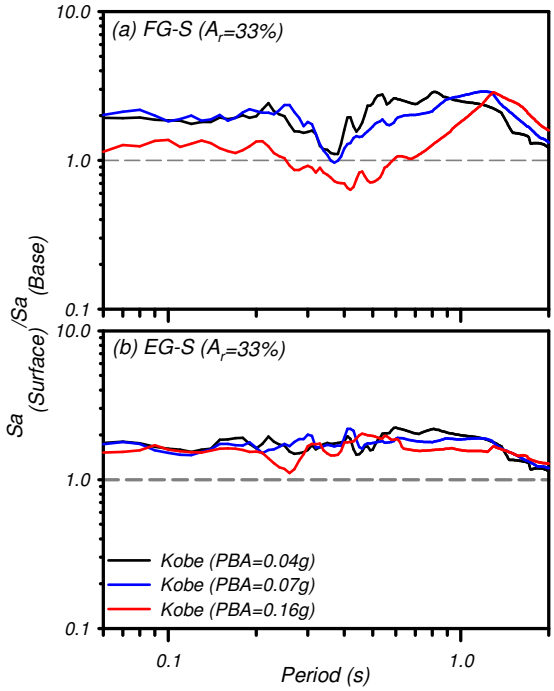

Figure 4.11. Pseudo spectral amplification ratios between the ground surface and the container base in MKH03 during Kobe motions with PBA of 0.04g, 0.07g, and 0.16g: (a) on the soil inside the floating grid (FG with A_r = 33%), (b) on the soil inside the embedded grid (EG with A_r = 33%)

4.3.4 Cracking of Soil-Cement Grids

Cracking of the soil-cement grids was monitored during shaking events using local crack detecting sensors and then mapped from visual inspection during final model excavation. The crack detecting sensors, which were brittle conductors embedded in the soil-cement walls, provided a binary indication of if, and when, a sensor was cracked. The sensors show a large change in conductivity if an open crack develops anywhere along their length. The change in conductivity is temporary if the crack later closes and contact is reestablished between both sides of the cracked conductor. The sensor signal does not provide information on the magnitude of the crack opening. More details on the crack detecting sensors can be found in Khosravi et al. (2015a,c,e).

The crack detectors showed that cracking was very limited during the shaking events described herein (i.e., few minor cracks across the grid surface) and that the detected cracks occurred at either the mid-length of the panels perpendicular to the shaking or at the corners of grid cells. The embedded grid (EG, A_r = 24%) of MKH01 developed few cracks during

the Kobe motion with PBA = 0.18g (event 10 in Table 4.1), but no cracks were detected during any of the preceding shaking events, including a TCU motion with PBA = 0.31g (event 9 in Table 4.1). The floating (FG, A_r = 33%) and embedded grid (EG, A_r = 33%) of MKH03 had no cracks detected in any of the shaking events. Visual inspection of the grid surfaces in MKH03 after testing also showed no signs of deep cracking on the surface. A schematic of the embedded grid in MKH01 with the locations of the crack detecting sensors and any visible post-testing cracks is provided in Figure S13.

4.3.5 Dynamic Stress-Strain Responses

Dynamic shear stress and shear strain time series for the unreinforced soil profile and the composite grid systems were computed at different depths using data from the vertical arrays of accelerometers. These analyses assumed a one dimensional (1-D) shear beam condition and used the procedures presented in Brandenberg et al. (2009) and Kamai and Boulanger (2010). Shear strains were computed by double integrating the accelerations to obtain horizontal displacements, and then differentiating those displacements with respect to depth to get the shear strain. This differentiation was performed using a weighted residual method (Brandenberg et al. 2009). The accelerations were filtered with a high-pass 4^{th} order Butterworth filter with a corner frequency (f_c) of 0.3 Hz, which is based on the data acquisitions system's known signal characteristics. Application of this method produces shear stress and shear strain values that are averages for the composite behavior of the reinforced grids. These average stress-strain responses do not distinguish how the shear stresses are distributed between the soil-cement grid and enclosed soil, but they do provide a basis for evaluating how the grid affected overall system stiffness.

Average shear stress–shear strain responses at depths of 5.1 and 13.7 m in the unreinforced soil (S) and embedded grid (EG) sides of model MKH01 are compared in Figure 4.12 for small, intermediate, and strong Kobe motions (PBA of 0.04, 0.09, and 0.18g), For the unreinforced soil profile (S), the shear stress-strain responses progressed from relatively linear in the small Kobe motion to strongly nonlinear in the strong Kobe motion; peak shear strains in the soil profile were 0.2%, 1%, and 2.5% at PBA of 0.04, 0.09, and 0.18g, respectively. For the embedded grid (EG, A_r = 24%), the average stress-strain response was notably stiffer than for the unreinforced soil; peak shear strains were

only about 0.8% in the strong Kobe motion (about 1/3 the 2.5% in the unreinforced soil) despite the peak shear stresses in the embedded grid being about 40% greater than in the unreinforced soil.

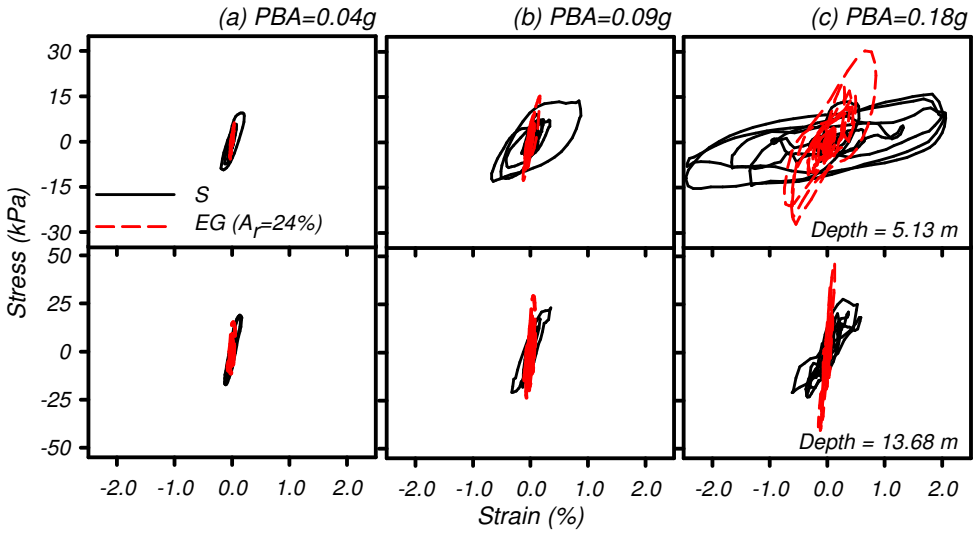

Figure 4.12. Average shear stress versus shear strain responses at depths of 5.1 and 13.7 m in the soil and embedded grid of MKH01 during Kobe motions with: (a) PBA = 0.04g, (b) PBA = 0.09g, (c) PBA = 0.18g.

Average shear stress–shear strain responses at depths of 5.8 and 14.2 m on the floating (FG) and embedded (EG) grid sides of model MKH03 are compared in in Figure 4.13 for the same series of Kobe motions compared in Figure 4.12. Note that the depth of 14.2 m on the floating grid side of the model is in the soft clay beneath the grid. At a depth of 5.8 m, the stress-strain responses for floating and embedded grids, both with A_r = 33%, were nearly linear with quite similar shape and peak shear strains. At a depth of 14.2 m, the clay beneath the floating grid developed strong nonlinearity with a peak shear strain of about 1% during the PBA = 0.16g event, whereas the embedded grid was notably stiffer with peak shear strains that were approximately 80% smaller.

4.4 Evaluation of Peak Shear Stress Demands on Grids and the Potential for Cracking

The potential for cracking in the soil-cement grids depends on the dynamic shear and tensile stresses that develop and the tensile strength of the soil cement. The dynamic shear stresses that developed in the walls can be estimated by first computing the average shear stresses in the grid system and then estimating how those stresses are partitioned between the walls and enclosed soil. The additional stresses that develop due to flexure, particularly

in the transverse walls, are more difficult to evaluate. This section presents a first-order evaluation of shear stress demands on the grids and potential for cracking, after which the effects of flexure and other stress concentrations are qualitatively discussed.

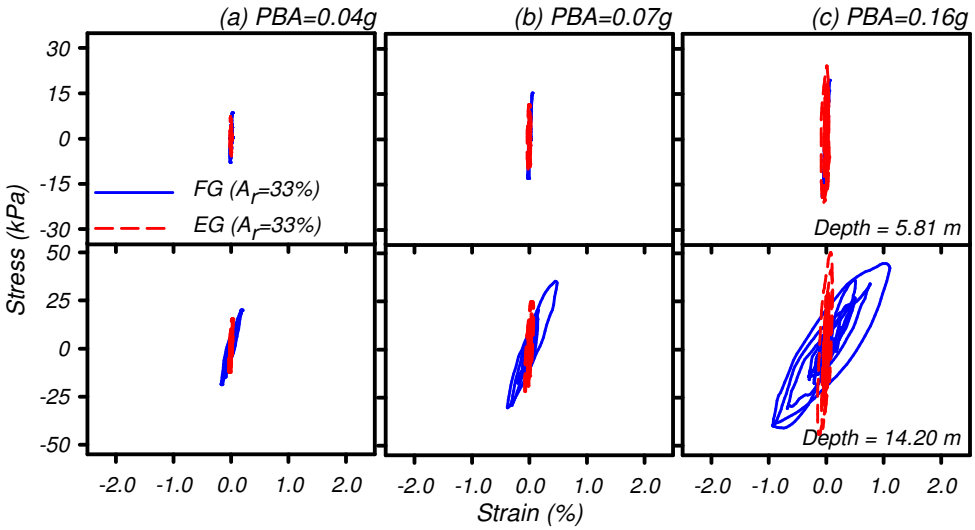

Figure 4.13. Average shear stress versus shear strain responses at depths of 5.8 and 14.2 m on the floating and embedded grid sides of MKH03 during Kobe motions with: (a) PBA = 0.04g, (b) PBA = 0.07g, (c) PBA = 0.16g.

The soil-cement tensile strength, σ_t, was estimated as 15% of the unconfined compressive strength, UCS (Kitazume and Terashi 2014). Using the average values of UCS for the soil cement specimens, the estimated values of σ_t for tests MKH01 and MKH03 were 73 kPa and 109 kPa, respectively.

Profiles of the peak average dynamic shear stresses imposed on the embedded grids during the strongest Kobe and TCU motions for MKH01 (EG with A_r = 24%) and MKH03 (EG with A_r = 33%) tests are shown in Figures 4.14a and 4.14b, respectively. The partitioning of these average shear stress demands between the soil-cement walls and enclosed soil was estimated using the equations developed by Nguyen et al. (2013) based on linear elastic, 3D finite element analyses of unit cells. The shear stresses carried by the walls (τ_{wall}) and enclosed soil (τ_{soil}) can be related to the average shear stress across the composite system (τ_{av}) as:

$$\tau_{Soil} = \tau_{av} \times \left(\frac{1}{G_r \times \left[A_r \,.\, C_G \,.\, \gamma_r + \frac{1}{G_r} . (1 - A_r) \right]} \right) \quad (1)$$

$$\tau_{wall} = \tau_{av} \times \left(\frac{1}{A_r \,.\, C_G + \frac{1}{\gamma_r . G_r} . (1 - A_r)} \right) \quad (2)$$

where

$$\gamma_r = \left[1 - (1 - A_r)^{1.3}.\left(\frac{G_r - 1}{185}\right)^{0.4}\right].\min\left(\frac{H}{S}, 1\right) \quad (3)$$

$$C_G = 1 - 0.5.\sqrt{1 - A_r} \quad (4)$$

where G_r = shear modulus ratio ($G_r = G_{wall}/G_{soil}$); H = soil-cement wall height; and S = grid spacing. The value of G_r was estimated to be between 5 and 10 based on correlations between elastic properties and UCS for soil-cement mixtures (Kitazume and Terashi 2014). The peak shear stresses that develop in the soil-cement walls and enclosed soil, as a ratio of the average stresses carried by the composite system, were computed using the above expressions as τ_{wall}/τ_{av} = 3.2-4.3 and τ_{soil}/τ_{av} = 0.55-0.75 for the A_r = 24% grid (MKH01) and τ_{wall}/τ_{av} = 2.8-3.7 and τ_{soil}/τ_{av} = 0.44-0.66 for the A_r = 33% grid (MKH03).

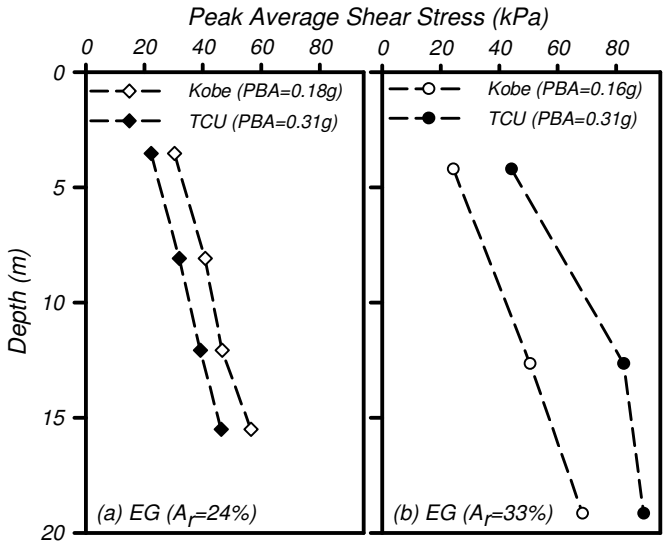

Figure 4.14. Peak average shear stress profiles during a Kobe motion with an average PBA = 0.17g and a TCU motion with an average PBA = 0.31g: (a) embedded grid side of MKH01, and (b) embedded grid side of MKH03

The initial and dynamic stress states for a soil-cement element in a longitudinal wall are schematically shown in Figure 4.15. The loading of longitudinal walls in the present tests is dominated by shear stresses, such that any flexure is neglected for the purpose of this example. The vertical stress in the walls is assumed to equal the average total vertical stress in the grid system (i.e., no arching of vertical stresses onto the walls), and the horizontal stress is assumed to equal to 0.5 times the vertical stress based on a Poisson's ratio, ν = 0.35 (Bruce et al. 2014). The dynamic shear stresses cause the Mohr circle to

grow, such that tensile stresses can develop under strong enough shear loading. Cracking would be expected when the principal tensile stress exceeds the tensile strength of the soil-cement material, σ_t. Consider a point in test MKH01 at a depth of 4.3 m (2.0 m below the top of the grid walls) where the total vertical stress is 75 kPa and the total horizontal stress is estimated to be 58 kPa; in this case, it would take a shear stress of 140 kPa to reduce the minor principal stress to the tensile strength of 73 kPa if the vertical and horizontal stresses remain constant. If the initial horizontal stress in the wall is instead assumed equal to the vertical stress, then it would take a shear stress of 149 kPa to bring σ_3 to σ_t which is not significantly different than the first estimate of 140 kPa.

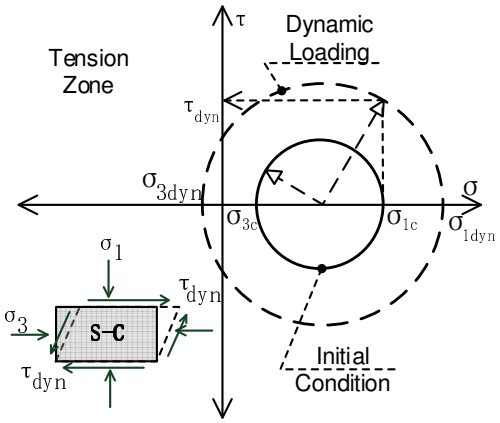

Figure 4.15. Mohr circle showing initial and dynamic stresses on a soil-cement element in a longitudinal panel

Profiles of the estimated minimum values of the minor principle stress in the longitudinal walls of MKH01 (EG, A_r = 24%) for the strongest TCU (PBA ≈ 0.31g) and Kobe (PBA ≈ 0.17g) motions are presented in Figure 4.16a for G_r of 5.0 and 10. The soil-cement would have been in tension over the upper 5 m of the walls during the Kobe motion with G_r = 10, although the tensile stresses would have been less than the estimated tensile strength of the soil-cement material. The maximum tensile stress was 40 kPa near the top of the wall, which is a bit more than half the estimated tensile strength of 73 kPa. The strongest TCU motion, on the other hand, would not be expected to create tension in the longitudinal walls for either value of G_r. These results are consistent with the observation of minor cracking in the strong Kobe motion not in the preceding strong TCU motion.

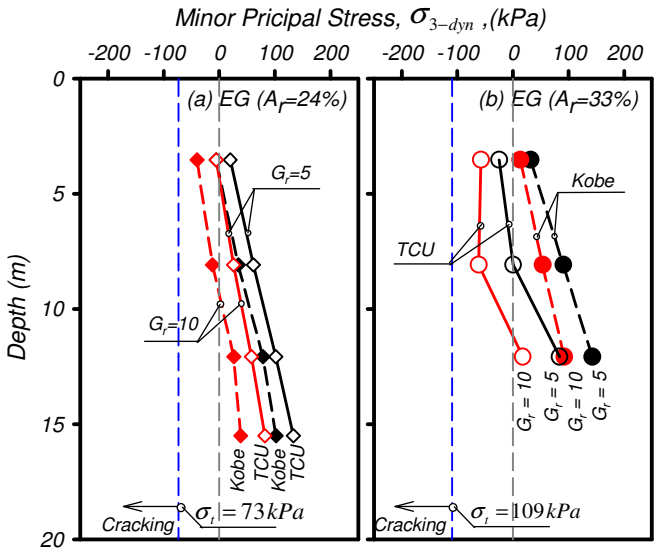

Figure 4.16. Profiles of minimum minor principal stress in the longitudinal soil-cement panels for Gr values of 5.0 and 7.5 during the strong Kobe (average PBA = 0.17g) and TCU (average PBA = 0.31g) motions: (a) embedded grid of MKH01, and (b) embedded grid of MKH03

Profiles of the estimated minimum values of the minor principle stress in the longitudinal walls of MKH03 (EG, A_r = 33%) for the strongest TCU and Kobe motions are presented in Figure 4.16b for G_r of 5.0 and 10. The soil-cement would have been in tension over the upper 7 m of the walls during the TCU motion with G_r = 10, although the tensile stresses would have been less than half the estimated tensile strength. The strongest Kobe motion, would not be expected to create tension in the longitudinal walls for either value of G_r. These results are consistent with the absence of cracking in either motion.

Tensile stresses and strains can also develop due to flexure of the walls, which is of particular importance for the transverse walls in these tests. Flexural strain of the transverse walls in a grid should be proportional to the relative displacement between the transverse and longitudinal walls. Displacement time series (relative to the container base) for midpoints on the transverse (EG-T) and longitudinal (EG-L) walls of the embedded grids in model MKH01 and MKH02 during the stronger Kobe motion (PBA ≈ 0.17 g) are shown in Figures 4.17a and 4.17b, respectively. For the embedded grid with A_r = 24% (Figure 4.17a), the transverse walls developed significantly greater displacements than the longitudinal walls; the peak displacement of the transverse walls (12.7 cm) was more than double the peak displacement of the longitudinal walls (4.9 cm). For the embedded grid with A_r = 33% (Figure 4.17b), the displacements for the transverse and longitudinal walls

were almost equal. These results suggest that flexural strains in the transverse walls of the embedded grid with $A_r = 24\%$ were much more significant than for the grid with $A_r = 33\%$. This difference in the observed flexure of the transverse walls, in combination with the above analyses of tensile stresses due to shear loading, is consistent the observed minor cracking in MKH01 ($A_r = 24\%$) and the absence of cracking in MKH03 ($A_r = 24\%$).

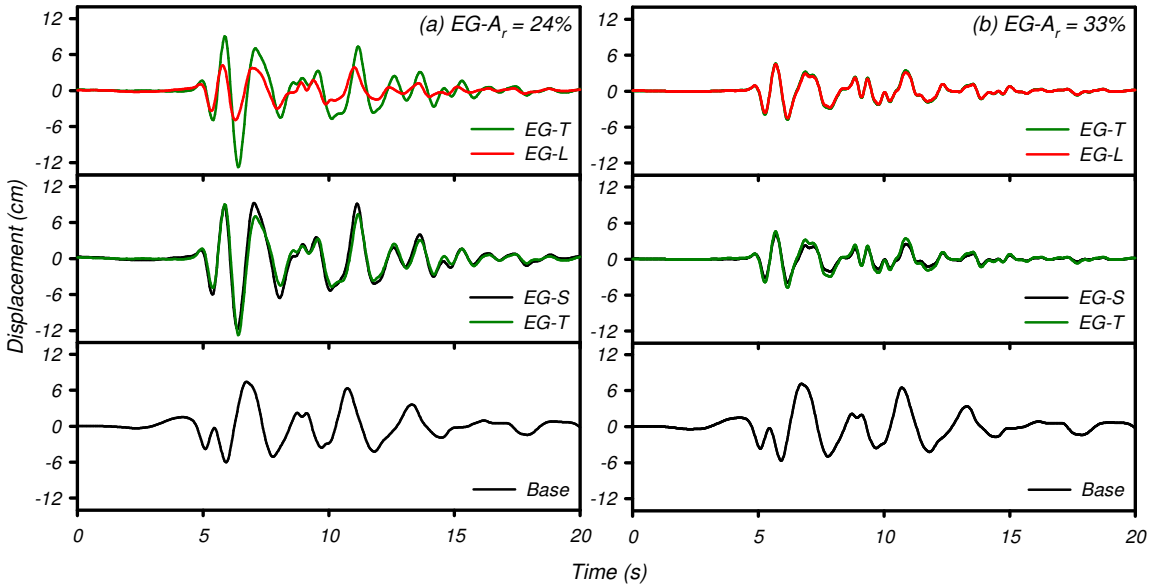

Figure 4.17. Displacements during Kobe motion with an average PBA = 0.17g in the embedded grid sides (a) EG with $A_r = 24\%$ in MKH01, (b) EG with $A_r = 33\%$ in MKH03.

4.5 Conclusion

A series of large centrifuge models was used to study the effects of soil-cement grid reinforcement on the seismic response of a deep, lightly over-consolidated clay profile. The model tests included an unreinforced soil profile and soil profiles reinforced with three different grid configurations. Recorded responses during 13 different shaking events were used to examine the nonlinear response characteristics of the unreinforced and reinforced profiles, and the internal interactions between the soil-cement grids and enclosed soils. The experimental data were archived (Khosravi et al. 2015c,e) for public distribution and use in the validation of numerical analysis methods.

The soft clay profile, without any reinforcement, developed strong nonlinearity at the stronger levels of shaking. The soft clay developed peak shear strains up to 2.5% and peak r_u values of 78% for the stronger Kobe motion (PBA = 0.18g), accompanied by significant lengthening of the soil profile's effective natural period.

The embedded grid with A_r = 24% significantly stiffened the site compared to the site with no reinforcement, resulting in stronger accelerations at the ground surface for the input motions used in this study. The soil-cement grid showed some nonlinearity in its response during the stronger shaking events; e.g., the Kobe motion with PBA = 0.18g produced peak shear strains up to 1% and r_u values of 100% in the reinforced soil and minor cracking in the soil-cement walls. The dynamic horizontal displacements of the transverse walls and enclosed soils were significantly greater than those for the longitudinal walls, indicating significant flexure in the transverse grid walls.

The embedded grid with A_r = 33% further stiffened the site and also produced stronger accelerations at the ground surface. The soil-cement grid did not, however, exhibit signs of significant nonlinearity in its response for any of the imposed shaking events; e.g., the Kobe motion with PBA = 0.16g produced peak shear strains of only 0.15% in the reinforced soil and no cracking in the soil-cement walls. The dynamic horizontal displacements of the transverse walls, enclosed soils, and longitudinal walls were essentially the same, indicative of relatively minor flexure in the transverse grid walls.

The floating grid with A_r = 33% effectively stiffened the upper portion of the clay profile, but its dynamic response was affected by strong nonlinearity in the soft clay beneath the grid during the strong shaking events; e.g., the Kobe motion with PBA = 0.16g produced peak shear strains up to 1.0% in clay beneath the grids, whereas the clay inside the grid cells remained relatively linear. Spectral amplification ratios were intermediate to those for the untreated soil and embedded grid (A_r = 33%), as expected. Displacements of the transverse and longitudinal walls were essentially the same and no cracking of the walls was observed.

The results of these experiments and analyses provide insights on the dynamic performance of soil-cement grids and the internal interactions between the grids and enclosed soils. The potential for tensile stresses and cracking in the longitudinal soil-cement walls was evaluated using a simplified analysis method, but the effects of transverse wall flexure and stress concentrations at grid corners will require more detailed analyses. The archived dataset provides a basis for future evaluation of these and other

issues as part of validating design and numerical analysis procedures for the seismic performance of soil-cement grid reinforcement systems.

5 Dynamic Centrifuge Tests of Structures with Shallow Foundations on Soft Clay Reinforced by Soil-Cement Grids

This chapter is produced from Khosravi et al. 2016, which has been submitted for Journal of Soils and Foundations.

Khosravi, M., Boulanger, R.W., Tamura, S., Wilson, D. W., Olgun, C.G., Wang, Y. (2016). "Dynamic Centrifuge Tests of Structures with Shallow Foundations on Soft Clay Reinforced by Soil-Cement Grids", Journal of Soils and Foundations (submitted for review)

Abstract. Centrifuge model tests are used to examine the dynamic response of structures supported by shallow foundations on soft clay reinforced by soil-cement grids. The centrifuge models involved a deep, lightly over-consolidated clay profile with three different soil-cement grid configurations. Structures on square shallow foundations were located over the central part of each soil-cement grid system. The models were subjected to multiple shaking events with peak base accelerations ranging from 0.006 to 0.546 g. The recorded responses of the structures and reinforced soil profiles are used to define the dynamic moment-rotation-settlement responses of the shallow foundations across the range of imposed shaking intensities. The soil-cement grids were effective at controlling foundation settlements for most cases; onset of more significant foundation settlements did develop for the weakest soil-cement grid configuration under the stronger shaking intensities which produced a rocking response of the structure and caused extensive crushing of the soil-cement near the edges of the shallow foundations. Alternative analysis methods for predicting the demands imposed on the soil-cement grids by the inertial loads from the overlying structures and the kinematic loading from the soil profile's dynamic response are evaluated for consistency with the observed damage patterns. The experimental data have been archived and provide a basis for future studies to evaluate numerical and design analysis methods.

5.1 Introduction

Soil-cement ground reinforcements can be an effective means for mitigation of earthquake-induced ground displacements and foundation settlements for a range of structure types, soil conditions, and seismic motions (e.g., Kitazume and Terashi 2014,

Bruce et al. 2013). Soil-cement ground reinforcements may be constructed as discrete columns or grid systems using deep mixing methods (DMM), trenching, jet grouting, or other methods. The seismic response and performance of such reinforcements has been studied using case histories (e.g. Tokimatsu et al. 1996, Yamashita et al. 2012, Tokunaga et al. 2015), dynamic centrifuge model tests (e.g. Adalier et al., 1998, Kitazume and Maruyama, 2006, Ishikawa and Asaka, 2006, Rayamajhi et al., 2014c, Takahashi et al., 2006), and numerical analyses (e.g. Namikawa et al. 2007, Bradley et al. 2013, Nguyen et al. 2013, Puebla et al. 2006, Rayamajhi et al., 2014c). These studies have demonstrated the effectiveness of soil-cement reinforcements for a range of situations, but there are still insufficient data to develop or validate design methodologies for all situations encountered in practice.

A schematic of possible damage to a soil-cement grid supporting a structure on a shallow foundation during seismic loading is shown in Figure 5.1. Damage to the upper portion of the soil-cement grid could be caused by excessive shallow foundation contact stresses which develop under the inertial loads from the overlying structure (Figure 5.1a). Damage throughout the soil-cement grid could be caused by excessive dynamic kinematic loads which develop because of the stiffness contrast between the grid and surrounding soils (Figure 5.1b). Currently available experimental and case history data do not provide sufficient information to quantify the possible effects of partial damage to the soil-cement grids, by either of the mechanisms illustrated in Figure 5.1, on their ability to limit the shallow foundation settlements.

This chapter summarizes results of centrifuge model tests examining the dynamic response of structures supported by shallow foundations on soft clay reinforced by soil-cement grids. The models were designed to examine the ability of the soil-cement grids to limit settlement of the shallow foundations even when the dynamic loading causes significant damage to the soil-cement grids. The centrifuge models examined a 23-m-thick (prototype), lightly over-consolidated clay profile with three different soil-cement grid configurations: an "embedded" soil-cement grid which penetrated the underlying dense sand layer and had an area replacement ratio $A_r = 24\%$, an "embedded" grid with $A_r = 33\%$, and a "floating" grid in the upper half of the clay layer with $A_r = 33\%$. A 2.3-m-thick

(prototype) bearing layer of coarse sand was placed over the grid-reinforced clay profile. Structures on square shallow foundations were then placed over the central part of each soil-cement grid system. The models were subjected to 13 shaking events with peak base accelerations (PBAs) ranging from 0.006 to 0.546 g. The dynamic responses of the structures and reinforced soil profiles are described, including the dynamic moment-rotation-settlement responses of the shallow foundations across the range of imposed shaking intensities. Damage to the soil-cement grids, which included extensive crushing near the edges of the shallow foundations and minor cracking at larger depths for the weakest soil-cement grid at the strongest shaking intensities, is described and related to the observed foundation settlements. Alternative analysis methods for predicting the demands imposed on the soil-cement grids by the inertial loads from the overlying structures and the kinematic loading from the soil profile's dynamic response are evaluated for consistency with the observed damage patterns. The results of these model tests and preliminary analyses provide insights on the response of soil-cement grids supporting structures on shallow foundations in soft clay deposits. The experimental data have been archived and provide a unique basis for future studies to evaluate numerical and design analysis methods.

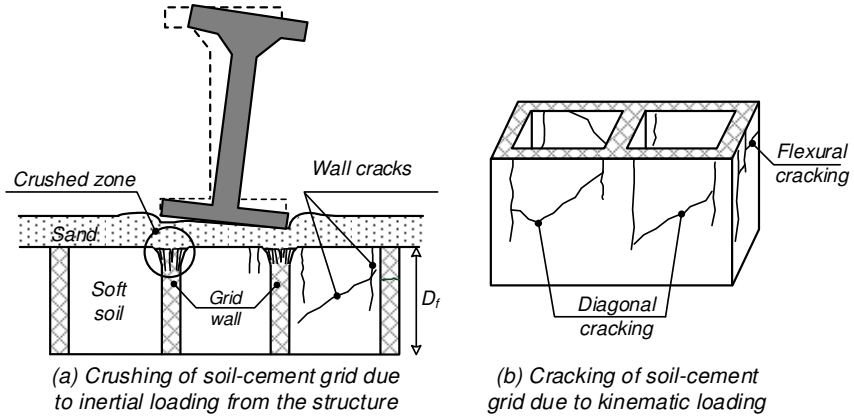

Figure 5.1. Schematic of possible damage to a soil-cement grid supporting a structure on a shallow foundation during seismic loading

5.2 Centrifuge Models

Two centrifuge tests were performed using the 9-m radius centrifuge at the University of California at Davis and the data archived for general distribution (Khosravi et al. 2015d). All tests were performed at a centrifugal acceleration of 57g. The recorded data and model

dimensions were converted into prototype units according to the scaling laws as described by Kutter (1995). All data are presented in prototype units unless otherwise specified.

All tests were performed in a hinged-plate model container. This container allows large and permanent shear strains while limiting lateral strains under static loading. The inner dimensions of the container in model scale were 1,755 mm long (100.0 m in prototype), 650 mm wide (37.0 m in prototype), and 516 mm tall (29.4 m in prototype). A 3-mm-thick rubber membrane (model scale) was attached inside the container to make it water tight.

The tests consisted of two models as shown in Figure 5.2 and described in Table 5.1. Model MKH02 had an untreated soil profile (S) on the left end of the container and an embedded soil-cement grid (EG) at right end as shown in Figure 5.2a. The area replacement ratio of the reinforced section in MKH02 was A_r = 24%. Model MKH04 had a floating soil-cement grid (FG) on the left end of the container and an embedded soil-cement grid (EG) at right end as shown in Figure 5.2b. The floating and embedded reinforced sections in MKH04 both had A_r = 33%. The soil-cement grids were constructed using the trench and excavation method (Khosravi et al. 2015a,b). Average unconfined compressive strengths for the soil-cement ($q_{u,sc}$) after 14 days of curing time were 580 and 820 kPa for MKH02 and MKH04, respectively. A structure supported by a square shallow foundation was placed over the central portion of each soil-cement grid system in both MKH02 and MKH04 (Figures 5.2a and 5.2b). The locations of select accelerometers, pore pressure transducers (PPTs), linear potentiometers (LPs), and crack detectors (CDs) are also shown in Figure 5.2.

The soil profile consisted of 23.4-m thick layer of kaolinite (Hydrite Flat DS) underlain by 2.3-m thick saturated dense sand ($D_r \approx 90\%$) for drainage purpose. A 2.3-m thick layer of coarse Monterey sand was placed over the soil-cement grids as a bearing layer for the SDOF structures. The water table was located about 0.5 m below the ground surface for all models. Properties of the kaolinite include: Liquid Limit, *LL*=47; Plastic Index, *PI*=19; specific gravity of solids, G_s=2.58; median particle size of 4.0 μm; and a coefficient of consolidation, C_v=0.7 mm^2/s in virgin loading and 2.3 mm^2/s in unloading/reloading (Khosravi et al. 2015a). A T-bar penetrometer was also used as the primary tool for directly measuring the strength of the clay during the centrifuge test (Khosravi et al. 2015 d).

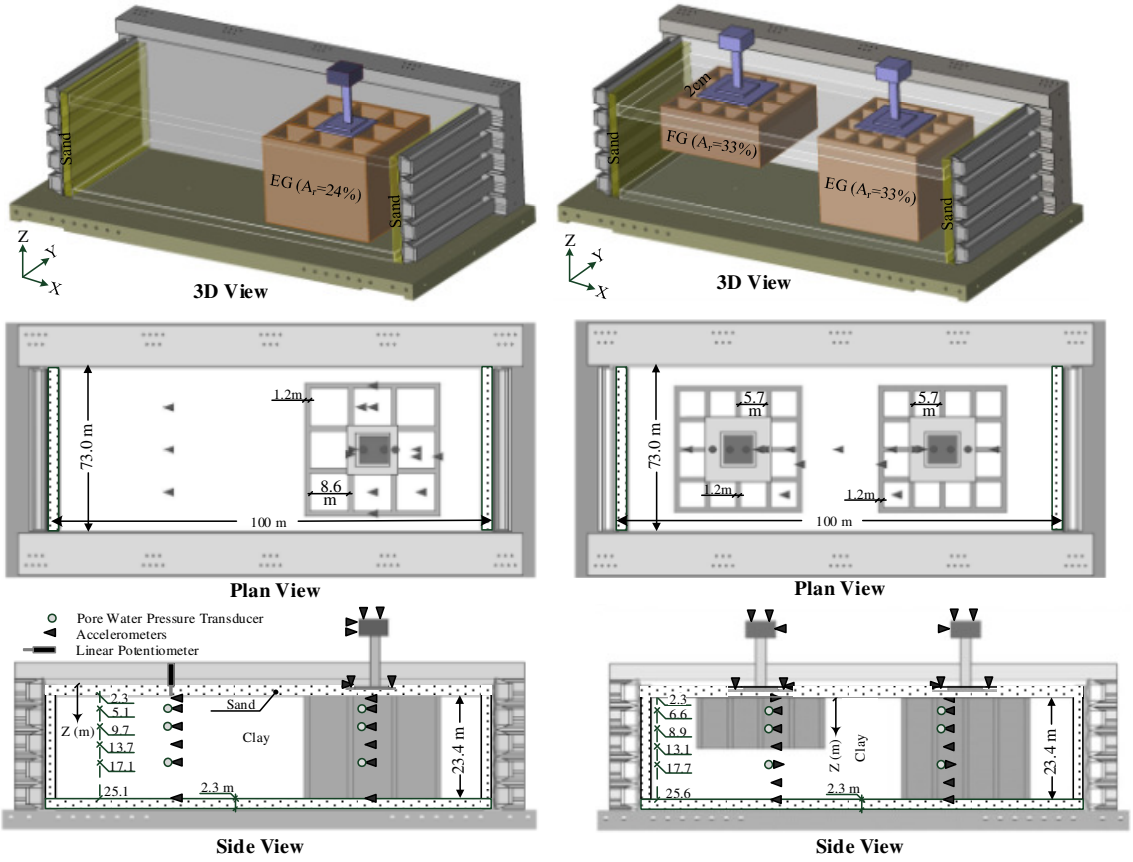

Figure 5.2. Model configurations with dimensions in prototype scale: (a) MKH02, (b) MKH04.

Table 5.1. Parameters of the soil, soil-cement grid and structure

	EG in MKH02	EG in MKH04	FG in MKH04
Area replacement ratio, A_r (%)	24	33	33
Panel spacing, S (m)	5.7	8.6	8.6
Panel thickness, t_p (m)	1.2	1.2	1.2
Reinforced depth ratio	1.0	1.0	0.5
UCS of soil-cement, $q_{u,cs}$ (kPa)	580	819	819
Sand ϕ' (degree)	40	40	40
Footing width, L (m)	11.4	14.8	14.8
Superstructure weight, V_{st} (kN)	8658	8658	8658
Footing weight, V_{ft} (kN)	3835	5866	5866
Column weight, V_{col} (kN)	307	307	307
Height of V_{st} from footing base, H_{st} (m)	13.96	13.96	13.96
Height of V_{ft} from footing base, H_{ft} (m)	0.59	0.53	0.53
Height of V_{col} from footing base, H_{col} (m)	6.59	6.59	6.59
Embedment Depth (m)	0.86	0.86	0.86

Both models, before placement of the SDOF structures on top of the grids, were shaken with 13 different motions with PBA of 0.006 to 0.32 g and peak base velocities (PBV)

ranging from 9 to 586 mm/s (Table 5.2). These shaking events were used to examine the effect of the soil-cement grids on dynamic site response, and did not cause any apparent significant damage to the grids. The dynamic responses of the reinforced soil profiles during those events and analyses of the soil-cement grids' reinforcing effects are described in Khosravi et al. (2016).

Table 5.2. Ground motions at the base of the model containers

Event No.	Motion Name	MKH02		MKH04	
		PBA g	PBV cm/s	PBA g	PBV cm/s
1	Step	0.006	0.88	0.006	0.88
2	SW7-333	0.030	3.73	0.040	4.02
3	TCU 078	0.083	7.64	0.096	9.17
4	Kobe 0807	0.042	6.62	0.044	7.30
5	SW7-333	0.031	3.75	0.040	4.25
6	TCU 078	0.178	15.58	0.197	16.85
7	Kobe 0807	0.089	12.77	0.076	12.45
8	SW7-333	0.031	3.66	0.039	16.21
9	TCU 078	0.323	26.07	0.331	26.81
10	Kobe 0807	0.188	23.98	0.158	23.50
11	SW7-333	0.033	3.95	0.035	4.08
12	Kobe 0807	0.546	58.61	0.506	57.26
13	SW7-333	-	-	0.0334	3.73

The SDOF structures were then placed over the central part of each grid system. The SDOF structures were comprised of aluminum square footings, aluminum rectangular hollow columns, and aluminum and steel block superstructures. The footing width and weight, superstructure weight, and height of the superstructure's center of mass from the footing base for all structures are summarized in Table 5.1. The fixed-based fundamental periods of the SDOF structures were all measured as 0.8 s.

The two models, with the SDOF structures in-place, were shaken with a sequence of 12 or 13 shaking events consisting of one step motion, four (for model MKH02) or five (for model MKH04) sine sweep motions, and seven earthquake motions of varying intensity and frequency. The sequence of shaking events and their PBAs for both models are provided in Table 5.2. The step motion was used to estimate the natural period of the soil profile, reinforced soil profile, and structure under essentially elastic conditions. The sine sweep motions contained continuously varying frequencies between 0.1 and 6 Hz (progressing from lower to higher frequencies) and were similarly used to evaluate the

natural periods of the system at low levels of shaking. The horizontal PBAs, as measured at the base of the container, during the sine sweep motions ranged from 0.03 to 0.06g, which were small enough to not generate measurable excess pore water pressures (EPWP). The earthquake motions were scaled versions of the recordings at station TCU-078 during the 1999 Chi-Chi earthquake and at Port Island (Kobe-0807) during the 1995 Kobe earthquake and were used to examine nonlinear responses under strong shaking. These motions were high-pass filtered to remove low-frequency displacements that were outside the range of the shaking table's capacity.

5.3 Dynamic Responses

The dynamic responses of the three soil-cement grid systems and supported SDOF structures are presented together using select motions to illustrate the observed behaviors. Responses are presented for a low- and high-intensity Kobe motion, whereas responses for all other motions can be found in the data reports (Khosravi et al. 2015d) and Supplement Figures (Appendix D).

5.3.1 Acceleration Responses

Acceleration responses of the embedded grid and supported structure in model MKH02 (EG with $A_r = 24\%$) are shown in Figure 5.3 for Kobe motions with peak base accelerations (PBA) of 0.19 g (Figure 5.3a) and 0.54 g (Figure 5.3b). Each figure shows horizontal motions recorded near the ground surface on the soil inside the grid cells (EG-S), on the footing (EG-Ft), at the center of gravity of the superstructure (EG-St), and the input base motion. For the motion with PBA = 0.19 g, as shown in Figure 5.3a, the peak horizontal acceleration (PHA) on the soil surface (EG-S) was PHA = 0.35 g (85% greater than the PBA = 0.19 g) and on the superstructure (EG-St) was PHA = 0.54g (184% greater than the PBA). The accelerations on the footing (EG-Ft) were similar to those on the soil surface (EG-S) early and late in shaking when the superstructure accelerations remained smaller than about 0.25 g, whereas they visibly differed when the shaking was strongest and superstructure accelerations repeatedly exceeded about 0.25 g.

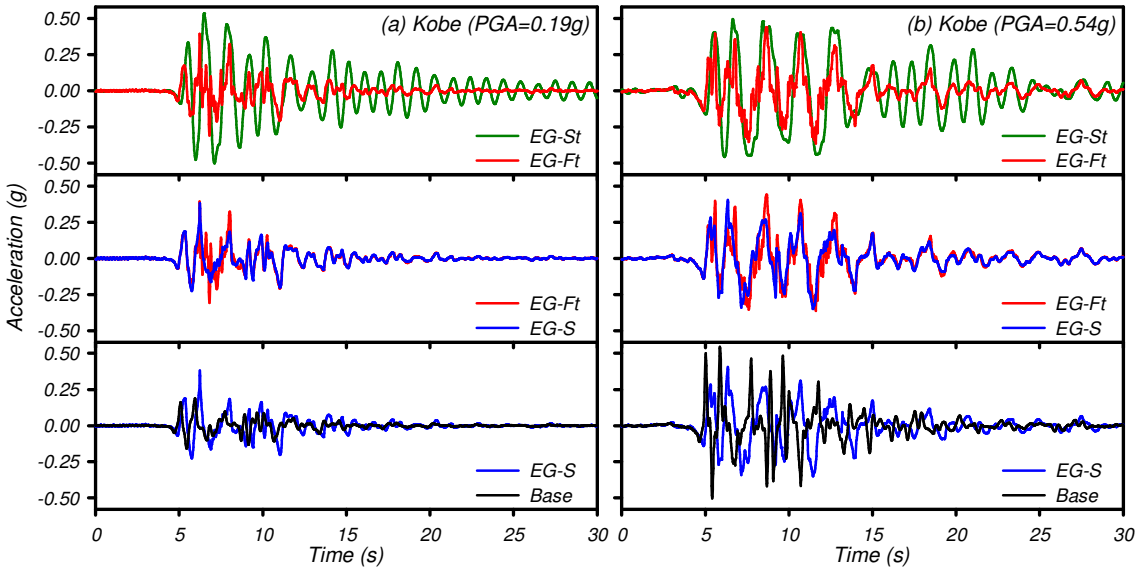

Figure 5.3. Recorded accelerations on the embedded grid and structure (EG with A_r = 24%) of MKH02 during (a) Kobe motion with PBA = 0.19g; (b) Kobe motion with PBA = 0.54g.

For the Kobe motion with PBA=0.54 g, as shown in Figure 5.3b, the soil surface (EG-S) had a PHA = 0.39 g (28% less than the PBA) and the superstructure (EG-St) had a PHA = 0.50g (7% less than the PBA). The surface acceleration has stronger long-period components than the base acceleration, which is attributed to softening of the soil and partial damage of the soil-cement grid, resulting in an effective lengthening of the reinforced soil system's effective natural period. The superstructure (EG-St) experienced four successive acceleration cycles with maximum values of 0.50 g followed by many smaller cycles. The recorded vertical displacements of the footing indicated large rotations during these four large amplitude cycles, indicative of foundation rocking. The effective natural period of the superstructure was about 1.85 s, more than twice the fixed-based natural period of the superstructure (0.8 s). The differences in the accelerations on the footing (EG-Ft) and soil surface (EG-S) are greatest when the superstructure accelerations are greatest, and become small once the superstructure accelerations dropped below about 0.25 g late in the shaking event. The footing accelerations have stronger high-frequency components than the superstructure acceleration, which may be attributed to the effect of foundation rocking and interaction between footing and soil as discussed later.

Behaviors similar to those described above were observed for the structures on the embedded and floating grids in model MKH04.

5.3.2 Dynamic Moment, Rotation, and Settlement Responses

The dynamic moment, rotation, and settlement of the footing for the structure located on the embedded grid (EG with $A_r = 24\%$) of MKH02 during Kobe motion with PBA = 0.19g are shown in Figure 5.4. Time histories are shown for vertical displacements at the north (EG-Ft-N) and south (EG-Ft-S) edges of the footing (Figure 5.4a), footing rotation (Figure 5.4b), and base acceleration (Figure 5.4c). The moment imposed on the footing by the structure's inertial loads (M_{ft}) and the average footing vertical displacement are plotted versus footing rotation (θ) in Figures 5.4d and 5.4e, respectively. The vertical displacement time histories at the footing edges were calculated by combining high-frequency accelerometer and low-frequency linear potentiometer sensor data, following the procedures described in Allmond and Kutter (2013). Footing rotations are computed from the difference in vertical displacements across the footing width (L). The applied footing moment was computed as:

$$M_{ft} = m_{ft}a_{ft}H_{ft} + m_{St}a_{St}H_{St} + m_{col}a_{col}H_{col} \quad (1)$$

where "*m*", "*a*" and "*H*" are mass, horizontal acceleration at the center of gravity, and height of the center of gravity from the base of the footing, respectively, and the subscripts "*ft*", "*st*", and "*col*" refer to the footing, superstructure and column of the SDOF structure, respectively (Figure 5.5). The total weight of the structure (V) is the sum of the weights for the footing (V_{ft}), column (V_{col}), and superstructure (V_{st}). The footing's moment-rotation response (Figure 5.4d) shows one large cycle of rotation in each direction which mobilized the footing's peak moment capacity ($M_{c,ft}$) of about $M_{c,ft}$ = 65 MNm. The moment reduced slightly with increasing rotation beyond those at which $M_{c,ft}$ was mobilized. The peak footing rotations were accompanied by an average vertical uplift of the footing (indicative of a rocking response), as shown in the plot of average vertical displacement versus footing rotation in Figure 5.4e. The cyclic loading did, however, result in accumulation of a permanent average footing settlement of 35 mm with negligible residual tilt (Figures 5.4b and 5.4e).

The dynamic response of the same structure (i.e., with EG with $A_r = 24\%$ in MKH02) during the strongest Kobe motion with PBA = 0.54g is shown in Figure 5.6. The footing's

moment capacity was again fully mobilized, and the peak rotations were almost three times greater than for PBA = 0.19 g (i.e., 0.020 rad in Figure 5.6 versus 0.007 rad in Figure 5.4). The average footing settlement progressively increased to its final value of about 230 mm (Figures 5.6a and 5.6e), which is almost seven times greater than for PBA = 0.19 g. The final footing settlement was accompanied by a permanent residual rotation of about 0.006 rad (Figure 5.6b). This large settlement and residual rotation during the strongest Kobe motion are attributed to crushing of the soil-cement grid underneath the footing, as discussed in a following section. The soil-cement grid did, however, continue to support the static loads of the structure despite the damage it incurred during this strong shaking event; note that the factor of safety against bearing failure would only be about 0.96 if the footing was resting on the soft clay alone.

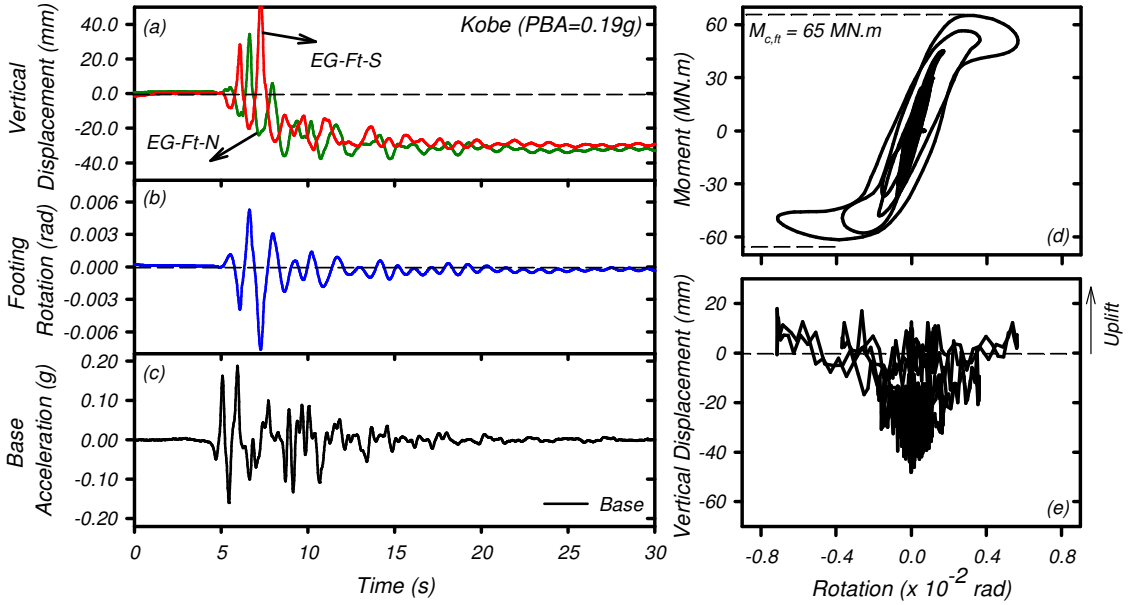

Figure 5.4. Dynamic response of the structure located on the embedded grid (EG with Ar = 24%) of MKH02 during Kobe motion with PBA = 0.19 g: (a) footing settlement time history; (b) footing rotation time history; (c) base acceleration time history; (d) footing moment versus rotation; and (e) footing vertical displacement versus rotation.

Moment-rotation and settlement-rotation plots for the footings on embedded and floating grids with A_r = 33% (MKH04) during the strongest Kobe motion with PBA = 0.54 g are shown in Figures 5.7a, and 5.7b, respectively. Both footings mobilized their peak moment capacities, which were about $M_{c,ft}$ = 97 MNm and 103 MNm on the embedded and floating grids, respectively. These $M_{c,ft}$ are about 50% greater than the $M_{c,ft}$ =65 MNm obtained for the footing on the embedded grid with A_r = 24% in MKH02 (Figure 5.6); the

greater $M_{c,ft}$ values in MKH04 are attributed primarily to the footing widths being greater than in MKH02 (14.8 m versus 11.4 m; Table 5.1). The final average settlements of the footings in MKH04 were only about 30-40 mm, and the strongest cycles of footing rotation were accompanied by an average footing uplift. The peak footing rotations were relatively small (about half those for MKH02) and the residual rotations were negligible.

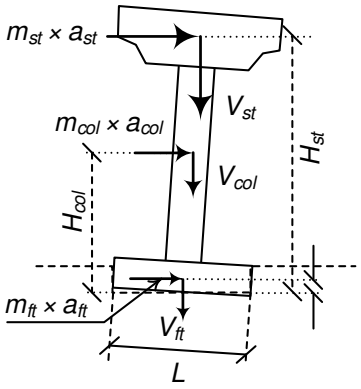

Figure 5.5. Definition of terms for computing structural inertial loads and footing moments

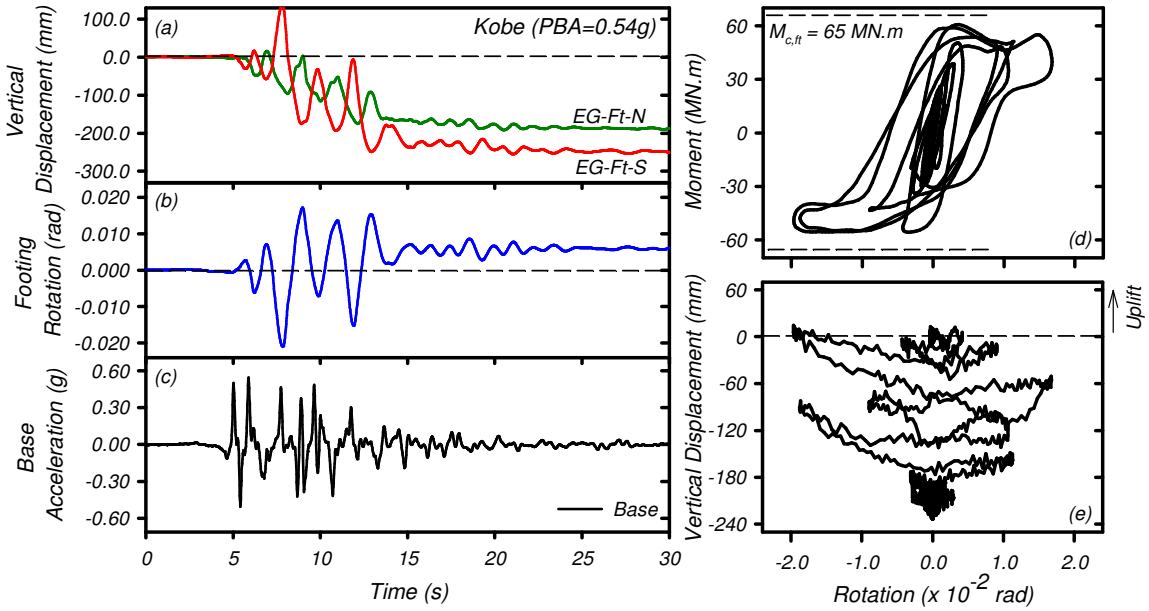

Figure 5.6. Dynamic response of the structure located on the embedded grid (EG with A_r = 24%) of MKH02 during Kobe motion with PBA = 0.54 g: (a) footing settlement time history; (b) footing rotation time history; (c) base acceleration time history; (d) footing moment versus rotation; and (e) footing vertical displacement versus rotation.

The dynamic rotations of the embedded and floating grids themselves were also examined to determine if they were significant contributors to the total footing rotations. The rotations of the embedded and floating grids were found to be similar to each other

and to be small enough, relative to the total footing rotations, that they can be neglected in evaluating the footing responses.

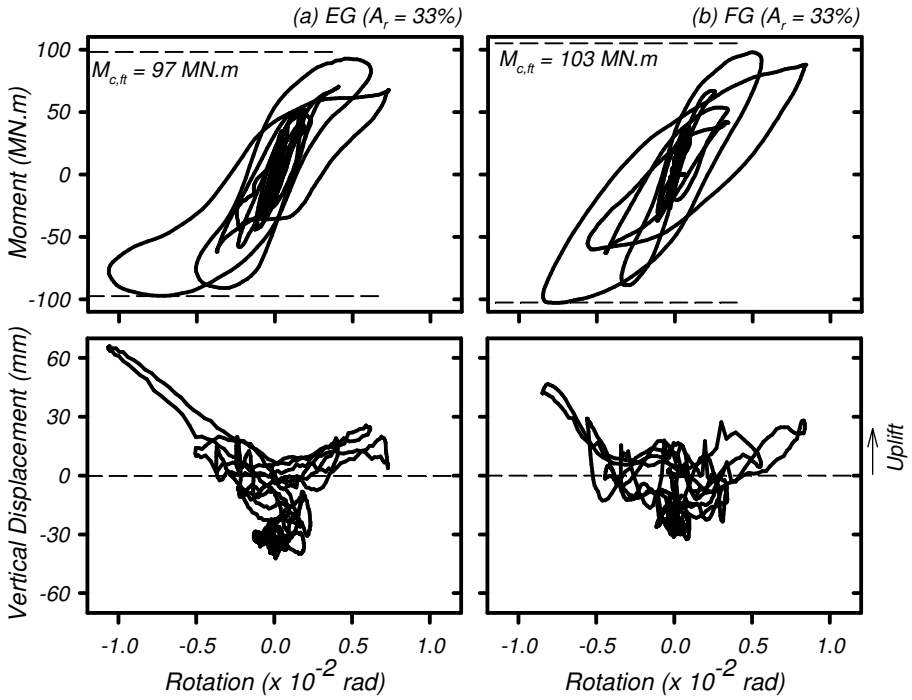

Figure 5.7. Dynamic response of the structure located on the grids of MKH04 during Kobe motion with PBA = 0.51g, (a) the embedded grid (EG with A_r = 33%); (b) the floating grid (FG with A_r = 33%).

5.3.3 Footing Settlements for All Shaking Events

Incremental settlements of all three footings for all shaking events are presented in Figure 5.8; the shaking-induced settlements are shown in Figure 5.8a, while the post-shaking consolidation settlements are shown in Figure 5.8b. For the footing on the embedded grid (EG-Ft) with A_r = 24% (MKH02), the shaking-induced and post-shaking settlements were both less than 10 mm for motions with PBA ≤ 0.10g, whereas the shaking-induced incremental settlements reached about 40 mm for a TCU motion with PBA = 0.327 g and a Kobe motion with PBA = 0.173 g, and the shaking-induced settlement jumped to 230 mm for the strongest Kobe motion with PBA = 0.526 g. The jump in settlement during the strongest Kobe motion is attributed to the onset of crushing of the soil-cement grid, as discussed later. The incremental settlements due to post-shaking consolidation remained relatively small for all events for this footing. For the footing on the embedded grid (EG-Ft) with A_r = 33% (MKH04), the shaking-induced and post-shaking consolidation settlements only reached about 40 mm and 20 mm, respectively, for the strongest Kobe

motion with PBA = 0.526 g. These relatively small settlements are attributed to a lack of damage to the soil-cement grids, as also discussed later. For the footing on the floating grid (FG-Ft) with A_r = 33% (MKH04), the shaking-induced settlements were almost equal to those for the footing on the embedded grid with A_r = 33%, but the post-shaking consolidation settlements jumped up to 120 mm for the strongest Kobe motion with PBA = 0.526 g. The large post-shaking consolidation settlements for this latter event are attributed to the reconsolidation strains that developed in the clay below the base of the floating grid.

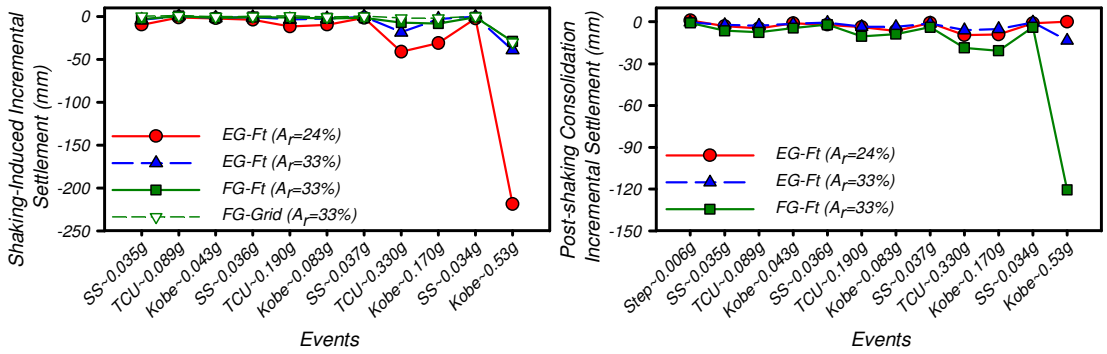

Figure 5.8. Shaking-induced and post-shaking consolidation settlements of the footings for all three structural models for each of the primary shaking events

5.3.4 Relating Peak Moments, Rotations, and Settlements from All Shaking Events

The peak footing moments (M_{ft}) and total incremental settlements (Δ_{ft}) are plotted versus peak footing rotation (θ_{pk}) in Figures 5.9a and 5.9b, respectively, for all three footings and all shaking events; the footing moments are normalized by VL/2 which is the maximum possible restoring moment (neglecting large deformation effects), and the footing settlements are normalized by the footing width. The three footings exhibited similar normalized peak moment versus peak rotation responses, including similar maximum normalized moments of $M_{ft}/(VL/2) \approx 0.90$. The normalized settlements for these footings remained less than about 0.1% for $\theta_{pk} \leq 0.004$ rad (Figure 5.9b) which corresponds to $M_{ft}/(VL/2) \leq 0.8$ or equivalently $M_{ft}/M_{c,ft} \leq 0.9$ (Figure 5.9a). The normalized settlement for the footing on the embedded grid with A_r = 24% (MKH02) jumped to 2% when the peak footing rotation reached almost 0.02 rad; this response was for the strongest Kobe event and is associated with crushing of the soil-cement grid near the footing base. The

normalized settlement for the footing on the floating grid with A_r =33% (MKH04) jumped to 1% when the peak footing rotation reach about 0.009 rad; this response was also for the strongest Kobe event and is associated with reconsolidation strains in the clay below the base of the floating grid.

5.3.5 Damage to Soil-Cement Walls

The soil surrounding the soil-cement grids was excavated after completion of all shaking events and the cracking patterns in the grids mapped to document shaking-induced damage. Photographs of the embedded grids with A_r = 24% (MKH02) and A_r = 33% (MKH04) are shown in Figures 5.10a and 5.10b, respectively. In MKH02, the soil-cement walls were extensively crushed beneath the structural footing (with crushing extending 0.3 to 0.5 m below the tops of the walls) and were significantly cracked to depths of up to 10 m (Figure 5.10a). The crack orientations and locations were highly varied. In MKH04, the soil-cement walls showed no visible signs of crushing beneath the footings or cracking at larger depths (Figure 5.10b).

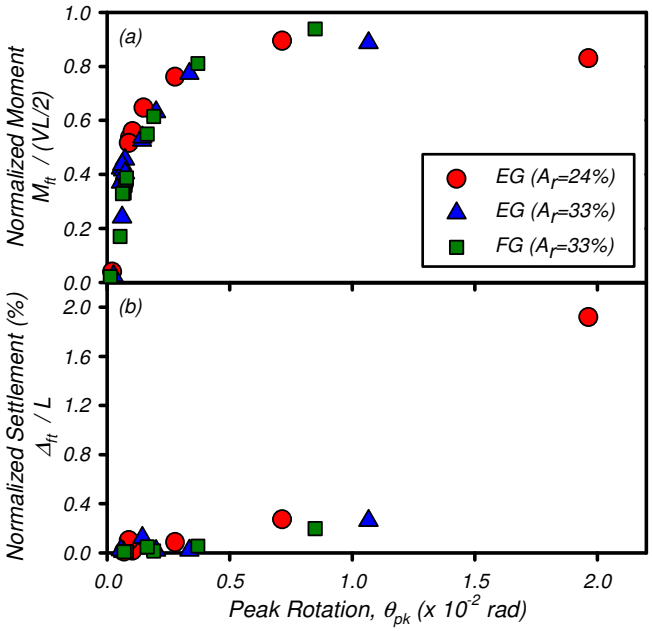

Figure 5.9. Peak moments, settlements, and rotations for all footings and motions: (a) normalized peak footing moment versus peak footing rotation; (b) normalized incremental settlement versus peak footing rotation.

5.4 Analysis of Demands on Soil-Cement Grids

The demands imposed on each soil-cement grid include contributions from: (1) static loads from the overlying structure, (2) inertial loads from the structure during shaking, and

(3) kinematic loads from the interaction of the soft clay profile and soil-cement grid during shaking. Methods for analyzing these loading cases were evaluated for their ability to distinguish between the occurrence and absence of crushing or cracking of the soil-cement grids, as identified in the previous sections.

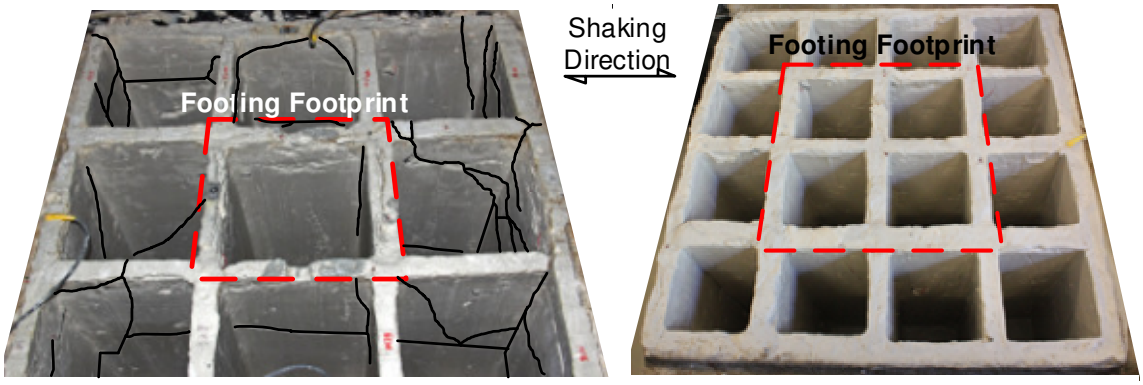

(a) EG with A_r = 24% (b) EG with A_r = 33%

Figure 5.10. Post-testing photographs of two soil-cement grids with any visible cracks highlighted for clarity: (a) embedded grid in MKH02, and (b) embedded grid in MKH04.

5.4.1 Static structural loads

Static loading of each soil-cement grid was evaluated for (1) the structural capacity of the soil-cement to carry the stresses imposed by the overlying footing, and (2) the geotechnical capacity of the soil-cement grid to carry the structural loads without plunging or experiencing excessive settlements. The structural capacities of the grids were estimated based on the unconfined compressive strength (UCS) of the soil-cement, and the loads from the footing were assumed to arch directly onto the grids (i.e., no load is carried by the soil within the grids). The axial geotechnical capacity of the soil-cement grid was estimated assuming that skin friction would be similar to that for drilled shafts (Bruce et al. 2013). The analysis results, summarized in Table 5.3, indicate factors of safety against a geotechnical failure of the soil-cement grids are high for the two embedded grids (FS = 9.5 and 16) and reasonable for the floating grid (FS = 3.8). The factors of safety against soil-cement crushing are 5.1 for the embedded and floating grids in MKH04 (both with A_r = 33%), but only 2.6 for the embedded grid in MKH02 with its lower A_r = 24% and lower unconfined compressive strengths (580 kPa versus 820 kPa).

5.4.2 Dynamic Structural Loads

The dynamic loads imposed on the soil-cement grids by the overlying structure require accounting for foundation rocking and how the footing contact stresses are transferred from the surface sand layer to the grid. A simplified procedure for estimating the load transfer from a rocking footing to the grid is investigated assuming that the footing contact stresses are controlled by the bearing capacity of the sand, after which their redistribution onto the grids needs to be evaluated. A simplified stress distribution for this mechanism is illustrated in Figure 5.11. The moment capacity of the footing can be estimated as (Deng et al., 2012):

Table 5.3. Analysis of foundation demands on the soil-cement grids

	EG in MKH02	EG in MKH04	FG in MKH04
Static loading			
FS against soil-cement crushing	2.6	5.1	5.1
FS against bearing failure of grid	9.5	16.0	3.8
Dynamic loading from footing			
L_{cs} (m)	1.1	0.97	0.97
q_{bLc} (kPa)	435	407	407
$M_{c,ft}$ (MNm)	69	100	100
C_r	0.55	0.83	0.83
$q_{u,cs}$ (kPa)	1060	1015	1015
q_{cg} (kPa)	568	477	477
$q_{u,sc}$ (kPa)	580	820	820
FS against soil-cement crushing	1.02	1.71	1.71

$$M_{c,ft} = V\frac{L}{2}\left(1 - \frac{A_c}{A}\right) \quad (2)$$

where A = area of the footing; and A_c = minimum bearing area required to support V when the limit bearing capacity of the foundation soil (q_{bLc}) is fully mobilized. The value of q_{bLc} under pure vertical loading is computed using a conventional bearing capacity formulae as:

$$q_{bLc} = S_q d_q q_o N_q + 0.5 S_\gamma d_\gamma \gamma L_{cs} N_\gamma \quad (3)$$

where q_o is the surcharge beside the footing, N_q and N_γ are bearing factors, s_q and s_γ are shape factors, d_q and d_γ are depth factors, and L_{cs} is the length of the contact area (L_{cs} = A_c/L for uni-directional rocking). The base shear coefficient (C_r) for a rocking footing, which is defined as the ratio of the lateral force to the weight of the superstructure required to mobilize the moment capacity of the footing, is then derived as:

$$C_r = \frac{L}{2H_{St}}\left(1 - \frac{A_c}{A}\right)\left(1 + \frac{m_{Ft}}{m_{St}}\right) \quad (4)$$

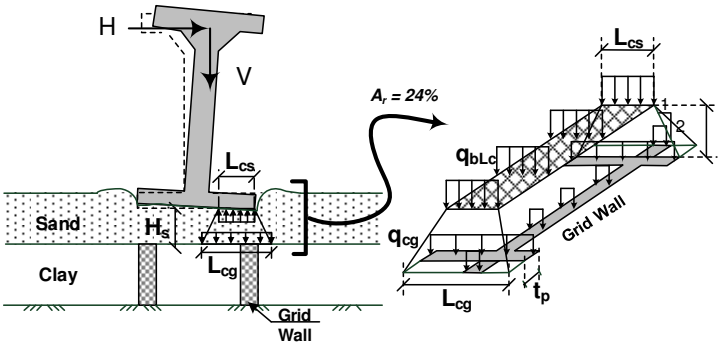

Figure 5.11. Schematic of rocking foundation mechanism1: rocking stresses controlled by sand layer

The mass of the column is redistributed equally to the superstructure and footing for use in this equation. The results of this analysis, as summarized in Table 5.3 and based on the properties in Table 5.1, indicate the L_{cs} are 1.10 and 0.97 m, the q_{bLc} are 1060 and 1015 kPa, the $M_{c,ft}$ are 69.0 and 100 MN.m, and the C_r are 0.55 and 0.83 for the grid with A_r = 24% (MKH02) and the grids with A_r = 33% (MKH04), respectively. The maximum observed footing rotation as a function of PHA for structures on embedded grids with A_r = 24%, and A_r = 33% for both MKH02 and MKH04 are displayed in Figure 5.12. For the footing on the embedded grid with A_r = 24% the total rotation of the footing rapidly increases at PHA reaches 0.52g, which indicates that the ultimate moment capacity of the footing was achieved. In the footing on the embedded grid with A_r = 33%, a gradual increase in rotation is observed as PHA approaches 0.8 g, indicating the ultimate moment capacity of the footing was not achieved and the applied pressure during footing rotation did not exceed the design limit of the soil-cement grid. Experimental results are in a good agreement with the analytical results.

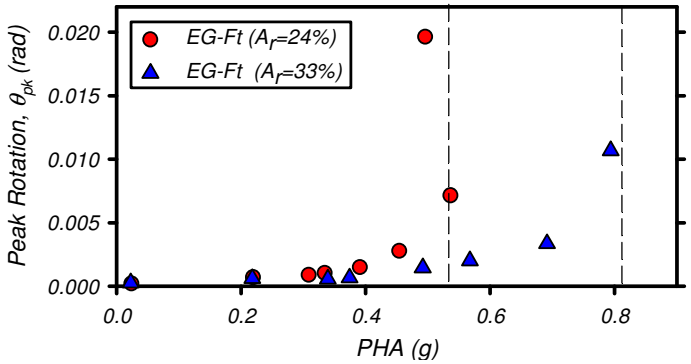

Figure 5.12. Experimental data for structures located on grids in test MKH02 and MKH04.

The stress transmitted by the rocking footing to the soil-cement grid was computed based on the assumption that the footing contact stress spreads at a 2(vertical):1(horizontal) slope down to the top of the grid, and that all stresses in the equivalent loaded area were carried by the grid alone (i.e., the soft clay did not carry any stress). The computed vertical stresses on the grids (q_{cg}) and the factors of safety against crushing of the soil-cement (FS = $q_{u,sc}/q_{cg}$) are summarized in Table 5.3. For the embedded grid with A_r = 24% (MKH02), the stress on the grid, q_{cg} = 568 kPa, is slightly less than the average strength of the soil-cement, $q_{u,sc}$ = 580 kPa, giving a factor of safety of 1.02 against soil-cement crushing. For the embedded and floating grids with A_r = 33% (MKH04), the stress on the grid is q_{cg} = 477 kPa which is less than the average strength of the soil-cement material, $q_{u,sc}$ = 820 kPa, giving a factor of safety of 1.72. Therefore, crushing of the soil-cement grids would not be expected for the embedded grid with A_r = 33%. The analysis results are consistent with the observed crushing of the embedded grid with A_r = 24% (Figure 5.10a) and the absence of crushing for the grids with A_r = 33% (e.g., Figure 5.10b). Moreover, the computed L_{cg} = 3.3 m for the soil cement grids with A_r = 24% (MKH02) is consistent with the observation that crushing occurred in both the transverse and longitudinal walls (Figure 5.10a). Thus, these analysis results suggest that the suggested mechanism is a good representation of the actual inertial loading conditions for this test.

5.4.3 Kinematic Loads from Soil Profile

The kinematic loads on the soil-cement grids due to their dynamic interaction with the soil profile was analyzed using a simplified procedure described in Khosravi et al. (2016). This analysis procedure: (1) estimates the shear stresses carried by the soil-cement grid based on the design relationships developed by Nguyen et al. (2013), and (2) estimates the tensile stresses that would develop under those imposed shear stresses, assuming the vertical and lateral total stresses remain equal to the overburden stress during shaking. The results for the embedded grid with A_r = 24% (MKH02) indicate that: (1) the soil-cement wall would have been in tension over its upper 10 m during the strongest TCU motion with PBA = 0.327 g and Kobe motion with PBA = 0.19 g, and would have been in tension over its full depth during the strongest Kobe motion with PBA = 0.526 g, and (2) the maximum tensile stress would have been about 86 kPa near the top of the walls during the strongest

TCU motion. The results for the grids with A_r = 33% (MKH04) indicate that: (1) the soil-cement wall would have been in tension over the full depth of the walls during the Kobe motion with PBA = 0.16 g, and the strongest Kobe motion with PBA = 0.506 g, and (2) the maximum tensile stress would have been about 83 kPa near the top of the walls during the strongest Kobe motion. The tensile strength of the soil-cement was estimated to be 10-15% of $q_{u,cs}$, or about 58-88 kPa for MKH02 and 82-123 kPa for MKH04. The analysis results for the embedded grid with A_r = 24% (MKH02) are reasonably consistent with the post-testing observation of cracks in the upper 5 to 10 m of the walls (Figure 5.10a). The analysis results for the grids with A_r = 33% (MKH04) are also reasonably consistent with the absence of cracking in the walls (Figure 5.10b), provided that the soil-cement's tensile strength was closer to the upper range of the estimated values. These analysis results suggest that the simplified procedure used by Khosravi et al. (2016) provides a reasonable first-order estimate of the potential for kinematic loading to produce tensile cracking in the soil-cement grids. It should be noted that the load distribution in the grid would also be affected by: (1) vertical stresses from the structure, (2) the boundaries of the grid, unreinforced soil and surrounding centrifuge container, and (3) the shear stresses from the structure, which were not considered in this analysis. It has also been assumed that the stresses in the grid due to inertial loads imposed by the structure are small relative to those due to kinematic loading, which is reasonable for the mid to lower portions of the grids in these tests.

5.5 Conclusion

Dynamic centrifuge model tests were performed to investigate the dynamic response of structures supported by shallow foundations on soft clay reinforced by embedded and floating soil-cement grids with area replacement ratios of 24 and 33%. Responses of three structures to a series of input motions were used to examine the moment-rotation-settlement responses of the footings and the performance of the soil-cement grids. The experimental data were archived for open distribution.

Footing settlements during shaking were controlled by the degree of footing rocking and the stresses imposed on the soil-cement grids. Shaking-induced footing settlements remained small (<15 mm) when the footing moment due to the inertial loads from the

superstructure were less than 90% of the estimated footing moment capacity ($M_{c,ft}$), peak footing rotations were less than 0.004 rad, and the stresses transmitted to the soil-cement were less than its unconfined compressive strength. The greatest footing settlement was 230 mm for the footing on an embedded grid with A_r = 24% (MKH02) during the strongest Kobe motion with a PBA = 0.53g, which fully mobilized the footing's moment capacity, produced peak footing rotations of 0.02 rad, and caused local crushing of the soil-cement under the footing. The footing settlements were only 30-40 mm for the footings on the embedded and floating grids with A_r = 33% (MKH04) during the same strongest Kobe motion, which also fully mobilized the footing moment capacities but did not cause any visible damage to the soil-cement under the footings. Additional post-shaking footing settlements attributed to dissipation of shaking-induced excess pore water pressures in the soft clay were small (<15 mm) for the embedded grids with A_r = 24% or 33% in all events, but did reach 120 mm for the floating grid during the strongest Kobe motion.

Simplified analysis methods for estimating the inertial and kinematic loads imposed on the soil-cement grids provided results which were reasonably consistent with the observed damage patterns; i.e., the loading conditions which produced crushing near the tops of the walls and cracking at larger depths. The inertial loads imposed by the structures were evaluated by assuming that the footing contact stresses are controlled by the bearing capacity of the sand, after which the stress was redistributed at a 2:1 slope to the top of the grids. This mechanism produced results which reasonably distinguished between conditions which did and did not produce crushing near the tops of the walls. The simplified analyses for the rocking response of the structures also provided accurate estimates of the footing moment capacities and the base shear coefficients at the onset of rocking. The simplified analysis for kinematic loading of the soil-cement grid, which was based on the procedure described in Khosravi et al. (2016), provided results which reasonably distinguished between the conditions which did and did not produce cracking in the soil-cement walls at larger depths.

The results of these centrifuge tests demonstrate the potential effectiveness of soil-cement grids for supporting structures on shallow foundations at soft soil sites, and provide

a basis for validating future advances in equivalent-static or nonlinear dynamic analysis methods for these types of ground reinforcement systems.

6 Numerical Simulations of Dynamic Centrifuge Tests of Structures with Shallow Foundations on Soft Clay Reinforced by Soil-Cement Grids[4]

This chapter is produced from a journal paper, Khosravi et al. 2016, which has been prepared to submit in Journal of Geotechnical and Geoenvironmental Engineering.

Khosravi, M., Boulanger, R. W., Wilson, D. W., Olgun, C. G., (2016). "Numerical Simulations of Dynamic Centrifuge Tests of Structures with Shallow Foundations on Soft Clay Reinforced by Soil-Cement Grids" Journal of Geotechnical and Geoenvironmental Engineering (Ready to sbumit).

Abstract. This study uses three-dimensional (3D), nonlinear finite-difference analyses to investigate the seismic response of structures on shallow foundations over soft soils reinforced with soil-cement grid. The goal is to evaluate the stresses transferred to the soil-cement grid during foundation rocking and the potential for large foundation settlements associated with local crushing of the soil-cement. The numerical analyses are first validated using data from dynamic centrifuge experiments that included cases with and without large foundation settlements and localized crushing of the soil-cement grids. The experimental and numerical results indicated that the dynamic loads imposed on the soil-cement reinforced soil by the overlying structure require accounting for foundation rocking and how the footing contact stresses are transferred to the soil-cement ground reinforcement. The numerical analyses provided reasonable prediction of structural rocking response and the zone of expected crushing or lack of crushing, but under-estimated the accumulation of foundation settlements when seismic demands repeatedly exceeded the soil-cement strength. Moment-rotation response of structures and uplift behavior of the footing under monotonic lateral loading were shown to be reasonably consistent with the results of dynamic centrifuge tests. Parametric analyses using the validated numerical model then illustrated the importance of area replacement ratio, thickness of the top sand layer, properties of bearing sand layer, and stiffness ratio of the soil-cement grid to surrounding

[4] Mohammad Khosravi performed all the experiments and analyses.

soil. A simple design model for estimating the stresses imposed on the soil-cement grid by the rocking foundations was developed and shown to provide a reasonable basis for assessing if local damage to the soil-cement grid is expected.

6.1 Introduction

Earthquake-induced ground displacements and foundation settlements continue to be a major cause of damage to all types of structures including building, dikes, levees, and seawalls. Soil-cement ground reinforcement is an in-situ soil stabilization technique that has been used for mitigation of earthquake-induced ground displacements and foundation settlements (e.g., Kitazume and Terashi 2014, Bruce et al. 2013, Tokunaga et al. 2015).

Previous studies using case histories from past earthquakes (e.g. Tokimatsu et al. 1996, Yamashita et al. 2012, Tokunaga et al. 2015), dynamic centrifuge model tests (e.g. Adalier et al., 1998, Kitazume and Maruyama, 2006, Ishikawa and Asaka, 2006, Rayamajhi et al., 2014, Takahashi et al., 2006), and numerical analyses (e.g. Namikawa et al. 2007, Bradley et al. 2013, Nguyen et al. 2013, Puebla et al. 2006, Karimi and Dashti, 2016a,b) have shown the effectiveness of soil-cement ground reinforcement mitigation of earthquake-induced ground displacements. Most of these studies have evaluated overall deformation mechanisms and critical aspects of the seismic response of improved soil deposits subject to severe ground shaking. Few studies, however, investigated the response of structures over soil-cement ground reinforced soil (Khosravi et al. 2016) and its effect on the performance of underlying soil-cement ground reinforcement.

Centrifuge experiments performed by Khosravi et al. (2015a, b, c, d) investigated the seismic response of single-degree-of-freedom (SDOF) structures with shallow foundations over soft soil reinforced with soil-cement grids. The onset of large foundation settlements during strong shaking coincided with rocking of the shallow foundations and localized cracking and crushing of the soil-cement under the footing edges. The rocking response and settlement of the structures was shown to depend on the area replacement ratio (A_r = area of soil-cement divided by total area), soil-cement strength, and intensity of the shaking motion. Results of this study indicated that the dynamic loads imposed on the soil-cement reinforced soil by the overlying structure require accounting for foundation rocking and how the footing contact stresses are transferred to the soil-cement ground reinforcement.

Rocking of foundation systems on soil-cement ground reinforced soil may result in crushing of the soil-cement grid, and consequently, significant accumulation of settlement or residual rotations.

This chapter describes three-dimensional, nonlinear finite difference, equivalent-static pushover analyses of a series of dynamic centrifuge tests investigating the response of structures supported on shallow foundations on a soft soil foundation layer treated with soil-cement grids. The centrifuge model tests included a 23-m-thick clay profile reinforced with soil-cement grid with two different configurations: an "embedded" soil-cement grid that penetrated the underlying dense sand layer and had an area replacement ratio $A_r = 24\%$, and an "embedded" grid with $A_r = 33\%$. A bearing layer of coarse sand was considered over the grid-reinforced clay profile as load transfer platform. Structures on square shallow foundations were over the central part of each soil-cement grid system. The results of the equivalent static pushover analyses were validated using the rocking responses of the structures and performance of the soil-cement grid during dynamic centrifuge tests. The calibrated 3D pushover model was used to perform a parametric evaluation of relevant terms to (1) evaluate and validate model ability to estimate stress distribution and damage in the soil-cement grid due to stresses imposed due to rocking foundation; and (2) evaluate the parameters that control stress distribution from the top sand layer to the grid and its surrounding soil beyond those covered in centrifuge tests. Specifically, this includes an investigation of the effects of area replacement ratio, thickness of the bearing sand layer between the footing and reinforced soil, and soil and soil-cement grid properties. The results were used to develop a simple analysis method for estimating stress transfer for rocking foundation from the sand layer to the top of soil-cement grid. This simplified analysis method, combined with knowledge of the soil-cement strength, provides a basis for evaluating potential damage to the soil-cement grid.

6.2 Overview of Centrifuge Experiments

Two centrifuge tests were performed using the 9-m radius centrifuge at the University of California at Davis and the data archived for general distribution (Khosravi et al. 2015c, e). The tests consisted of two models, MKH02 and MKH04, as shown in Figure 6.1. The centrifuge models examined a 23.4-m thick (prototype), lightly over-consolidated layer of

kaolinite (Hydrite Flat DS) with three different soil-cement grid configurations: an "embedded" soil-cement grid which penetrated the underlying dense sand layer and had an area replacement ratio of A_r = 24%, an "embedded" grid with A_r = 33%, and a "floating" grid in the upper half of the clay layer with A_r = 33%. A 2.3-m-thick (prototype) bearing layer of coarse Monterey sand was placed over the grid-reinforced clay profile. Properties of the kaolinite include: Liquid Limit, *LL*=47; Plastic Index, *PI*=19; specific gravity of solids, G_s=2.58; median particle size of 4.0 μm; and a coefficient of consolidation, C_v=0.7 mm^2/s in virgin loading and 2.3 mm^2/s in unloading/reloading (Khosravi et al. 2015a). Average unconfined compressive strengths for the soil-cement grid ($q_{u,sc}$) after 14 days of curing time were 580 and 820 kPa for MKH02 and MKH04, respectively.

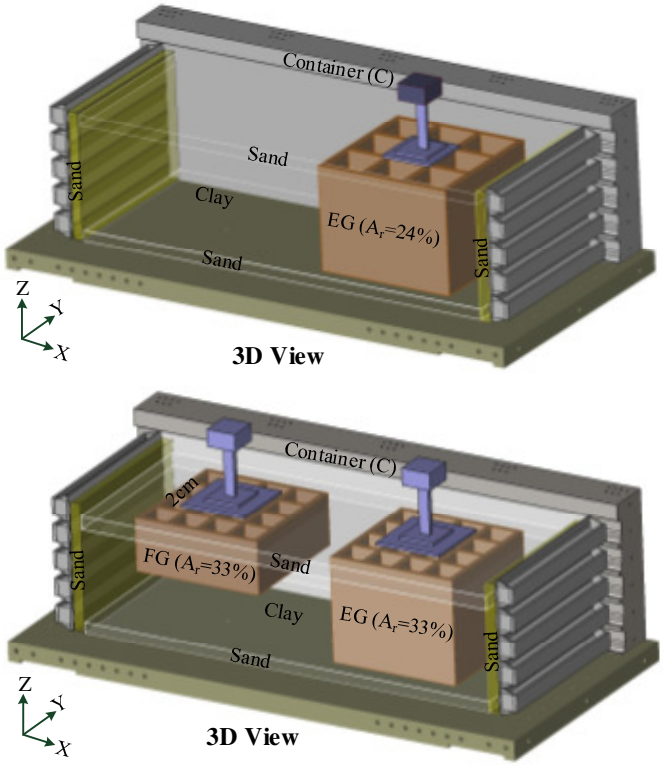

Figure 6.2. Model configurations with dimensions in prototype scale: (a) MKH02, (b) MKH04.

Structures supported by square shallow foundations were placed over the central part of each soil-cement grid system in both MKH02 and MKH04 (Figs 1a and 1b). The SDOF structures were comprised of aluminum square footings, aluminum rectangular hollow columns, and aluminum and steel block superstructures. The footing width and weight, superstructure weight, and height of the superstructure's center of mass from the footing

base for all structures are summarized in Table 6.1. The models were subjected to 13 shaking events with peak base accelerations (PBAs) ranging from 0.006 to 0.546 g.

Table 6.1. Parameters of the soil, soil-cement grid and structure

	EG in MKH02	EG in MKH04
Area replacement ratio, A_r (%)	24	33
Panel spacing, S (m)	6.9	9.8
Panel thickness, t_p (m)	1.2	1.2
Reinforced depth ratio	1.0	1.0
UCS of soil-cement, $q_{u,cs}$ (kPa)	580	819
Footing width, L (m)	11.4	14.8
Superstructure weight, V_{st} (kN)	8658	8658
Footing weight, V_{ft} (kN)	3835	5866
Column weight, V_{col} (kN)	307	307
Height of V_{st} from footing base, H_{st} (m)	13.96	13.96
Height of V_{ft} from footing base, H_{ft} (m)	0.59	0.53
Height of V_{col} from footing base, H_{col} (m)	6.59	6.59

6.2.1 Dynamic Moment, Rotation, and Settlement Responses

Normalized moment-rotation and settlement-rotation plots for the footings on embedded grids with A_r = 24% (MKH02) and A_r = 33% (MKH04) during the strongest Kobe motion with PBA = 0.54 g are shown in Figures 5.2a, and 5.2b, respectively. The footing moments are normalized by VL/2 which is the maximum possible restoring moment (neglecting large deformation effects). The footing's moment-rotation response of footing on EG with A_r = 33% showed one large cycle of rotation in each direction which mobilized the footing's peak moment capacity ($M_{c,ft}$) of about $M_{c,ft}$ = 95 MNm. The moment reduced slightly with increasing rotation beyond those at which $M_{c,ft}$ was mobilized. The peak footing rotations were accompanied by an average vertical uplift of the footing (indicative of a rocking response), as shown in the plot of average vertical displacement versus footing rotation in Figure 6.2b. The cyclic loading, however, resulted in accumulation of a permanent average footing settlement of 35 mm with negligible residual tilt.

The dynamic response of the structure on EG with A_r = 24% in MKH02 during the strongest Kobe motion with PBA = 0.54g is also shown in Figure 6.2a. The footing's moment capacity was again fully mobilized, and the peak rotations were almost two times

greater than in MKH04 (i.e., 0.020 rad in Figure 6.2a versus 0.01 rad in Figure 6.2b). The superstructure experienced four successive acceleration cycles with maximum values of 0.50 g followed by many smaller cycles. The average footing settlement progressively increased to its final value of about 230 mm (Figure 6.2a), which is almost seven times greater than in MKH04. This large settlement and residual rotation during the strongest Kobe motion are attributed to crushing of the soil-cement grid underneath the footing.

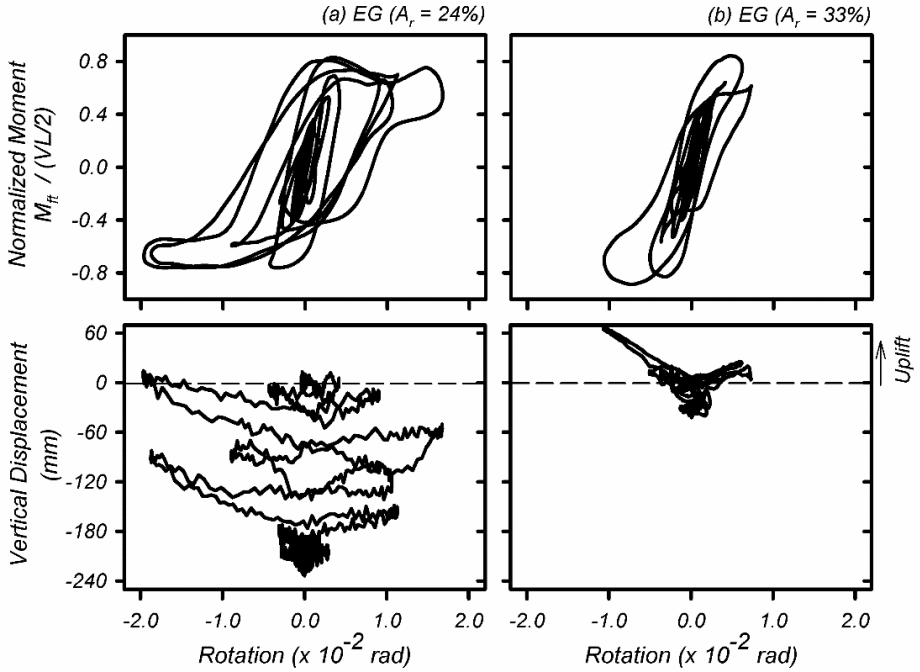

Figure 6.2. Dynamic response of the structure located on the embedded grids during Kobe motion with PBA = 0.51g, (a) the embedded grid (EG) with A_r = 24%, and (b) the embedded grid (EG) with A_r = 33%.

The soil surrounding the soil-cement grids was excavated after completion of all shaking events and the cracking patterns in the grids mapped to document shaking-induced damage. Photographs of the embedded grids with A_r = 24% (MKH02) and A_r = 33% (MKH04) are shown in Figures 6.3b and 6.3c, respectively. In MKH02, the soil-cement walls were extensively crushed beneath the structural footing (with crushing extending 0.3 to 0.5 m below the tops of the walls) and were significantly cracked to depths of up to 10 m (Figure 6.3b). The crack orientations and locations were highly varied. In MKH04, the soil-cement walls showed no visible signs of crushing beneath the footings or cracking at larger depths (Figure 6.3c).

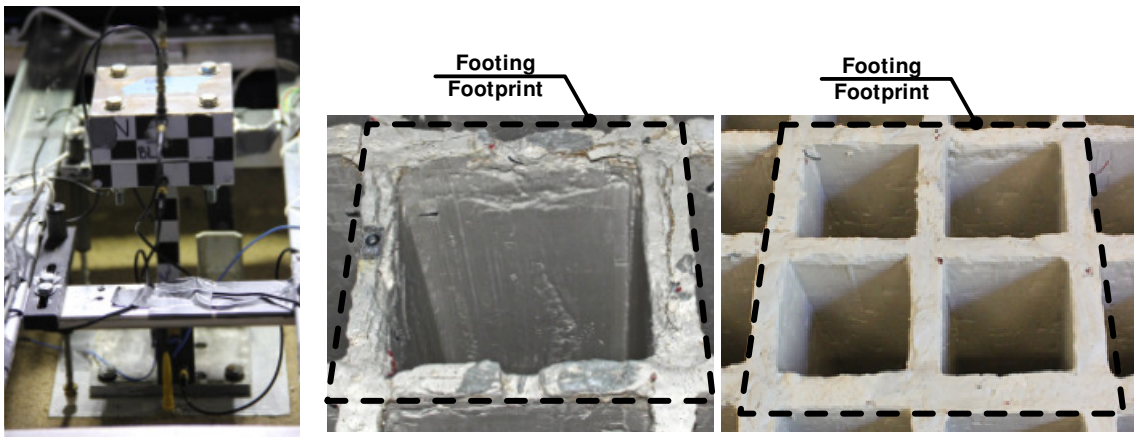

Figure 6.3. Photographs of a SDOF model before shaking and soil-cement grids during post-test excavations: (a) SDOF system, (b) embedded grid in MKH02, and (c) embedded grid in MKH04.

6.3 Overview of Numerical Simulations

Three-dimensional nonlinear analyses of the centrifuge tests were performed in the finite difference FLAC3D platform (Itasca 2012) to evaluate and validate model ability to estimate stress distribution and damage in the soil-cement grid due to stresses imposed due to rocking foundation. The soil and soil-cement grid were modeled with brick zones available in FLAC3D. The Mohr–Coulomb model was used to simulate the nonlinear response of the soil and soil-cement material without any pore fluid within the model. The Mohr–Coulomb material model requires conventional soil parameters including: unit weight (γ), friction angle (ϕ), cohesion intercept (c), shear modulus (G), and bulk modulus (B). The Mohr–Coulomb idealization simplifies the problem, but nonetheless allows initial insights to be gained from parametric analyses across a range of parameters.

The analyses presented herein used common baseline models shown in Figure 6.4 from which various terms and parameters (e.g. thickness of the bearing sand layer, soil properties, footing dimensions) were varied. The baseline models are those for the MKH02 and MKH04 centrifuge tests. The baseline soil model consisted of a 23-m-thick layer of lightly over-consolidated clay, underlain and overlain by a 2.2-m thick layer of dense sand. The 1.3-m wide soil-cement walls were spaced 9.8 m and 7.0 m center-to-center apart, for an average A_r = 24% and A_r = 33%, respectively (Figures 6.4a and 6.4b). The mesh size and the maximum unbalanced force at the grid points (i.e., error tolerance) were selected based on a series of parametric analyses to optimize accuracy and computation speed. Finer

elements were used near the soil surface and building foundation to better capture the larger deformation gradients.

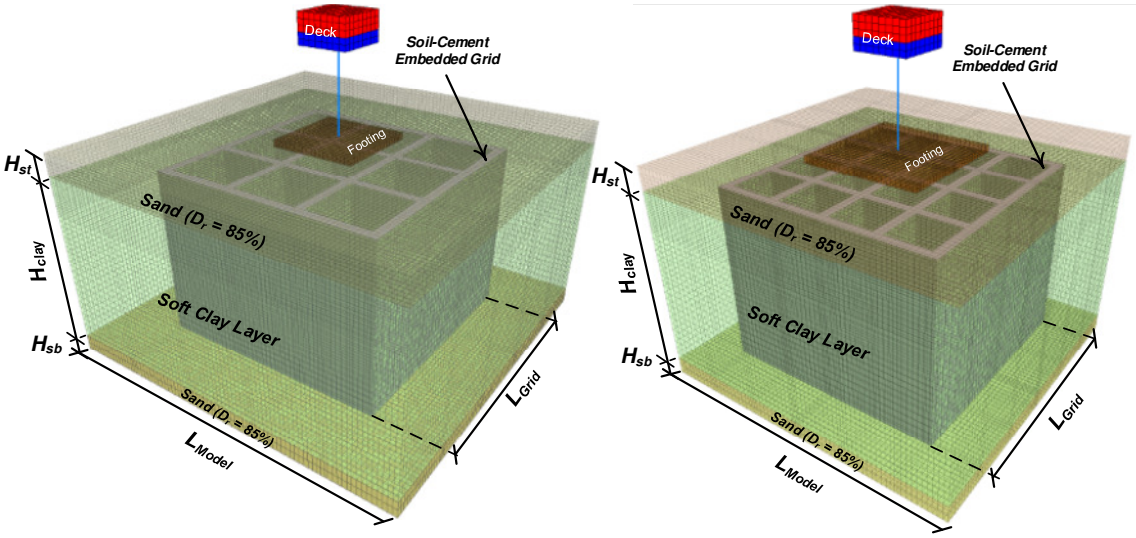

Figure 6.4. Numerical model configurations with dimensions: (a) the embedded grid (EG) with A_r = 24%; and (b) the embedded grid (EG) with A_r = 33%.

The finite difference discretization of the structure system simulated in prototype scale is shown in Figure 6.5. The structure and its foundation were modeled using quadratic solid and structural elements with linear-elastic material properties. The column of the structure is modeled with beam element with properties summarized in Figure 6.5. The interfaces between the foundation and soil were modeled as linear spring–slider systems, with interface shear strength defined by the Mohr–Coulomb failure criterion.

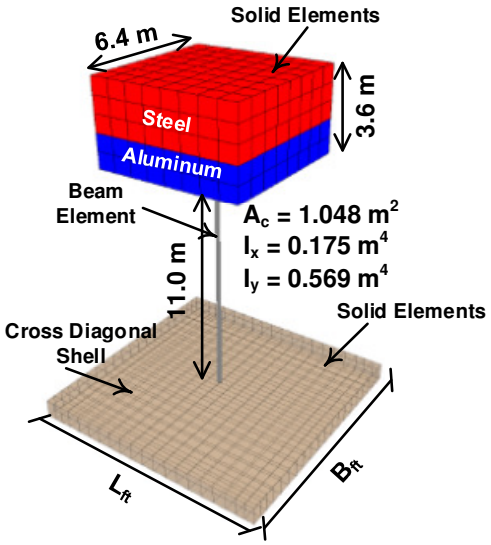

Figure 6.5. Structural model configuration with dimensions

Equivalent-static pushover analyses were used to evaluate the effects of structural inertial loading as is common in engineering practice; note that this case neglects kinematic loading effects between the footing, soil, and soil-cement grid. The base of the finite difference mesh was fixed and the lateral boundaries were fixed horizontally and free vertically for this loading case. Future analyses may be used to explore a set of quasi-static cyclic pushover analyses to evaluate the ability of the model to simulate foundation settlement during cyclic loading of the structure. In addition, a future set of equivalent-static analyses for the foundation system could be used to evaluate the distribution of seismic loads between the soil-cement grid and enclosed soil; this case would evaluate the kinematic loading effects in the foundation alone. The lateral boundaries of the finite difference mesh would need to be tied to their opposing sides (same vertical and horizontal displacement) for this analysis case.

6.4 Numerical Results for Models MKH02 and MKH04

The response of different soil-foundation-structure systems were numerically simulated in FLAC3D and compared with centrifuge measurements in terms of moment capacity, footing rotation, and performance of the soil-cement grid underneath the footing.

6.4.1 Responses of the Structures and Soil-Cement Grids

For the static pushover analysis, a horizontal velocity is applied on the center of mass of the superstructure. In Figure 6.6, plots of moment, maximum shear stresses, τ_{max}, in the critical juncture on soil-cement grid under the footing, and vertical displacement for the footings on embedded grids with A_r = 24% (MKH02) and A_r = 33% (MKH04) during monotonic lateral loading to a superstructure displacement of 420 mm are shown. The "critical juncture" is the juncture, or corner crossing of longitudinal and transverse walls, that is most strongly loaded and it was always the juncture beneath the other ends of the rocking footing contact area. The experimental peak footing moments (M_{ft}) are also plotted versus peak footing rotation (θ_{ft}) in Figures 6.6a for both footings and all shaking events. The two footings exhibited similar normalized peak moment versus peak rotation responses, including similar maximum normalized moments of $M_{ft}/(VL/2) \approx 0.90$ mobilized at about the same footing rotation of $\theta_{ft} \approx 0.006$ rad. The numerical results are

consistent with the results of centrifuge tests, as presented in Figure 6.6a. The two systems produced different maximum shear stresses in the soil-cement for similar levels of footing rotation, though. The maximum shear stress, τ_{max}, is shown for the most strongly, and lightly loaded elements in the critical juncture of the soil-cement grid; these maximum and minimum values of τ_{max} are normalized by half of the unconfined compressive strength, $q_{u,sc}/2$, of the soil-cement material as shown in Figure 6.6b. The smallest value of $\tau_{max}/(q_{u,sc}/2)$ was on the inner side of the critical juncture while the greatest value was under the leading edge of the footing during foundation rocking. For the embedded grid with $A_r = 24\%$, both the largest and smallest $\tau_{max}/(q_{u,sc}/2)$ reached their peak values of 1.0 and 0.6 at $\theta_{ft} \approx 0.006$ rad (Figure 6.6b) which corresponds to $M_{ft}/(VL/2) \approx 0.9$. In the embedded grid with $A_r = 33\%$ (MKH04), the smallest $\tau_{max}/(q_{u,sc}/2)$ on the soil-cement grid reached its peak of 0.4 at $\theta_{ft} \approx 0.006$ rad which corresponds to $M_{ft}/(VL/2) \approx 0.9$. The greatest $\tau_{max}/(q_{u,sc}/2)$ on the critical juncture, however, continued to rise even after the footing reached its moment capacity. Normalized maximum shear stress did not reach 1.0 after a rotation of $\theta_{ft} \approx 0.012$ rad (Figure 6.6b). This could be attributed to the continued increase in vertical stress on the critical juncture as the footing rotation continued to increase. The footings for both systems developed up-lift with a higher rate of vertical displacement for the footing on embedded grid with $A_r = 33\%$; stronger uplift in MKH04 is attributed primarily to the footing width being greater and FS_v being greater than in MKH02 (14.8 m versus 11.4 m). Normalized vertical displacement of the footings, however, is similar for both footings (Figure 6.6c).

The results from numerical simulations during monotonic lateral loading are further compared with dynamic centrifuge test results for select shaking events in Figure 6.7. Normalized moment-rotation and settlement-rotation plots for the footings on embedded grids with $A_r = 24\%$ (MKH02) during the Kobe motion with PBA = 0.19 g and embedded grid with $A_r = 33\%$ (MKH04) during the strongest Kobe motion with PBA = 0.54 g are shown in Figures 6.7a, and 6.7b, respectively. The results from numerical simulations were also plotted with dashed lines. Based on experimental results, both footings mobilized their peak moment capacities and no crushing of the soil-cement grids were observed during these motions. For this range of motions, the envelopes of the dynamic centrifuge tests

were well captured by the monotonic pushover curves. The experimental peak footing rotations were accompanied by an average vertical uplift of the footing (indicative of a rocking response), as shown in the plot of average vertical displacement versus footing rotation. The numerical simulations reasonably envelope the dynamic loading responses, although they do not simulate the accumulation of permanent average footing settlements of about 40 mm.

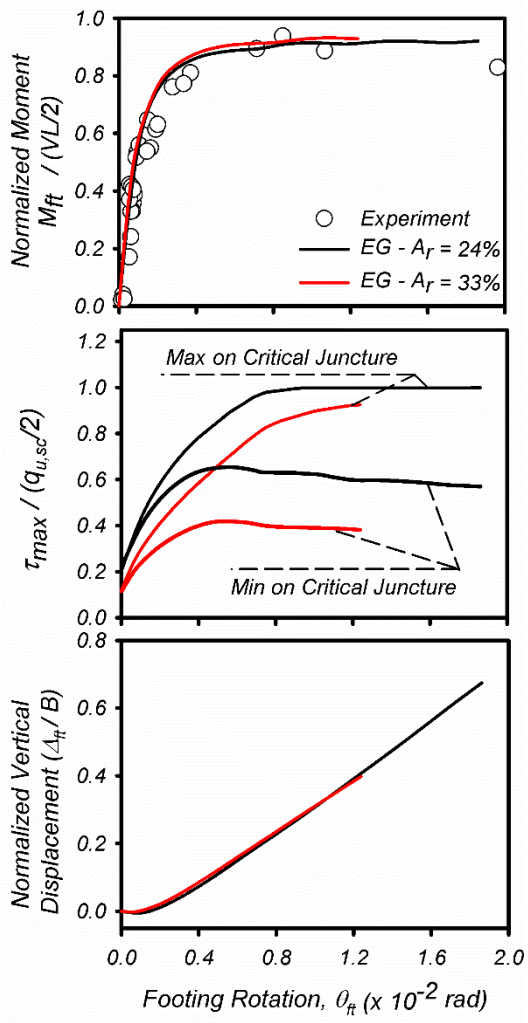

Figure 6.6. Normalized moment, maximum shear stress in the soil-cement, and normalized vertical displacement versus footing rotation for both embedded grids in MKH02 (A_r = 24%) and MKH04 (A_r = 33%): (a) normalized footing moment, (b) normalized maximum shear stress in the soil-cement at the top of the grid, and (c) normalized vertical displacement.

The dynamic response of the structure on EG with A_r = 24% in MKH02 during the strongest Kobe motion with PBA = 0.54g is compared with the results of monotonic pushover analysis using FLAC3D in Figure 6.7c. The monotonic pushover curve begins to over-estimate the moment-rotation resistance at large rotations and cannot approximate the

cyclic accumulation of foundation settlements. The observed behavior is attributed to crushing of the soil-cement grid underneath the footing that results in a settlement of 230 mm, and these features of behavior are not simulated in a pushover analysis. The centrifuge results indicated that the strength of the soil-cement grid, number of rotation cycles and rotation amplitudes control the settlement behavior of the structure over the soil-cement grid.

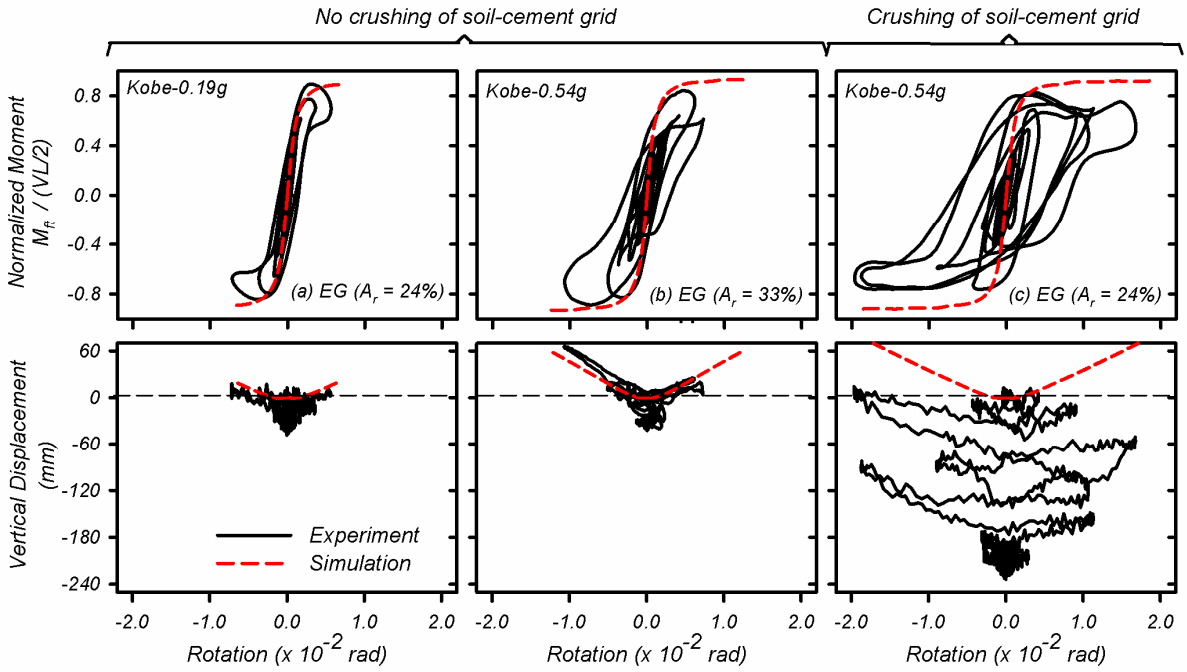

Figure 6.7. Measured dynamic and computed pushover responses of the structure located on the embedded grids during Kobe motions, (a) the embedded grid with A_r = 24% during Kobe motion with PBA = 0.19g; (b) the embedded grid with A_r = 33% during Kobe motion with PBA = 0.54g; and (c) the embedded grid with A_r = 24% during Kobe motion with PBA = 0.54g.

6.4.2 Vertical Stress Distribution under the Footing

The dynamic loads imposed on the soil-cement grids by the overlying structure depend on: (1) the mechanism of load transfer from the footing through the sand to the elevation of the grid surface, (2) the distribution or sharing of stresses between the soil-cement grid and its surrounding soil, and (3) the distribution of stresses within the soil-cement grid.

The results from 3D numerical simulations are used to evaluate the parameters that control stress distribution under the footing at the end of consolidation (static loading only) and during shaking-induced foundation rocking. In Figures 6.8a and 6.8b, three dimensional (3D) contours of change in vertical stress, $\Delta\sigma_v$, imposed on the sand at the

elevation of the footing base and at the elevation of the soil-cement grid surface at the end of consolidation for the embedded grid with A_r = 24% are presented. The results are for the baseline model with H_s = 2.2 m, ϕ_s = 40 deg, and $q_{u,sc}$ = 600 kPa. Assuming uniform stress distribution of the structural load, the stress imposed on the soil beneath the footing should be 100.5 kPa (Figure 6.8a). Instead, the soil under the footing deflects in a bowl-shaped depression, relieving stresses under the middle of the footing. The change in vertical stress due to the footing increases from 32 kPa beneath the footing center to a maximum of 184 kPa beneath the corners of the footing. In Figure 6.8b, the change in vertical stresses imposed on the top of the soil-cement grid and enclosed soil (i.e., at a depth of 2.2 m below the footing base) due to the structural load are presented. Assuming a uniform stress distribution at this depth, with 2V:1H load spreading from the footing base, the expected uniform stress would be 71 kPa. Instead, the change in vertical stress is only 32 kPa on the soil at the middle of the grid cell and reaches a maximum of 117 kPa at the critical juncture on the soil-cement grid.

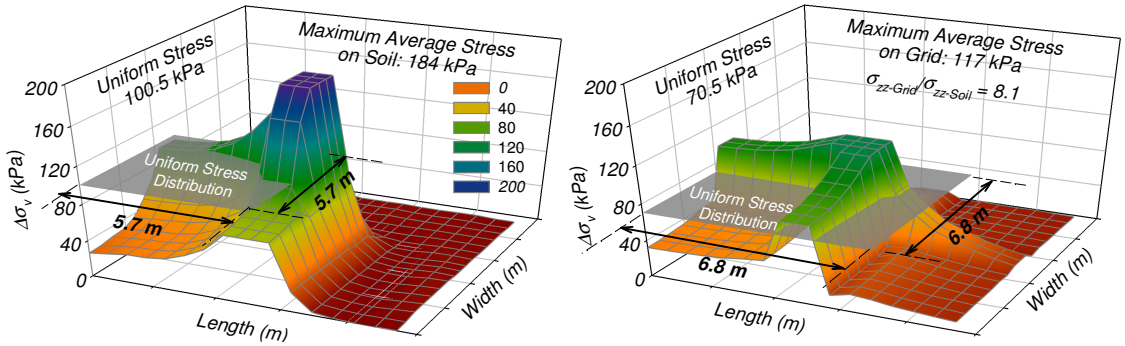

Figure 6.8. Computed change in vertical stress due to the static structural load for the embedded grid with A_r = 24%: (a) change in vertical stress $\Delta\sigma_v$ at the base of the footing; and (b) change in vertical stress $\Delta\sigma_v$ on the surface of soil-cement grid (2.2 m below the footing base).

The contours of change in vertical stress, $\Delta\sigma_v$, imposed at the footing base (0.9 m below the sand layer surface) and on the top of the soil-cement grid (2.2 m below the footing base) during foundation rocking at a peak footing rotation of $\theta_{ft} \approx 0.006$ rad (associated with $M_{ft}/(VL/2) \approx 0.90$) are presented in Figures 6.9a and 6.9b, respectively. As the foundation rocks, the contact area between the footing and soil reduces, and stress on the contact area increases. The vertical stress distribution beneath the footing is non-uniform with a maximum average $\Delta\sigma_v$ of 1050 kPa at the corners of the footing versus only 447 kPa at the middle of the footing edge. The maximum $\Delta\sigma_v$ imposed on the soil-cement grid

is 467 kPa at the critical juncture of the soil-cement grid (where concentration of $\Delta\sigma_v$ is observed) versus only 302 kPa at the middle of the transverse walls. The value of $\Delta\sigma_v$ imposed on the soil inside the grids is almost zero at the middle of the grid, and increases to about 100 kPa near the grid walls. The maximum average $\Delta\sigma_v$ on the soil-cement grid during rocking (467 kPa) is four times higher than the maximum average $\Delta\sigma_v$ at the end of consolidation (117 kPa, Figure 6.8b), whereas the maximum stress on the enclosed soil increased about three times.

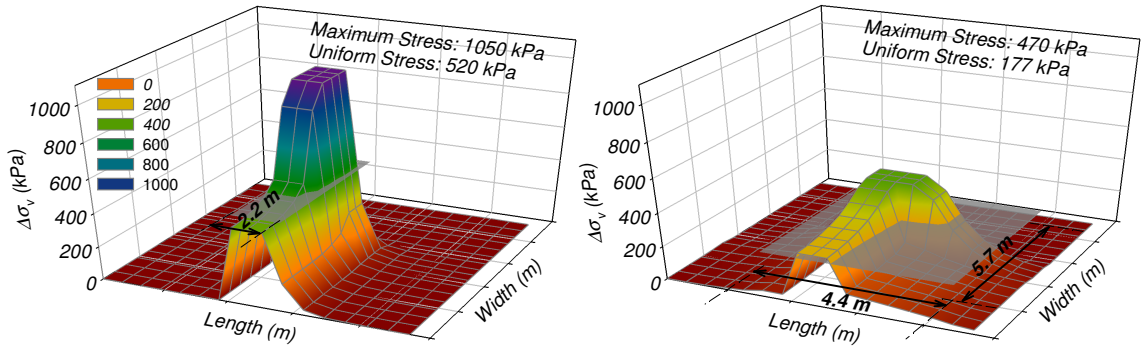

Figure 6.9. Computed change in vertical stress for the embedded grid with A_r = 24% during foundation rocking at $\theta_{ft} \approx 0.006$ rad: (a) change in vertical stress $\Delta\sigma_v$ at the base of the footing; and (b) change in vertical stress $\Delta\sigma_v$ on the surface of soil-cement grid (2.2 m below the footing base).

6.4.3 Sensitivity to Properties of the Sand

The effect of the sand friction angle on the pushover response of the structure and the stresses imposed on the footing base and soil-cement walls are presented in Figure 6.10. In Figures 6.10a and 6.10b, moment versus footing rotation and maximum shear stress in the most strongly loaded zone in the critical juncture versus footing rotation for the embedded grid with A_r = 24% are presented, respectively. For these analyses, friction angles of 35, 40 and 45 degrees were considered, while other parameters were kept constant. In Figures 6.10c and 6.10d, change in vertical stress due to rocking foundation, $\Delta\sigma_v$, along longitudinal (EG-L) and transverse (EG-T) walls for the same grid are presented, respectively. Based on the results, increasing the sand friction angle from 35 to 45 degrees increases the moment capacity of the footing by only 10% (Fig 10a), while the maximum contact stresses beneath the footing increases by about 65% (dashed lines in Figures 6.10c and 6.10d). These results are consistent with the findings of Gajan and Kutter (2008) in indicating that the moment capacity of a rocking foundation on sand is well defined and relatively insensitive to a range of typical friction angles. The maximum shear stress

imposed on the top of the soil-cement grid is approximately the same for all three friction angles (solid lines in Figures 6.10c and 6.10d) because they are largely controlled by yielding in the soil-cement.

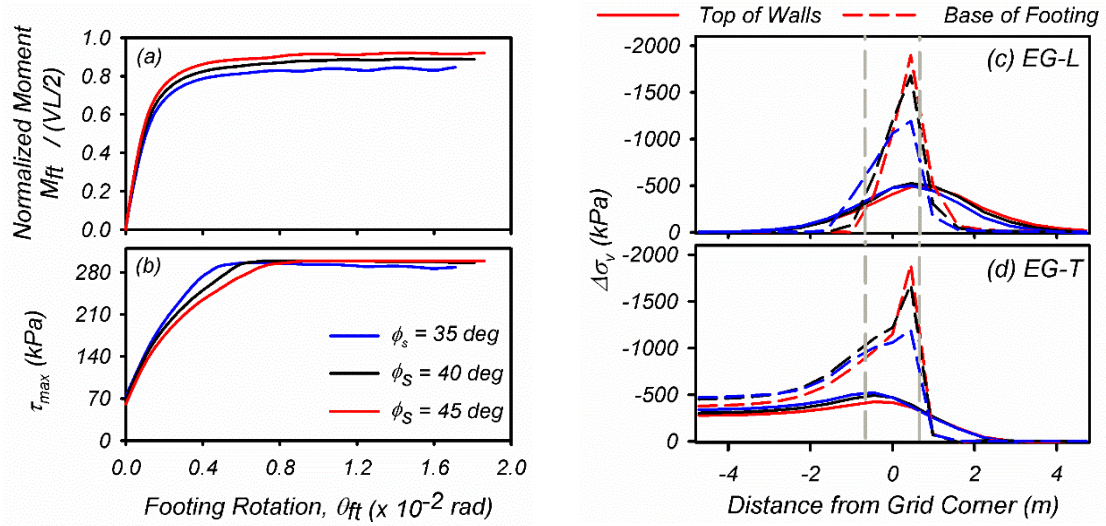

Figure 6.10. Effect of the sand friction angle on the pushover response of structure and stresses imposed on at the footing base and top of the soil-cement walls for the embedded grid with A_r = 24% and H_s = 2.2 m: (a) moment versus footing rotation, (b) maximum shear stress in the soil-cement versus footing rotation, (c) $\Delta\sigma_v$ at the base of the footing and top of the soil-cement grid along the longitudinal wall (EG-L), and (d) $\Delta\sigma_v$ at the base of the footing and top of the soil-cement grid along the transverse wall (EG-T).

6.4.4 Sensitivity to Sand Layer Thickness

Normalized moment versus footing rotation, maximum shear stress in the most strongly loaded zone in the critical juncture versus footing rotation, and change in vertical stress due to foundation rocking, $\Delta\sigma_v$, along longitudinal (EG-L) and transverse (EG-T) walls for the embedded grid with A_r = 24% with the same soil properties but different top sand layer thicknesses of 1.0 and 2.2 meters are presented in Figure 6.11a, b, c, and d, respectively. As shown in Fig 11a, the moment-rotation response of the footing is relatively independent of the sand layer thickness, as is the maximum contact stress of about 1700 kPa beneath the footing base (black dashed line shown previously in Figure 6.10c for a friction angle of 40 degree). The maximum stress imposed on the soil-cement grid, however, increased from 500 kPa for H_s = 2.2 m (solid blue and red lines in Figures 6.11c and 6.11d) to 800 kPa for H_s = 1.0 m (dashed blue and red lines in Figures 6.11c and 6.11d). For both H_s = 1.0 and 2.2 m, the maximum shear stress in the most strongly loaded zone in the soil-cement grid reach the strength of the soil-cement material, but at different footing rotations (Figure 6.11b). In the model with H_s = 1.0 m, the soil-cement grid reaches its capacity limit

at $\theta_{ft} \approx 0.002$ rad which corresponds to $M_{ft}/(VL/2) \approx 0.78$, while in the model with $H_s = 2.2$ m, it occurs at $\theta_{ft} \approx 0.006$ rad (associated with $M_{ft}/(VL/2) \approx 0.90$).

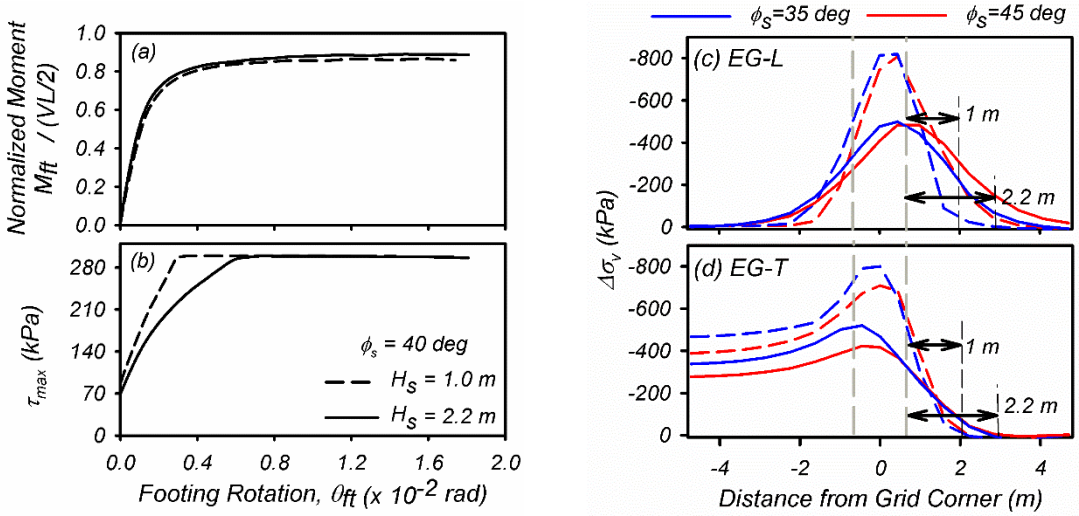

Figure 6.11. Effect of thickness of the top sand layer on the pushover response of structure and stresses imposed on soil-cement walls in the embedded grid with A_r = 24%: (a) moment versus footing rotation, (b) maximum shear stress in the soil-cement versus footing rotation for □s = 40 deg, (c) Δσv along longitudinal wall (EG-L), and (d) Δσv along transverse wall (EG-T)

Contours of strength to stress ratio for a range of 1.0 to 1.3 are shown on the 3D views of the soil-cement grid in Figure 6.12; results for sand layer thicknesses of H_s = 2.2 m, 1.5 m, and 1.0 m are shown in Figures 6.12a, 6.12b, and 6.12c, respectively. The upper range limit is selected based on the typical minimum design values of factor of safety against crushing of the soil-cement materials (Bruce et al. 2013). Yielding of soil-cement grid occurs in zone with strength to stress ratio of about 1.0, which is associated with dark blue zones in these figures. For H_s = 2.2 m (Figure 6.12a), yielding of the soil-cement grid occurs only at the corners of the critical junctures (at the intersection of transverse, EG-T, and longitudinal walls, EG-L under the footing). The degree of over-stressing reduces with depth and reaches to 1.3 at a depth of 3.3 m from top of the soil-cement grid. Reductions in the thickness of the upper sand layer increases the extent of yielding, with yielding (dark blue zone) occurring to depths of up to 1.5 m for the case with H_s = 1.0 (Figure 6.12c). Numerical results suggest that cracking of the soil-cement grid starts at the grid critical juncture where concentration of the stresses is observed during foundation rocking. If yielding of the soil-cement was accompanied by strain-softening (which is not incorporated in the present analyses), stresses would be expected to redistribute from yielding elements

onto other elements, contributing to a spreading of damage along the length of the transverse wall.

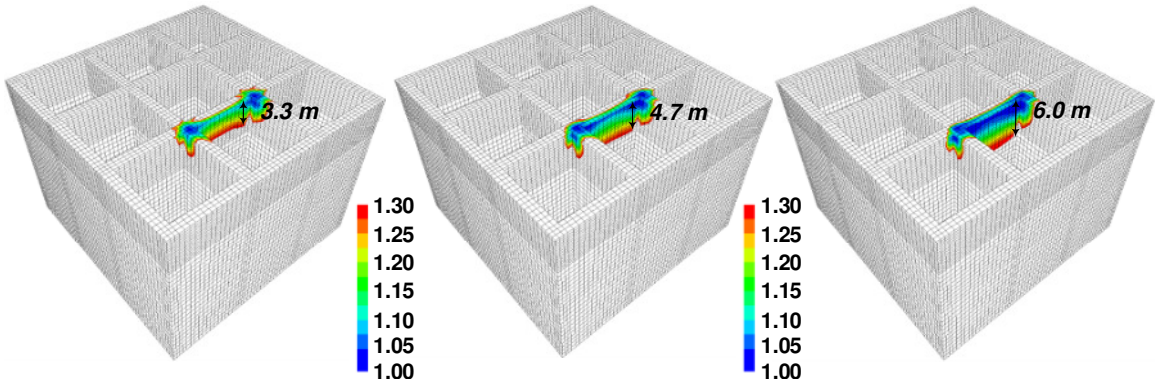

(a) H_s = 2.2 m (b) H_s = 1.5 m (c) H_s = 1.0 m

Figure 6.12. Contour of strength/stress ratio in the range of 1.0 - 1.3 for embedded grid with A_r = 24% under lateral loading.

The numerical maximum shear stresses, τ_{max}, in the critical zone of soil-cement grid are plotted versus H_s in Figure 6.16 (solid and dashed lines) for three different top sand friction angles of 35, 40 and 45 degrees. It was shown that the amount of stresses imposed on soil-cement grid during foundation rocking depends on area replacement ratio, and thickness and friction angle of the top sand layer. For the embedded grid with A_r = 24%, the numerical maximum τ_{max} on the soil-cement grid is 300 kPa regardless of thickness and friction angle of the top sand layer because the maximum shear stress was limited by the strength of the soil-cement material for all these cases (i.e., the walls were yielding in these analyses). For the embedded grid with A_r = 33% (MKH04), however, the numerical τ_{max} values in the critical element ranged from 405 kPa (range of 395 kPa – 410 kPa) for H_s = 1.0 m to 287 kPa (range of 260 kPa – 305 kPa) for H_s = 2.2 m. The average factor of safety against crushing is 1.43 for H_s = 2.2 m suggesting that no crushing of the soil-cement grid is expected. These results are consistent with the absence of cracking in the embedded grid with A_r = 33% (Figure 6.3c).

6.5 Development of a Simplified Procedure

A simplified procedure was developed to estimate the maximum shear stress in the soil-cement grid and potential for crushing of the soil-cement grid based on the results of FLAC3D analyses. Numerical parametric analyses were initially performed to evaluate: (1) state of stresses in the elements in the soil-cement grid, (2) distribution of the vertical

and shear forces transferred to the top of the soil-cement grid, (3) the development of maximum shear stress in the soil-cement grid due to the above stress changes, and (4) stress distribution between the soil-cement grid and surrounding soil. The analysis was performed using the FLAC3D models developed in previous sections, except that the soil-cement materials were kept elastic. The results of the analyses were then used to justify the assumptions for the proposed simplified procedure.

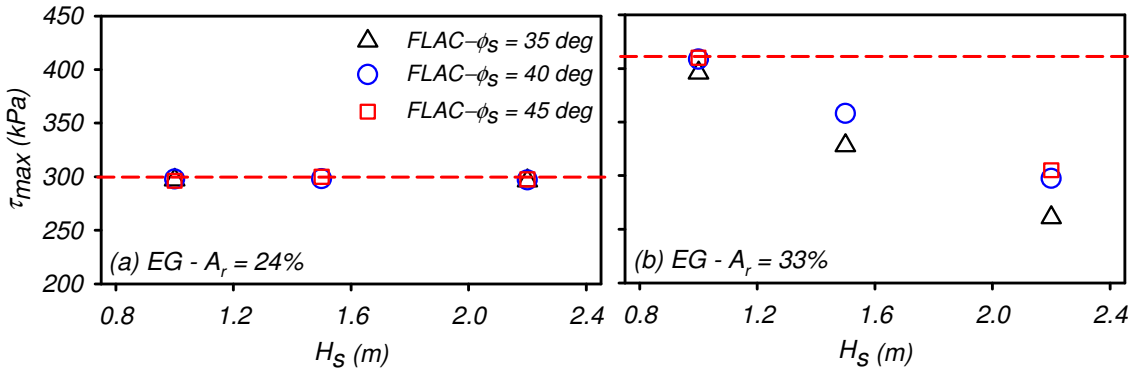

Figure 6.13. Maximum shear stresses in the most strongly loaded zone in the critical juncture for (a) the embedded grid with A_r = 24%, (b) the embedded grid with A_r = 33%.

6.5.1 Numerical Parametric Analyses

Mohr's Circles describing the stress states for different elements in the soil-cement grids with A_r = 24% under the initial soil profile (no structure), static foundation loading, and rocking foundation conditions for the baseline model with H_s = 2.2 m, ϕ_s = 40 degrees are presented in Figure 6.14. The results are for four different soil-cement zones, namely the middle (Figure 6.14a) and most strongly loaded zones of the critical juncture (Figure 6.14b), and the middle (Figure 6.14c) and critical zones at the middle of the transverse wall (Figure 6.14d). The Mohr's Circles for the initial soil profile alone (small black circles) expand under the static foundation loading (red circles), but then grow more dramatically under the rocking foundation loading (blue circles). The normal and shear stresses acting on the soil-cement varied with location along the wall (e.g., on the transverse wall versus critical juncture) and within the walls at each location (e.g., middle versus critical zone at either location). For the most strongly loaded element in the critical juncture, the vertical stress changed from an initial stress of 50 kPa to a vertical stress of 638 kPa during rocking foundation, while the shear stress in the soil-cement element, $\tau_{st\text{-}g}$, was about 60 kPa. Results from numerical simulations indicated that the dominating stress component in the

soil-cement element during rocking foundation was the vertical stress. The shear stress transferred to the soil-cement grid is small compared to the change in vertical stress, which is attributed to the differences in how these stress components spread with depth and the fact that some of the horizontal loads on the structure were carried by lateral earth pressures against the sides of the footing. The four Mohr circles also show the minor principle stress becomes slightly negative during foundation rocking at these critical loading points. With these observations, it appears that the value of τ_{max} developed in the soil-cement due to foundation rocking foundation can be reasonably estimated as simply $\sigma_v / 2$.

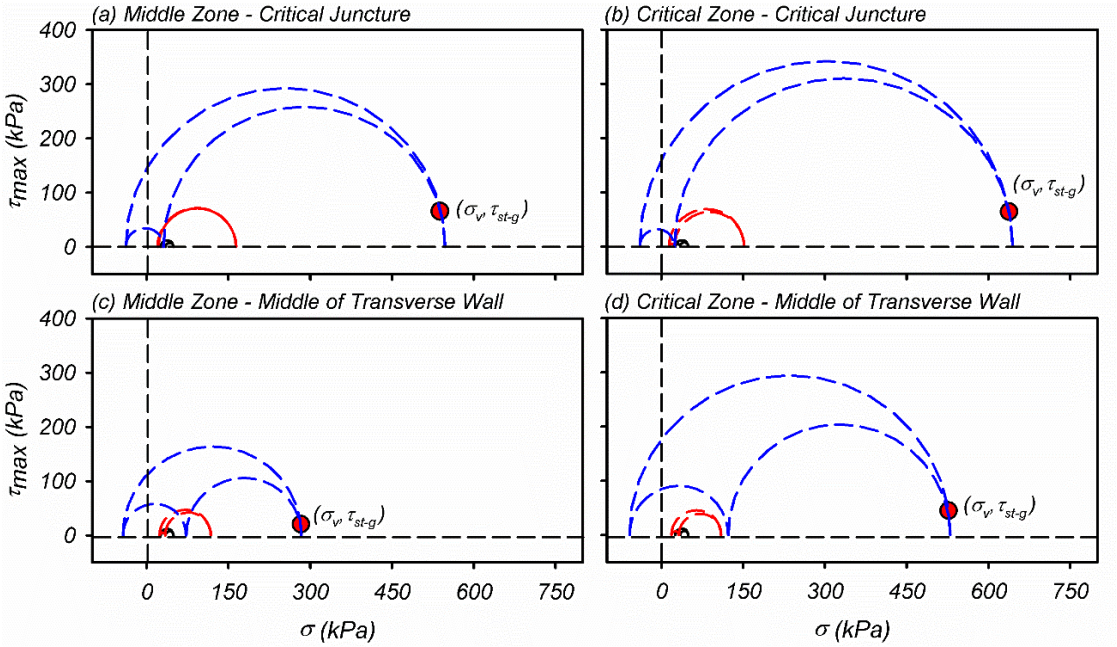

Figure 6.14. Mohr circles for the initial, static and rocking state of stresses in: (a) the middle zone in the critical juncture, (b) the most strongly loaded zone in the critical juncture, (c) the middle zone at the middle of the transverse wall (EG-T), and (d) the most strongly loaded zone at the middle of the transverse wall.

The distributions of the vertical stresses transferred to the top of the soil-cement grid during foundation rocking was presented previously in Figure 6.9. The stress distribution over the soil-cement grid is not uniform and has stress concentration at the intersection of the transverse and longitudinal walls under the footing (critical juncture). The degree of the stress concentrations is expressed relative to the average change in vertical stress as follows. Three different stress concentration ratios, SCRs, for the soil-cement grid were defined based on the results of FLAC3D analysis: (1) ratio of maximum $\Delta\sigma_v$ on the critical juncture to the average $\Delta\sigma_v$ over the grid, CJ_{max}, (2) ratio of average $\Delta\sigma_v$ on the critical

juncture to the average $\Delta\sigma_v$ over the grid, CJ_{ave}, and (3) ratio of average $\Delta\sigma_v$ on transverse wall to the average $\Delta\sigma_v$ over the grid, TW_{ave}. The SCRs were plotted versus H_s in Figure 6.15. These SCRs were then used to evaluate the stress demands over different locations on the soil-cement grid based on the average τ_{max}. For the embedded grid with $A_r = 24\%$ (Figure 6.15a), the average stress concentration ratios, CJ_{max}, CJ_{ave}, and TW_{ave} were about 1.80 (range of 1.61 – 1.93), 1.29 (range of 1.23 – 1.35), and 0.88 (range of 0.85 – 0.93), respectively. For the embedded grid with $A_r = 33\%$ (Figure 6.15b), the stress concentration factors were all closer to unity, especially with $H_s = 2.2$ m (CJ_{max} was only about 1.2 in this case).

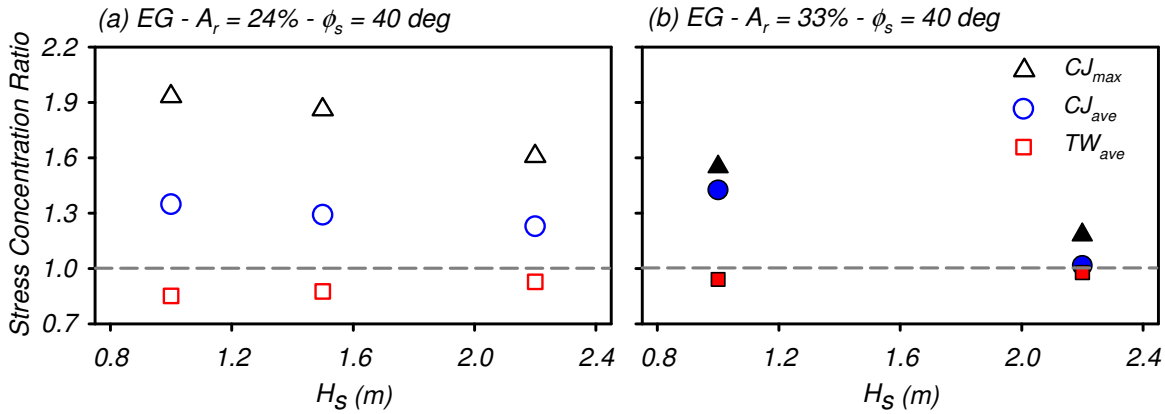

Figure 6.15. Stress concentration ratios from analyses with elastic soil-cement grids: (a) the embedded grid with $A_r = 24\%$, (b) the embedded grid with $A_r = 33\%$.

The effect of relative stiffness of the soil-cement material and the enclosed soil on the stress distribution between the two elements are discussed in Figure 6.16a, in terms of change in vertical stresses over the longitudinal and transverse walls. The results are presented for two soil-cement/clay stiffness ratios (G_G/G_C) of 8.6 and 43.5. In these analyses, shear modulus of clay was kept constant and shear modulus of the soil-cement material was increased. The results showed a slight change (~ 6%) in the maximum vertical stress along both longitudinal and transverse walls. Accordingly, it was found to be reasonable to assume that all the load of the structure is only carried by the soil-cement grid.

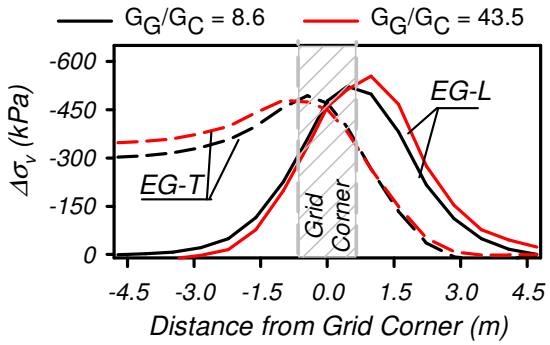

Figure 6.16. Effect of stiffness ratio of soil-cement grid to enclosed soil (GG/GC) on stresses imposed on the embedded grid with A_r = 24% and H_s = 2.2 m during lateral loading.

6.5.2 Proposed Simplified Procedure

The simplified procedure was developed assuming that the footing contact stresses are controlled by the bearing capacity of the sand, after which their redistribution onto the grids needs to be evaluated. A simplified stress distribution for this mechanism is illustrated in Figure 6.17. The moment capacity of the footing was initially estimated assuming a uniform stress distribution (Deng et al., 2012):

$$M_{c-ft} = V\frac{L}{2}\left(1-\frac{A_c}{A}\right) \quad (1)$$

where A = area of the footing; and A_c = minimum bearing area required to support V when the limit bearing capacity of the foundation soil (q_{bLc}) is fully mobilized.

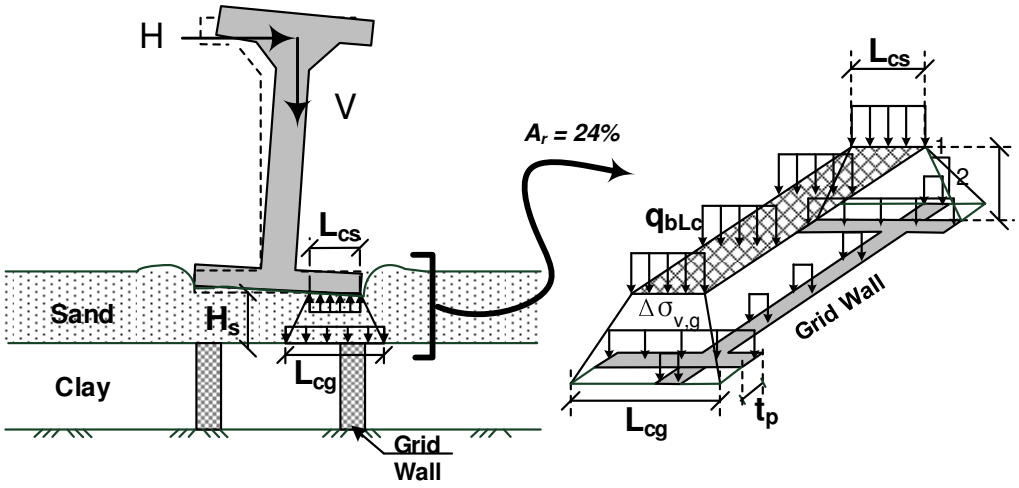

Figure 6.17. Schematic of rocking foundation and 2:1 method for estimating vertical stresses imposed on the top of the soil-cement grid

The value of q_{bLc} under pure vertical loading was obtained using a conventional bearing capacity formulae as:

$$q_{bLc} = S_q d_q q_o N_q + 0.5 S_\gamma d_\gamma \gamma L_{cs} N_\gamma \quad (2)$$

where q_o is the surcharge beside the footing, N_q and N_γ are bearing factors, s_q and s_γ are shape factors, d_q and d_γ are depth factors, and L_{cs} is the length of the contact area ($L_{cs} = A_c/L$ for uni-directional rocking).

The stress transmitted by the rocking footing to the soil-cement grid and surrounding soil was computed based on the assumption that the footing contact stress spreads at a 2(vertical):1(horizontal) slope down to the top of the grid. Vertical stresses calculated using 2V:1H method agree reasonably well with the Boussinesq method for depths between L_c and $4L_c$ below the foundation (Fellenius 2006). The expected stresses carried by the soil-cement grid were then calculated based on the assumption that all stresses in the equivalent loaded area were carried by the grid alone (i.e., the soft clay did not carry any stress). The value of maximum shear stress at different locations in the soil-cement grid (e.g., critical juncture and transverse wall) was then estimated as $SCR \times \tau_{max}$, where SCR is the stress concentration ratio (Figure 6.15).

The state of stress in the soil-cement was then estimated assuming that the total horizontal stresses and horizontal shear stresses are both zero. The maximum shear stress, τ_{max}, in the soil-cement was then estimated as $\sigma_v/2$. Soil-cement crushing is expected when the maximum shear stress, τ_{max}, exceeds the strength of the soil-cement material, $q_{u,cs}/2$.

The analytical results obtained using this simplified procedure are compared to the results from the 3D numerical analyses in Figure 6.18. The analytical and numerical results are all shown for a sand friction angle of 40 degrees. The average maximum shear stress in the soil-cement grids, $\tau_{max,ave}$, computed using the proposed simplified method (without any SCR) are plotted in Figure 6.18 versus H_s as red solid lines. The numerical $\tau_{max,ave}$ in the soil-cement grid are plotted as red solid square symbols. For the embedded grid with $A_r = 24\%$ (Figure 6.18a), the numerical $\tau_{max,ave}$ on the soil-cement grid ranged from about 252 kPa for $H_s = 2.2$ to 315 kPa for $H_s = 1.0$ m. Analyses based on the simplified procedure with $A_r = 24\%$ overestimate $\tau_{max,ave}$ by about 15 to 20%. For the embedded grid with $A_r = 33\%$ (Figure 6.18b), the numerical $\tau_{max,ave}$ ranged from 191 kPa for $H_s = 2.2$ m to 304 kPa for $H_s = 1.0$ m which were 4 to 30% less than the values obtained from the simplified

procedure. The analytical τ_{max} for specific locations were then determined using the average SCRs of CJ_{ave} and CJ_{max} in the critical juncture and TW_{ave} in the transverse wall, and plotted in Figure 6.18 along with numerical τ_{max} values in those locations. Analyses based on the simplified procedure in grids with A_r = 24% and 33% overestimate maximum shear stresses, τ_{max}, over the soil-cement grid by an average of 20% which was approximately similar to the error observed in estimating the $\tau_{max,ave}$ values.

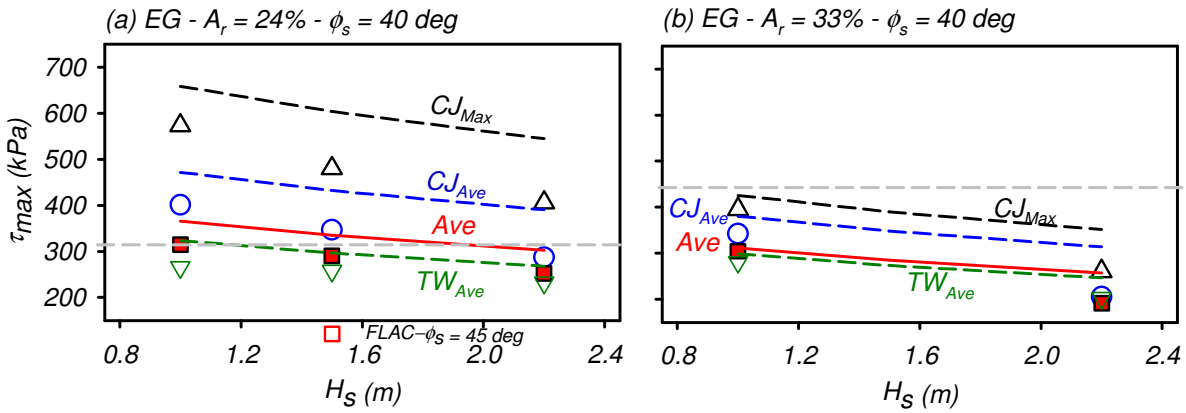

Figure 6.18. Analytical (dashed lines) and 3D numerical (symbols) maximum shear stress results for analyses with elastic soil-cement grids: (a) the embedded grid with A_r = 24%, (b) the embedded grid with A_r = 33%.

The simplified analysis results in Figure 6.18 are consistent with the observed performance of the soil-cement grids in test MKH02 and MKH04. For the embedded grid with A_r = 24% with H_s = 2.2 m (MKH02), the analytical τ_{max} over the soil-cement grid was 302 kPa, giving an average factor of safety slightly less than 1.0 against soil-cement crushing. The critical juncture, however, would be strongly overloaded and expected to develop crushing damage first. Any loss of load carrying capacity in the critical junction would transfer loads to the transverse walls, such that crushing could be expected to progress there as well. Thus, these results are consistent with the crushing observed during model excavation (Figure 6.3b). For the embedded grid with A_r = 33% with H_s = 2.2 m (MKH04), the analytical τ_{max} over the soil-cement grid was 260 kPa, giving a factor of safety of 1.6 against soil-cement crushing. The critical juncture would have a greater τ_{max} of about 351 kPa and a lower factor of safety of 1.17, but it would also not be expected to crush. Therefore, crushing of the soil-cement grid would not be expected for the embedded grid with A_r = 33% (MKH04) which was consistent with the absence of crushing for the grid with A_r = 33% (e.g., Figure 6.3c).

The difference between the simplified procedure and numerical results are due to the net effects of several assumptions: (1) 2V:1H method for stress distribution through the top sand layer depth, (2) the assumption that all stresses in the equivalent loaded area are carried by the grid alone, (3) the use of average stress concentration ratios, (4) neglecting any horizontal shear stress on top of the soil-cement grid, and (5) assuming the total horizontal stress becomes zero during foundation rocking. The above assumptions have some compensating effects, with some contributing to an overestimation of τ_{max} values and others to an underestimation. The errors introduced by these assumptions appear to be relatively small compared to the primary factors of concern (e.g., vertical stresses under the rocking foundation, and the strength of the soil-cement) and the net error is conservative for the cases summarized in Figure 6.18.

6.6 Conclusion

The purpose of the 3D analysis was to: (1) to evaluate and validate the numerical model's ability to estimate stress distributions and damage in the soil-cement grid due to stresses imposed during foundation rocking, (2) to evaluate the parameters that control the stress distribution beyond those covered in the centrifuge tests, (3) to develop a simplified procedure for design purposes. The 3D numerical pushover analyses provided reasonable prediction of: (1) structural rocking response, and (2) the zone of expected crushing or lack of crushing. Moment-rotation response of structures under monotonic lateral loading are shown to be reasonably consistent with the results of dynamic centrifuge tests for a range of stresses less than the strength of soil-cement grid.

A series of parametric analyses were performed for a range of geometries, and soil properties. The parametric analysis showed that the potential for damage to the soil-cement grid depends on the thickness and strength of the top sand layer, area replacement ratio, and the strength of the soil-cement grid. A simplified analysis method for estimating stress transfer from rocking foundations to the top of the soil-cement grid was developed based on the assumptions that: (1) the footing contact stress spreads at a 2(vertical):1(horizontal) slope down to the top of the grid, (2) all stresses in the equivalent loaded area are carried by the grid alone, (3) stress concentration ratios for the critical junctures and transverse walls from the 3D analyses are reasonable, (4) horizontal shear stresses imposed on the

soil-cement grid from the rocking foundation are negligible, and (5) the total horizontal stress is zero during foundation rocking. The proposed simplified procedure provided results that appear slightly conservative relative to the 3D numerical results and were shown to reasonably distinguish between the conditions that did and did not results in crushing of the soil-cement grid in these centrifuge tests.

7 Summary and outlook

7.1 Summary

Dynamic centrifuge model tests and three-dimensional, nonlinear finite difference, pushover analyses were used to study: (1) the effects of soil-cement grid reinforcement on the seismic response of soft soil, (2) the response of structures supported by shallow foundations on soft clay reinforced by embedded and floating soil-cement grids, and (3) possible effect of partial damage to the soil-cement grid reinforcement on its ability to withstand applied forces and stresses. The results of these analyses were used to develop simplified procedures for estimating the inertial and kinematic loads imposed on the soil-cement grids provided results which were reasonably consistent with the observed damage patterns; i.e., the loading conditions which produced crushing near the tops of the walls and cracking at larger depths.

7.2 Small Centrifuge Tests

At the preliminary stages of this study, a series of small centrifuge tests were carried out to develop: (1) soil-cement mix designs; (2) soil-cement construction technique for centrifuge model tests; and (3) a crack detection technique to track the crack propagation along the height and length of soil-cement panels. Preliminary dynamic centrifuge tests were also performed to evaluate the testing efficacy. Different soil-cement mixtures were examined and it was found that the critical factors influencing the strength gain of the mixture are the cement type, curing environment and soil-cement-water ratio. Strength, workability and setting time of the soil-cement mixture are the key parameters which were considered in the selection of the soil cement mix to be used in the planned centrifuge tests. The tests also showed that centrifuge models of soil-cement grid reinforced soil could be constructed using trenching and excavation technique and the results could be used to examine system-level performance, including the effects of grid cracking.

7.3 The Effect of Ground Reinforcement on the Seismic Response of Soft Soil

A series of large centrifuge models was used to study the effects of soil-cement grid reinforcement on the seismic response of a deep, lightly over-consolidated clay profile. The model tests included an unreinforced soil profile and soil profiles reinforced with three

different grid configurations. Recorded responses during 13 different shaking events were used to examine the nonlinear response characteristics of the unreinforced and reinforced profiles, and the internal interactions between the soil-cement grids and enclosed soils. The experimental data were archived (Khosravi et al. 2015c,e) for public distribution and use in the validation of numerical analysis methods.

The soft clay profile, without any reinforcement, developed strong nonlinearity at the stronger levels of shaking. The soft clay developed peak shear strains up to 2.5% and peak r_u values of 78% for the stronger Kobe motion (PBA = 0.18g), accompanied by significant lengthening of the soil profile's effective natural period.

The embedded grid with A_r = 24% significantly stiffened the site compared to the site with no reinforcement, resulting in stronger accelerations at the ground surface for the input motions used in this study. The soil-cement grid showed some nonlinearity in its response during the stronger shaking events; e.g., the Kobe motion with PBA = 0.18g produced peak shear strains up to 1% and r_u values of 100% in the reinforced soil and minor cracking in the soil-cement walls. The dynamic horizontal displacements of the transverse walls and enclosed soils were significantly greater than those for the longitudinal walls, indicating significant flexure in the transverse grid walls.

The embedded grid with A_r = 33% further stiffened the site and also produced stronger accelerations at the ground surface. The soil-cement grid did not, however, exhibit signs of significant nonlinearity in its response for any of the imposed shaking events; e.g., the Kobe motion with PBA = 0.16g produced peak shear strains of only 0.15% in the reinforced soil and no cracking in the soil-cement walls. The dynamic horizontal displacements of the transverse walls, enclosed soils, and longitudinal walls were essentially the same, indicative of relatively minor flexure in the transverse grid walls.

The floating grid with A_r = 33% effectively stiffened the upper portion of the clay profile, but its dynamic response was affected by strong nonlinearity in the soft clay beneath the grid during the strong shaking events; e.g., the Kobe motion with PBA = 0.16g produced peak shear strains up to 1.0% in clay beneath the grids, whereas the clay inside the grid cells remained relatively linear. Spectral amplification ratios were intermediate to those for the untreated soil and embedded grid (A_r = 33%), as expected. Displacements of

the transverse and longitudinal walls were essentially the same and no cracking of the walls was observed.

The results of these experiments and analyses provide insights on the dynamic performance of soil-cement grids and the internal interactions between the grids and enclosed soils. The potential for tensile stresses and cracking in the longitudinal soil-cement walls was evaluated using a simplified analysis method, but the effects of transverse wall flexure and stress concentrations at grid corners will require more detailed analyses. The archived dataset provides a basis for future evaluation of these and other issues as part of validating design and numerical analysis procedures for the seismic performance of soil-cement grid reinforcement systems.

7.4 Dynamic Response of Structures with Shallow Foundation over Soft Soil Reinforced with Soil-Cement Grid

7.4.1 Dynamic Centrifuge Tests

Dynamic centrifuge model tests were performed to investigate the dynamic response of structures supported by shallow foundations on soft clay reinforced by embedded and floating soil-cement grids with area replacement ratios of 24 and 33%. Responses of three structures to a series of input motions were used to examine the moment-rotation-settlement responses of the footings and the performance of the soil-cement grids. The experimental data were archived for open distribution.

Footing settlements during shaking were controlled by the degree of footing rocking and the stresses imposed on the soil-cement grids. Shaking-induced footing settlements remained small (<15 mm) when the footing moment due to the inertial loads from the superstructure were less than 90% of the estimated footing moment capacity ($M_{c,ft}$), peak footing rotations were less than 0.004 rad, and the stresses transmitted to the soil-cement were less than its unconfined compressive strength. The greatest footing settlement was 230 mm for the footing on an embedded grid with A_r = 24% (MKH02) during the strongest Kobe motion with a PBA = 0.53g, which fully mobilized the footing's moment capacity, produced peak footing rotations of 0.02 rad, and caused local crushing of the soil-cement under the footing. The footing settlements were only 30-40 mm for the footings on the embedded and floating grids with A_r = 33% (MKH04) during the same strongest Kobe

motion, which also fully mobilized the footing moment capacities but did not cause any visible damage to the soil-cement under the footings. Additional post-shaking footing settlements attributed to dissipation of shaking-induced excess pore water pressures in the soft clay were small (<15 mm) for the embedded grids with A_r = 24% or 33% in all events, but did reach 120 mm for the floating grid during the strongest Kobe motion.

Simplified analysis methods for estimating the inertial and kinematic loads imposed on the soil-cement grids provided results which were reasonably consistent with the observed damage patterns; i.e., the loading conditions which produced crushing near the tops of the walls and cracking at larger depths. The inertial loads imposed by the structures were evaluated by assuming that the footing contact stresses are controlled by the bearing capacity of the sand, after which the stress was redistributed at a 2:1 slope to the top of the grids. This mechanism produced results which reasonably distinguished between conditions which did and did not produce crushing near the tops of the walls. The simplified analyses for the rocking response of the structures also provided accurate estimates of the footing moment capacities and the base shear coefficients at the onset of rocking. The simplified analysis for kinematic loading of the soil-cement grid, which was based on the procedure described in Khosravi et al. (2016), provided results which reasonably distinguished between the conditions which did and did not produce cracking in the soil-cement walls at larger depths.

The results of these centrifuge tests demonstrate the potential effectiveness of soil-cement grids for supporting structures on shallow foundations at soft soil sites, and provide a basis for validating future advances in equivalent-static or nonlinear dynamic analysis methods for these types of ground reinforcement systems.

7.4.2 3D Numerical Simulations

The purpose of the 3D analysis was to: (1) to evaluate and validate the numerical model's ability to estimate stress distributions and damage in the soil-cement grid due to stresses imposed during foundation rocking, (2) to evaluate the parameters that control the stress distribution beyond those covered in the centrifuge tests, (3) to develop a simplified procedure for design purposes. The 3D numerical pushover analyses provided reasonable

prediction of: (1) structural rocking response, and (2) the zone of expected crushing or lack of crushing. Moment-rotation response of structures under monotonic lateral loading are shown to be reasonably consistent with the results of dynamic centrifuge tests for a range of stresses less than the strength of soil-cement grid.

A series of parametric analyses were performed for a range of geometries, and soil properties. The parametric analysis showed that the potential for damage to the soil-cement grid depends on the thickness and strength of the top sand layer, area replacement ratio, and the strength of the soil-cement grid. A simplified analysis method for estimating stress transfer from rocking foundations to the top of the soil-cement grid was developed based on the assumptions that: (1) the footing contact stress spreads at a 2(vertical):1(horizontal) slope down to the top of the grid, (2) all stresses in the equivalent loaded area are carried by the grid alone, (3) stress concentration ratios for the critical junctures and transverse walls from the 3D analyses are reasonable, (4) horizontal shear stresses imposed on the soil-cement grid from the rocking foundation are negligible, and (5) the total horizontal stress is zero during foundation rocking. The proposed simplified procedure provided results that appear slightly conservative relative to the 3D numerical results and were shown to reasonably distinguish between the conditions that did and did not results in crushing of the soil-cement grid in these centrifuge tests.

7.5 Recommendation for Future Research

This research has improved the understanding regarding the reinforcement mechanisms of soil-cement grid in terms of distributing shear stresses and strains, and the internal interactions between the grids and enclosed soils. It demonstrated the potential effectiveness of soil-cement grids for supporting structures on shallow foundations at soft soil sites and provided simplified procedures for first-order estimation of the inertial and kinematic load demands imposed on the soil-cement grids. Several additional research areas have been identified which could benefit from additional research in the future. A brief description of these topics are discussed in this section.

- Research is needed to understand the effect of partial damage to the soil-cement ground reinforcement on its ability to limit settlements or deformations to acceptable levels during a given or future earthquake. The current study mainly focused on the response of soil-

cement grid supporting structures over soft clay. Results from experiments showed that structure could survive during a severe earthquake, and grid could stand static loads of the structure even after partial damage. However, the effect of partial damage on the response of structures and embankment in future earthquake has not been investigated in details. This is more critical for soil-cement walls or grids supporting an embankment, or using for mitigation of lateral spreading. Investigation of the effect of partial damage of the soil-cement ground reinforcement requires to (1) develop a quantitative measure for characterizing damage (e.g. offsets, crack sizes), since the performance of the damaged soil-cement grid depends on level and extension of the damage in the soil-cement grid, (2) develop a technique (e.g. non-destructive testing methods such as Impact-Echo, and inclinometer tubes) to inspect wall integrity after a major earthquake, and (3) understand the post-cracking behavior of soil-cement ground reinforcement (e.g. wall, or grid). Post-cracking behavior of soil-cement ground reinforcement can be investigated through: (1) conducting element scale tests to study cracking and post-cracking behavior of soil-cement samples under different loading conditions, and (2) conducting model tests, the results of which can be used to develop and validate numerical models to study the mechanism dominating the behavior of the cracked wall system (e.g. frictional behavior).

- Numerical modeling of the progressive failure of brittle material such as soil-cement material is challenging. Current work has explored one area of this modeling, which is evaluating and validating the numerical model's ability to estimate stress distributions and damage in the soil-cement grid during foundation rocking. Soil-cement material were modeled using Mohr-Coulomb which cannot accurately simulate how that progressive damage is related to structural settlement, or to the ability to maintain stability of a slope. This could be investigated using more advanced constitutive models incorporating strain-softening. The results of current centrifuge tests can be used to validate these numerical models. The validated model can be used to investigate other parameters that were found controlling the response of foundation rocking such as number of rotation cycles.
- Research is required to investigate the seismic response of embankment over soft or liquefiable soil reinforced with soil-cement ground reinforcement. This need could be met through numerical simulation using a numerical program such as FLAC. The FLAC model can be calibrated using the data from the large centrifuge test that has been performed

recently at the center for geotechnical modeling at UC Davis on an embankment over liquefiable soil reinforced by soil-cement grid. The validated model could be used to develop guidance on how to define design parameters in particular the strength properties of the reinforced zone when using the simpler analysis methods common in current practice.

References

Adalier, K., Elgamal, A. K., and Martin, G. R. (1998). "Foundation Liquefaction Countermeasures for Earth Embankments." *J. of Geotech. and Geoenviron. Eng.*, 124(6), 500-517.

Allmond, J., and Kutter, B. L. (2013). "Centrifuge testing of rocking foundations on saturated and submerged sand: Centrifuge Data Report for JDA02." *Data Report, UCD/CGMDR-13/01*, University of California at Davis, Davis, CA

Almeida M. S. S., Davies M. C. R., and Parry R. H. G. (1985)"Centrifuge tests of embankments on strengthened and unstrengthened clay foundations." *Geotechnique*, 35(4), 425-441.

Babasaki R., SU Suzuki K. and Suzuki Y., (1992). "Centrifuge tests on improved ground for liquefaction." *Proc. of the 10th World Conference on Earthquake Engineering*. Balkema, Rotterdam, the Netherlands, 1461-1464.

Babasaki, R., Suzuki, K., Saitoh, S., Suzuki, Y., and Tokitoh, K. (1991). "Construction and Testing of Deep Foundation Improvement Using the Deep Cement Mixing Method." *Deep Foundation Improvements: Design, Construction, and Testing*, ASTM STP 1089, 1991, Philadelphia, 224-234.

Bradley, B.A., Araki, K., Ishii, T. and Saitoh, K. (2013). "Effect of lattice-shaped ground improvement geometry on seismic response of liquefiable soil deposits via 3-D seismic effective stress analysis." *Soil Dynamics and Earthquake Eng.,* 48. 35-47.

Brandenberg, S.J., Wilson, D.W. and Rashid, M.M. (2010). "Weighted residual numerical differentiation algorithm applied to experimental bending moment data." *J. of Geotech. and Geoenviron. Eng.*, 136 (6), 854-863.

Bruce, M.E.C., Berg, R.R., Collin, J.G., Filz, G.M., Terashi, M., and Yang D.S. (2013). "Deep Mixing for Embankment and Foundation Support." *Report No. FHWA-HRT-13-046, Federal Highway Administration*, Washington, DC.

Deng, L., Kutter, B. L., and Kunnath, S. K. (2012). "Centrifuge modeling of bridge systems

designed for rocking foundations." *J. Geotech. Geoenviron. Eng.*, 10.1061/(ASCE)GT.1943-5606.0000605, 335–344

Dilena, M., and Morassi, A. (2004). "The use of antiresonances for crack detection in beams." *Journal of Sound and Vibration*, 276(1), 195-214.

Fukutake K, Ohtsuki A. (1995). "Three dimensional Liquefaction analysis of partially improved ground." *Proc. of the First International Conference on Earthquake Geotechnical Engineering*. Japan, Balkema, Brookfield, ISBN 90 5410 578X, 863-68.

Gajan, S. and Kutter, B. (2008). "Effect of Critical Contact Area Ratio on Moment Capacity of Rocking Shallow Footings." *Geotechnical Earthquake Engineering and Soil Dynamics IV*: 1-11.doi: 10.1061/40975(318)133

Gu, X., Chen, Z., and Ansari, F. (2000). "Embedded fiber optic crack sensor for reinforced concrete structures." *ACI Structural Journal*, 97(3), pp.468-476

Hausler, E.A. and Sitar, N. (2001). "Performance of Soil Improvement Techniques in Earthquakes." *Fourth International Conference on Recent Advances in Geotechnical Earthquake Engineering and Soil Dynamics*, March 26 - 31.

Inagaki, M., Abe, T., Yamamoto, M., Nozu, M., Yanagawa, Y., and Li, L., (2002). "Behavior of cement deep mixing columns under road embankment." *Physical Modelling in Geotechnics*, ICPMG '02, pp. 967-972.

Ishikawa, A., and Asaka, Y. (2006). "Seismic responses of column and grid-type improved grounds. Physical modelling in geotechnics." *ICPMG '06 International conference; 6th, Physical modelling in geotechnics*, ICPMG '06, 521-526

Kamai, R., and Boulanger, R. W. (2010). "Characterizing localization processes during liquefaction using inverse analyses of instrumentation arrays." *Meso-Scale Shear Physics in Earthquake and Landslide Mechanics*, Y. H. Hatzor, J. Sulem, and I. Vardoulakis, eds., CRC Press/Balkema, Netherlands, 219–238.

Karimi, Z., and Dashti, S. (2015a). "Numerical Simulation of Earthquake Induced Soil Liquefaction: Validation against Centrifuge Experimental Results." *IFCEE 2015*, Geo-institute, ASCE, USA, 11-20. doi: 10.1061/9780784479087.002.

Karimi, Z., and Dashti, S., (2015b). "Numerical and Centrifuge Modeling of Seismic Soil–

Foundation–Structure Interaction on Liquefiable Ground." *J. Geotech. Geoenviron. Eng.* (10.1061/(ASCE)GT.1943-5606.0001346 , 04015061.

Karimi, Z. and Dashti, S. (2016a). "Seismic Performance of Shallow Founded Structures on Liquefiable Ground: Validation of Numerical Simulations Using Centrifuge Experiments." *J. Geotech. Geoenviron. Eng.*, 10.1061/(ASCE)GT.1943-5606.0001479, 04016011.

Karimi, Z., and Dashti, S. (2016b). "Effects of Ground Motion Intensity Measures on Liquefaction Triggering and Settlement near Structures." *ICONHIC2016*, June 2016, Chania, Greece.

Khosravi, M., Wilson, D. W., Boulanger, R. W., Olgun, C. G., Tamura, S., Wang, Y., Rayamajhi, D., (2015a). "1-M Radius Centrifuge Experiments: Seismic response of soft soil reinforced with soil-cement grid-Construction procedure", Network for Earthquake Engineering Simulation (distributor), Dataset.

Khosravi, M., Tamura, S., Boulanger, R. W., Wilson, D. W., Olgun, C. G., Rayamajhi, D., Wang, Y. (2015b). "Dynamic Centrifuge Tests on Soft Clay Reinforced by Soil-Cement Grids." *IFCEE 2015*, 2349-2358, doi 10.1061/9780784479087.218.

Khosravi, M., Wilson, D. W., Boulanger, R. W., Olgun, C. G., Tamura, S., Wang, Y. (2015c). "Test MKH01: Dynamic Centrifuge Tests of Soft Clay Reinforced by Soil-Cement Grids," *Network for Earthquake Engineering Simulation (distributor),* Dataset, doi:10.4231/D3HD7NT63

Khosravi, M., Wilson, D. W., Boulanger, R. W., Olgun, C. G., Tamura, S., Wang, Y., (2015d). "Test MKH02: Dynamic Centrifuge Tests of Structures on Soft Clay Reinforced by Soil-Cement Grids", *Network for Earthquake Engineering Simulation (distributor),* Dataset, doi:10.4231/D38P5VB1Q

Khosravi, M., Boulanger, R. W., Wilson, D. W., Tamura, S., Olgun, C. G., Wang, Y., (2015e). "Seismic Performance of Soil-Cement Grid Supporting a Structure over Soft Clay." *The Deep Mixing 2015 Conference,* San Francisco, CA, 631-640.

Khosravi, M., Boulanger, R., Tamura, S., Wilson, D., Olgun, C., and Wang, Y. (2016).

"Dynamic Centrifuge Tests of Soft Clay Reinforced by Soil–Cement Grids." *J. Geotech. Geoenviron. Eng.*, 10.1061/(ASCE)GT.1943-5606.0001487, 04016027.

Khosravi, M., Boulanger, R.W., Tamura, S., Wilson, D. W., Olgun, C.G., Wang, Y. (2016b). "Dynamic Centrifuge Tests of Structures with Shallow Foundations on Soft Clay Reinforced by Soil-Cement Grids", *Soils and Foundations* (submitted for review).

Khosravi, M., Boulanger, R.W., Tamura, S., Wilson, D. W., Olgun, C.G., Wang, Y. (2016c). "Numerical Simulations of Dynamic Centrifuge Tests of Structures with Shallow Foundations on Soft Clay Reinforced by Soil-Cement Grids", *J. Geotech. Geoenviron. Eng.*, (in preparation).

Kitazume, M., Okano, K., and Miyajima, S., (2000). "Centrifuge model tests on failure envelope of column type deep mixing method improved ground." *Soils and Foundations*, 40(4), pp. 43-55.

Kitazume, M. and Karastanev, D., (1996). "Bearing capacity of improved ground with column type DMM." *Grouting and Deep Mixing, Proceedings of IS-Tokyo 96, 2nd International Conference on Ground Improvement Geosystems*, pp. 503-508.

Kitazume, M. and Maruyama, K. (2006). "External stability of group column type deep mixing improved ground under embankment." *Soils and Foundations*, 46(3), 323-340.

Kitazume, M. and Maruyama, K. (2007). "Internal Stability of Group Column Type Deep Mixing Improved Ground under Embankment Loading", *Soils and Foundations*, 47(3), pp. 437-455.

Kitazume, M. and Terashi, M. (2014). "The Deep Mixing Method." Tayler & Francis Group, London, UK, 410 p.

Kutter, B. L. (1995). "Recent Advances in Centrifuge Modeling of Seismic Shaking (State-of-the-Art Paper)." *Proceeding of 3rd International Conference on Recent Advances in Geotechnical Earthquake Engineering and Soil Dynamics*, 2, 927-942.

Li, L., Chan, P., and Lytton, R. L. (1991). "Detection of thin cracks on noisy pavement images." *Transportation Research Record*, (1311).

Matsuo, O. and Shimazu, T., Goto, Y., Suzuki, Y., Okumura, R., and Kuwabara, M. (1996).

"Deep Mixing Method as a liquefaction prevention measure." *Proc., 2nd Int. Symp. on ground improvement geosystems*, Tokyo, 521-526.

Mitchell, J.K. (2008). "Mitigation of Liquefaction Potential of Silty Sands." *From Research to Practice in Geotechnical Engineering Congress*, 433-451

Miyake, M., Wada, M., and Satoh, T., (1991). "Deformation and strength of ground improved by cement treated soil columns." *Proceedings International Conference on Geotechnical for Coastal Development* (GEO-COAST '91), pp. 369-380.

Namikawa, T., Koseki, J., Suzuki, Y. (2007). "Finite element analysis of lattice-shaped ground improvement by cement-mixing for liquefaction mitigation." *Soils and Foundations*, 47(3), 559–576.

Nguyen, T. V., Rayamajhi, D., Boulanger, R. W., Ashford, S. A., Lu, J., Elgamal, A., and Shao, L. (2013). "Design of DSM Grids for Liquefaction Remediation." *J. Geotech. Geoenviron. Eng.*, 140(3), 1923-1933.

Puebla, H., Butler, R.C., O'Neill, E.S., and Williams, R.R. (2006). "Static and Seismic Stress-Deformation Analyses of a Deep Soil Mix Wall." *4th International FLAC Symposium on Numerical Modeling in Geomechanics*, Madrid, Spain.

Rayamajhi, D., Nguyen, T. V., Ashford, S. A., Boulanger, R. W., Lu, J., Elgamal, A., and Shao, L. (2014a). "Numerical Study of Shear Stress Distribution for Discrete Columns in Liquefiable Soils." *J. Geotech. Geoenviron. Eng.*,140(3), 04013034.

Rayamajhi, D., Tamura, S., Khosravi, M., Boulanger, R.W., Wilson, D., Ashford, S.A., and Olgun, C.G. (2014b). "Dynamic Centrifuge Tests to Evaluate Reinforcing Mechanisms of Soil-Cement Columns in Liquefiable Sand." *10.1061/(ASCE)GT.1943-5606.0001298, 04015015*.

Rayamajhi, D., Tamura, S., Khosravi, M., Boulanger, R.W., Wilson, D., Ashford, S.A., and Olgun, C.G. (2014c). "Reinforcing effects of soil-cement columns in liquefiable sand." Data Report, UCD/CGMDR-14/01, University of California, Davis, CA.

Rayamajhi, D., Tamura, S., Khosravi, M., Boulanger, R. W., Wilson, D.W., Ashford, S. A., and, Olgun, C.G. (2015). "Investigating Reinforcing Effects of Soil-Cement

Columns on Liquefiable Sand using Dynamic Centrifuge Tests.", *DFI Deep Mixing 2015*, San Francisco, CA.

Rayamajhi, D., Ashford, S. A., and, Elgamal, A. (2016). I. "Stone Columns in Liquefiable Soils: Shear Reinforcement and Cyclic Stress Ratio Reductions." *J. Geotech. Geoenviron. Eng*, 10.1061/(ASCE)GT.1943-5606.0001474, 04016023.

O'Rourke, T. D., Goh, S. H. (1997). "Reduction of liquefaction hazards by deep soil mixing." *Proc. of the NCEER/INCEDE workshop*, MCEER, University of Buffalo, Buffalo, NY, 1997, 87-105.

Salawu, O. S. (1997). "Detection of structural damage through changes in frequency: a review." *Engineering structures*, 19(9), 718-723.

Schofield, A. N. (1981). "Dynamic and earthquake geotechnical centrifuge modeling." *Proc., Int. Conf. on Recent Advances in Geotechnical Earthquake Engineering and Soil Dynamics*, Vol. 3, Missouri Univ. of Science and Technology, Rolla, MO, 1081–1100.

Shiotani, T., Ohtsu, M., and Ikeda, K. (2001). "Detection and evaluation of AE waves due to rock deformation." *Construction and Building Materials*, 15(5), 235-246.

Sinha, S. K., and Fieguth, P. W. (2006). "Automated detection of cracks in buried concrete pipe images." *Automation in Construction*, 15(1), 58-72

Stringer, M.E., Kutter, B.L., Wislon, D.W., Zhou, Y.G., Zheng, B.L., 2012. "Steel Pile Jacket Seismic Soil Structure Interaction Study: Phase 2 Data Report." *Center for - Geotechnical Modeling*, Report No. UCD/CGMDR-12/02.

Takahashi, H., Kitazume, M., Ishibashi, S. (2006). "Effect of deep mixing wall spacing on liquefaction mitigation." *Proc. of the 6th international conference on physical modelling in geotechnics*, 585-590.

Tokimatsu, K., Mizuno, H., Kakurai, M. (1996). "Building damage associated with geotechnical problems." *Soils and Foundations*, special issue on Geotechnical Aspects of the January 17, 1995 Hyogoken-Nambu Earthquake, 1, 219-234.

Tokunaga, S., Kitazume, M., Morikawa, Y., Takahashi, H., Nagatsu, T., Honda, N., Onishi, T., Asanuma, T., Kubo, S., Higashi, S. (2015). "Performance of cement deep mixing

method in 2011 tohoku earthquake." *The Deep Mixing 2015 Conference*, San Francisco, CA, 1071-1080.

Takahashi, H., Kitazume, M., Ishibashi, S. (2006). "Effect of deep mixing wall spacing on liquefaction mitigation." *Proc. of the 6th international conference on physical modelling in geotechnics*, 585-590.

Yamashita, K., Hamada, J., Onimaru, S., Higashino, M., (2012). “Seismic behavior of piled raft with ground improvement supporting a base-isolated building on soft ground in Tokyo." *Soils and Foundations*, 52(5), 1000–1015.

Appendix A: List of publications

A.1 Journal Publications

Rayamajhi, D., Tamura, S., **Khosravi, M.,** Boulanger, R.W., Wilson, D., Ashford, S.A., and Olgun, C.G. (2014). "Dynamic Centrifuge Tests to Evaluate Reinforcing Mechanisms of Soil-Cement Columns in Liquefiable Sand." *Journal of Geotechnical and Geoenvironmental Engineering*, 140(3), 04015015.

Khosravi, M., Boulanger, R. W., Wilson, D. W., Tamura, S., Olgun, C. G., Wang, Y., (2016). "Dynamic Centrifuge Tests of Soft Clay Reinforced by Soil-Cement Grids." *Journal of Geotechnical and Geoenvironmental Engineering*, 10.1061/(ASCE)GT. 1943-5606.0001487, 04016027.

Khosravi, M., Boulanger, R.W., Tamura, S., Wilson, D. W., Olgun, C.G., Wang, Y. (2016). "Dynamic Centrifuge Tests of Structures with Shallow Foundations on Soft Clay Reinforced by Soil-Cement Grids", *Soils and Foundations* (submitted for review).

Wang, Y., Wilson, D.W., **Khosravi, M.,** Yuan X., and Olgun, C.. (2016) "Evaluation of Cyclic Shear Stress-Strain Using Inverse Analysis Techniques in Dynamic Centrifuge Tests". *Chinese Journal of Geotechnical Engineering*, 38(2), 271-277.

Tamura, S., **Khosravi, M.,** Boulanger, R. W., Wilson, D. W., Olgun, C. G., D. Rayamajhi, Wang, Y. (2016). "Simple Method for Detecting Cracks in Soil-Cement Mixture in Centrifuge Modeling", Journal of Physical Modelling in Geotechnics (In Preparation).

Khosravi, M., Boulanger, R.W., Tamura, S., Wilson, D. W., Olgun, C.G., Wang, Y. (2016). "Numerical Simulations of Dynamic Centrifuge Tests of Structures with Shallow Foundations on Soft Clay Reinforced by Soil-Cement Grids", *Soils and Foundations* (submitted for review).

A.2 Conference Proceedings

Khosravi, M., Tamura, S., Boulanger, R. W., Wilson, D. W., Olgun, C. G., Rayamajhi, D., Wang, Y. (2015). "Dynamic Centrifuge Tests on Soft Clay Reinforced by Soil-Cement Grids." *IFCEE 2015*, 2349-2358.

Khosravi, M., Boulanger, R. W., Wilson, D. W., Tamura, S., Olgun, C. G., Wang, Y.,

(2015). "Seismic Performance of Soil-Cement Grid Supporting a Structure over Soft Clay." The Deep Mixing 2015 Conference, San Francisco, CA, 631-640.

Rayamajhi, D., Tamura, S., **Khosravi, M.,** Boulanger, R.W., Wilson, D. W., Ashford, S.A., Olgun, C.G. (2015). "Investigating Reinforcing Effects of Soil-Cement Columns in Liquefiable Sand Using Dynamic Centrifuge Tests", *The Deep Mixing 2015 Conference*, San Francisco, CA, 375-384.

Tamura, S., **Khosravi, M.,** Boulanger, R.W., Wilson, D. W., Olgun, C.G., Rayamajhi, D., Wang, Y. (2015). "Seismic response of Soft Clay Reinforced by Soil-Cement Grid Based on Dynamic Centrifuge Tests", *6th International Conference on Earthquake Geotechnical Engineering*, 1-4 November 2015, Christchurch, New Zealand.

A.3 Technical Reports

Khosravi, M., Wilson, D. W., Boulanger, R. W., Olgun, C. G., Tamura, S., Wang, Y., Rayamajhi, D., (2015a). "1-M Radius Centrifuge Experiments: Seismic response of soft soil reinforced with soil-cement grid-Construction procedure", Network for Earthquake Engineering Simulation (distributor), Dataset.

Khosravi, M., Wilson, D. W., Boulanger, R. W., Olgun, C. G., Tamura, S., Wang, Y., (2015c). "Test MKH01: Dynamic Centrifuge Tests of Soft Clay Reinforced by Soil-Cement Grids", Network for Earthquake Engineering Simulation (distributor), Dataset.

Khosravi, M., Wilson, D. W., Boulanger, R. W., Olgun, C. G., Tamura, S., Wang, Y., (2015e). "Test MKH02: Dynamic Centrifuge Tests of Structures on Soft Clay Reinforced by Soil-Cement Grids", Network for Earthquake Engineering Simulation (distributor), Dataset.

Rayamajhi, D., Tamura, S., **Khosravi, M.,** Boulanger, R.W., Wilson, D., Ashford, S.A., and Olgun, C.G. (2014 c). "Reinforcing effects of soil-cement columns in liquefiable sand." Data Report, UCD/CGMDR-14/01, University of California, Davis, CA.

Appendix B: Supplement for the Chapter 4: Dynamic Centrifuge Tests of Soft Clay Reinforced by Soil-Cement Grids

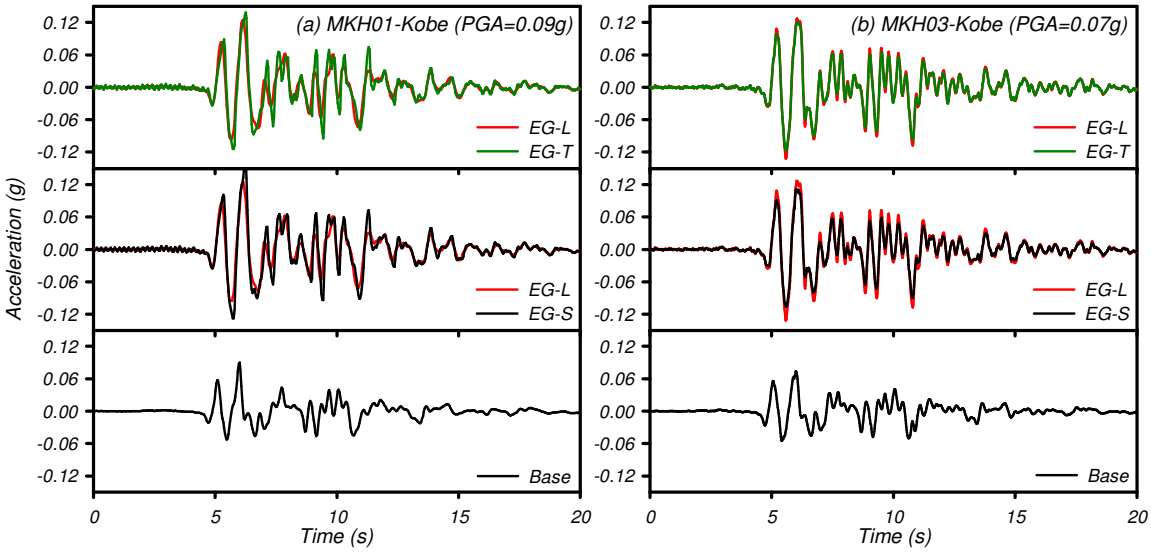

Figure B.S1. Recorded accelerations in the embedded grid sides of MKH01 (EG with A_r = 24%) and MKH03 (EG with A_r = 33%) during (a) Kobe motion with PBA = 0.09 g, (b) Kobe motion with PBA = 0.07 g.

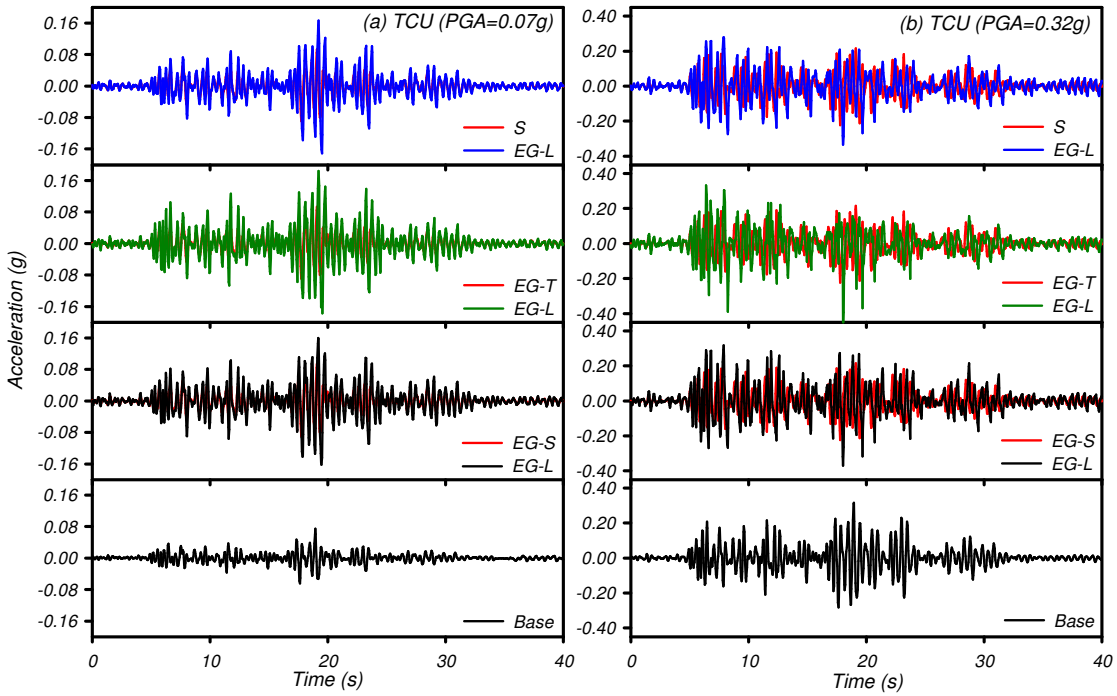

Figure B.S2. Recorded accelerations in the soil and embedded grid sides (EG with A_r = 24%) of MKH01 during (a) TCU motion with PBA = 0.07g, (b) TCU motion with PBA = 0.32g.

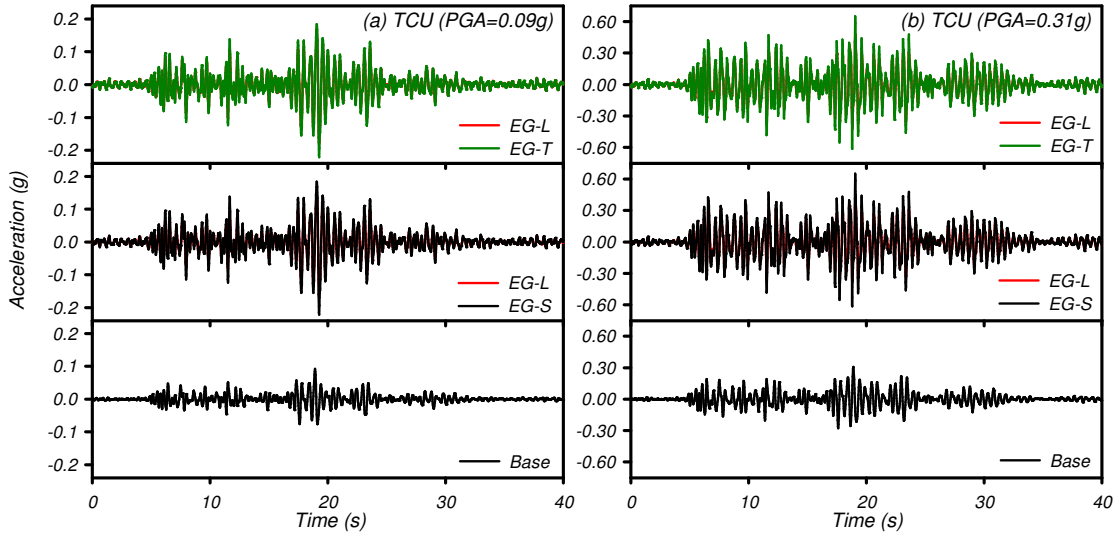

Figure B.S3. Recorded accelerations in the embedded grid side (EG with A_r = 33%) of MKH03 during (a) TCU motion with PBA = 0.09g, (b) TCU motion with PBA = 0.31g.

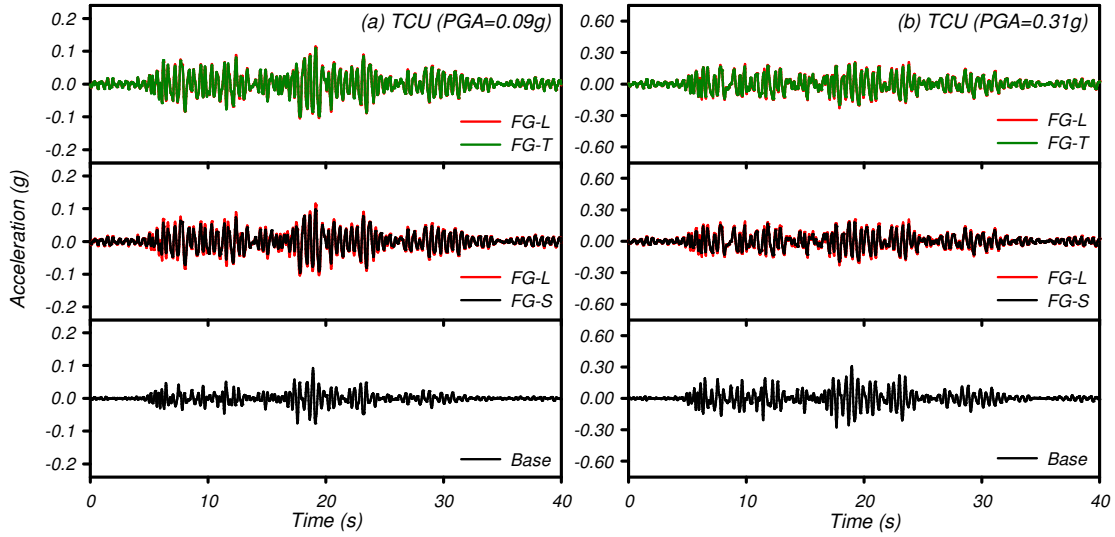

Figure B.S4. Recorded accelerations in the floating grid side (FG with A_r = 33%) of MKH03 during (a) TCU motion with PBA = 0.09g, (b) TCU motion with PBA = 0.31g.

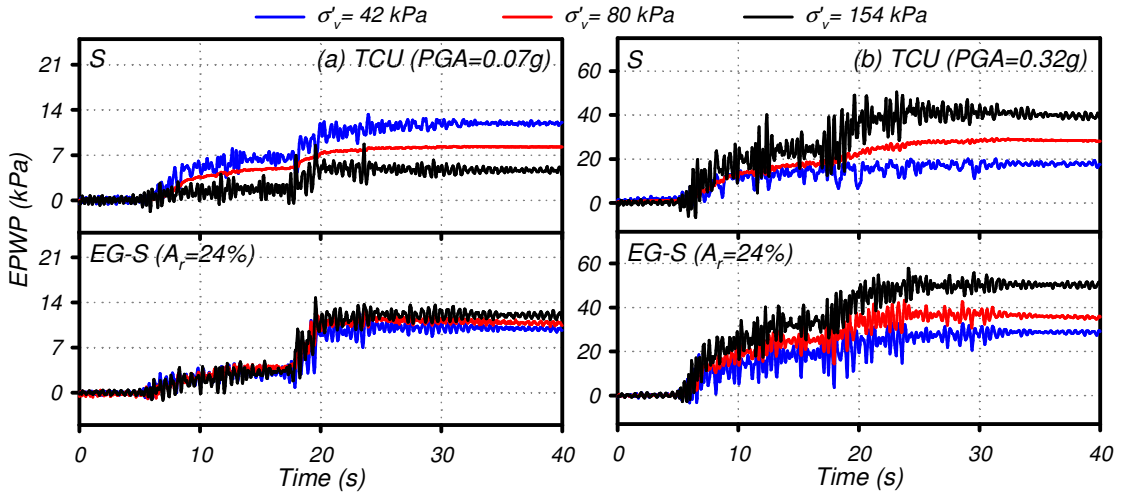

Figure B.S5. Excess pore water pressures in the soil and embedded grid sides (EG with A_r = 24%) of MKH01 during (a) TCU motion with PBA = 0.07g, (b) TCU motion with PBA = 0.32g.

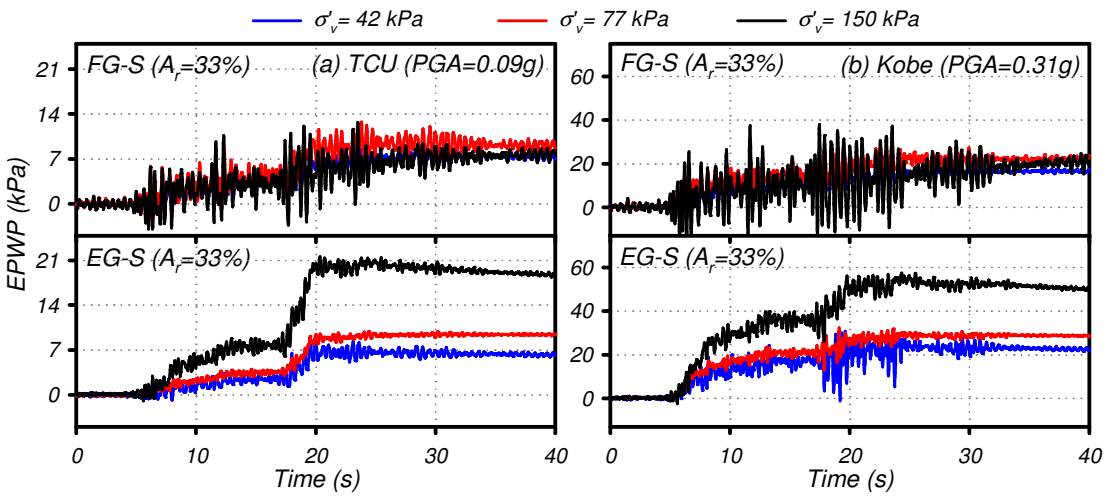

Figure B.S6. Excess pore water pressures in floating and embedded grid sides (FG and EG with A_r = 33%) of MKH03 during (a) TCU motion with PBA = 0.09g, (b) TCU motion with PBA = 0.31g.

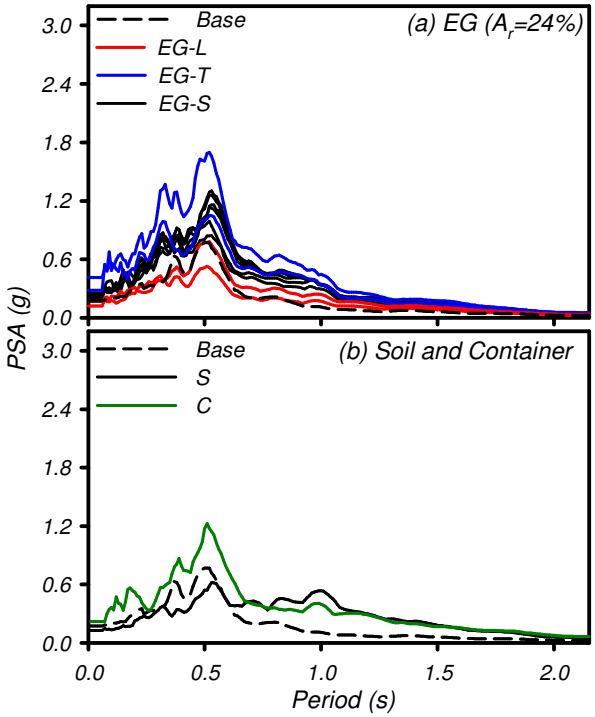

Figure B.S7. Pseudo spectral accelerations in MKH01 during TCU motion with PBA = 0.32g: (a) on the embedded grid side, (b) on the soil side and the container top ring

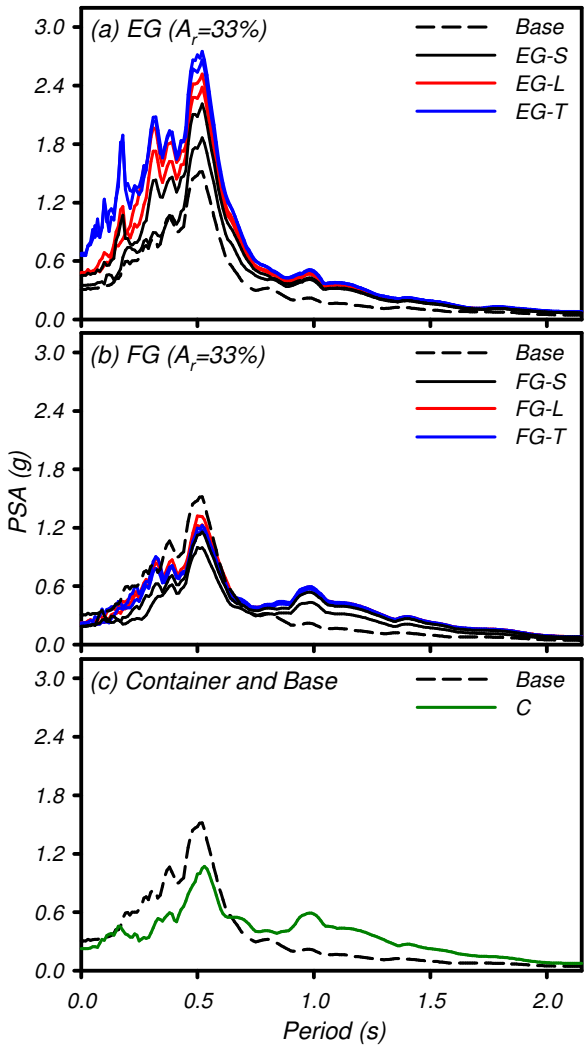

Figure B.S8. Pseudo spectral accelerations in MKH03 during TCU motion with PBA = 0.31g: (a) on the embedded grid side, (b) on the floating grid side, and (c) on the container top ring and base

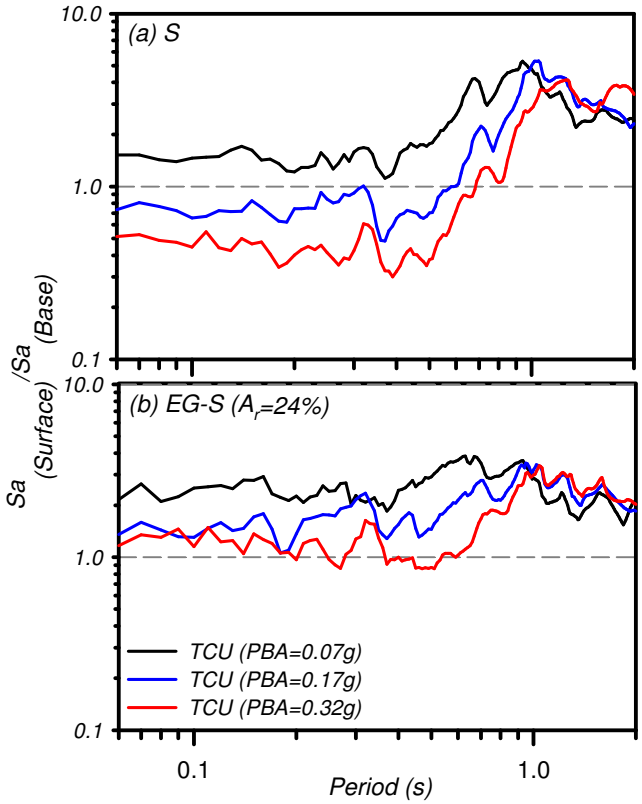

Figure B.S9. Pseudo spectral amplification ratios between the ground surface and the container base in MKH01 during TCU motions with PBA of 0.07g, 0.17g, and 0.32g: (a) on the soil side, (b) on the soil inside the embedded grid (EG with A_r = 24%)

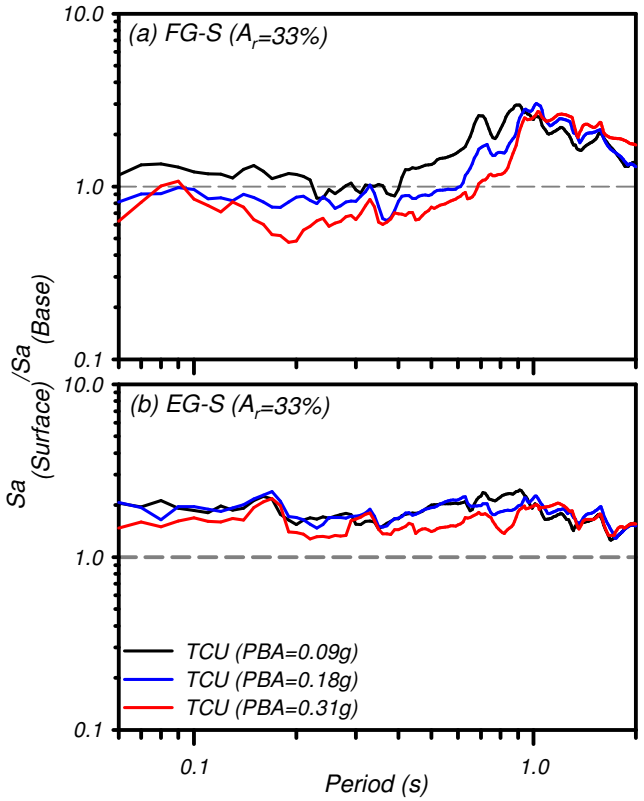

Figure B.S10. Pseudo spectral amplification ratios between the ground surface and the container base in MKH03 during TCU motions with PBA of 0.09g, 0.18g, and 0.31g: (a) on the soil inside the floating grid (FG with A_r = 33%), (b) on the soil inside the embedded grid (EG with A_r = 33%)

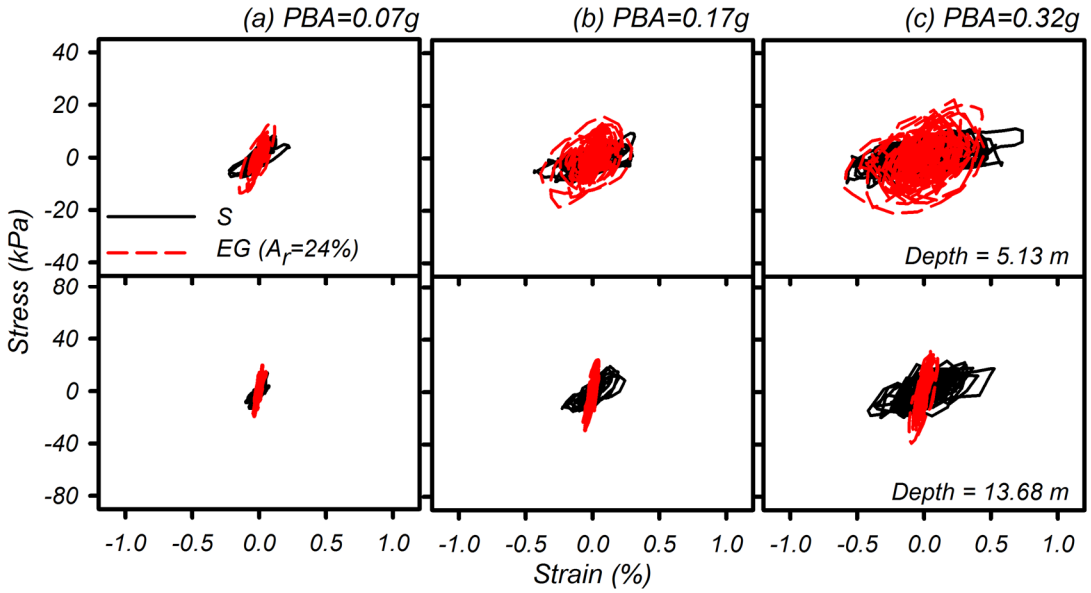

Figure B.S11. Average shear stress versus shear strain responses at depths of 5.1 and 13.7 m in the soil and embedded grid of MKH01 during TCU motions with: (a) PBA = 0.07g, (b) PBA = 0.17g, (c) PBA = 0.32g.

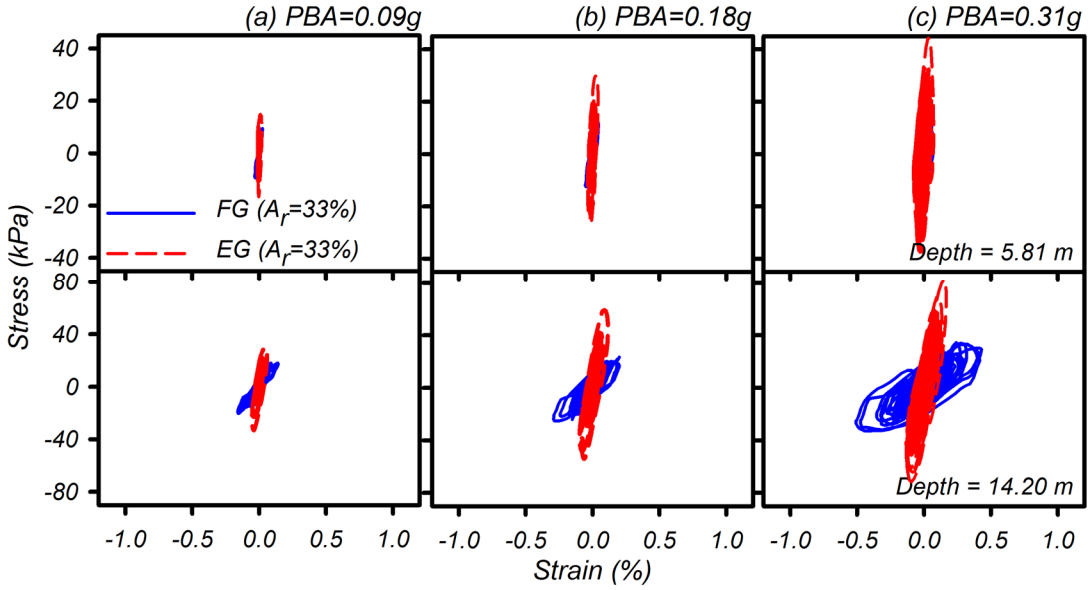

Figure B.S12. Average shear stress versus shear strain responses at depths of 5.8 and 14.2 m on the floating and embedded grid sides of MKH03 during TCU motions with: (a) PBA = 0.09g, (b) PBA = 0.18g, (c) PBA = 0.31g.

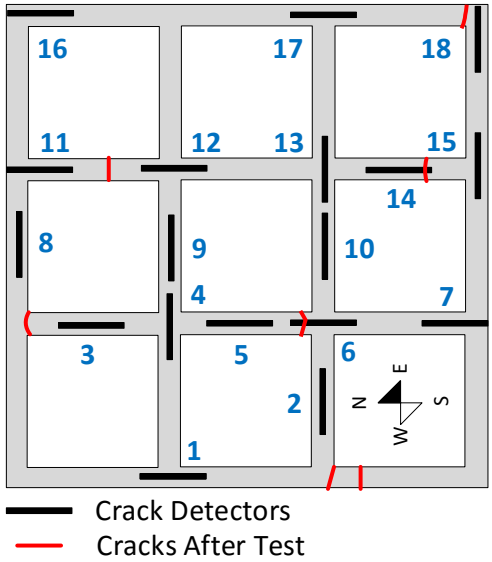

Figure B.S13. Schematic of the embedded grid in MKH01 with the location of crack detecting sensors and any visible post-testing cracks

Appendix C: Supplement for the chapter 5 Dynamic Centrifuge Tests of Structures with Shallow Foundations on Soft Clay Reinforced by Soil-Cement Grids

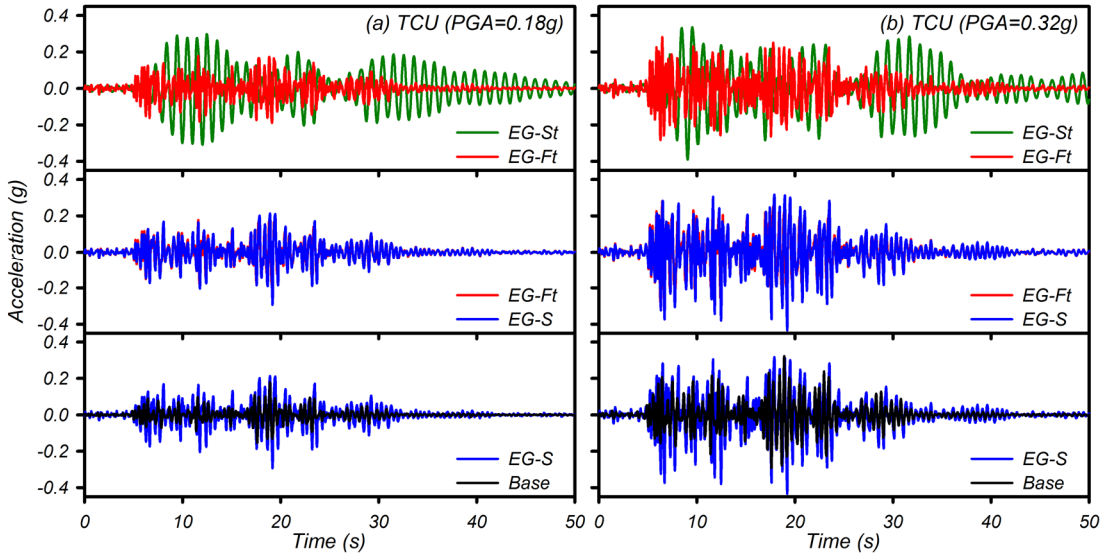

Figure C.S1. Recorded accelerations on the embedded grid and structure (EG with A_r = 24%) of MKH02 during (a) TCU motion with PBA = 0.18g; (b) TCU motion with PBA = 0.32g.

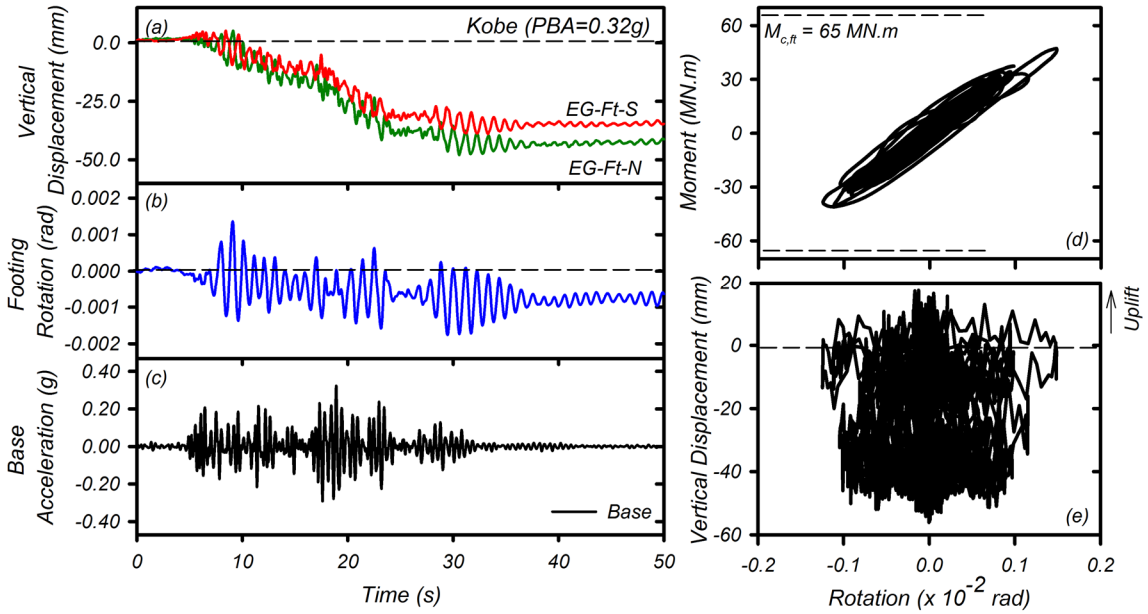

Figure C.S2. Dynamic response of the structure located on the embedded grid (EG with A_r = 24%) of MKH02 during TCU motion with PBA = 0.32 g: (a) footing settlement time history; (b) footing rotation time history; (c) base acceleration time history; (d) footing moment versus rotation; and (e) footing vertical displacement versus rotation.

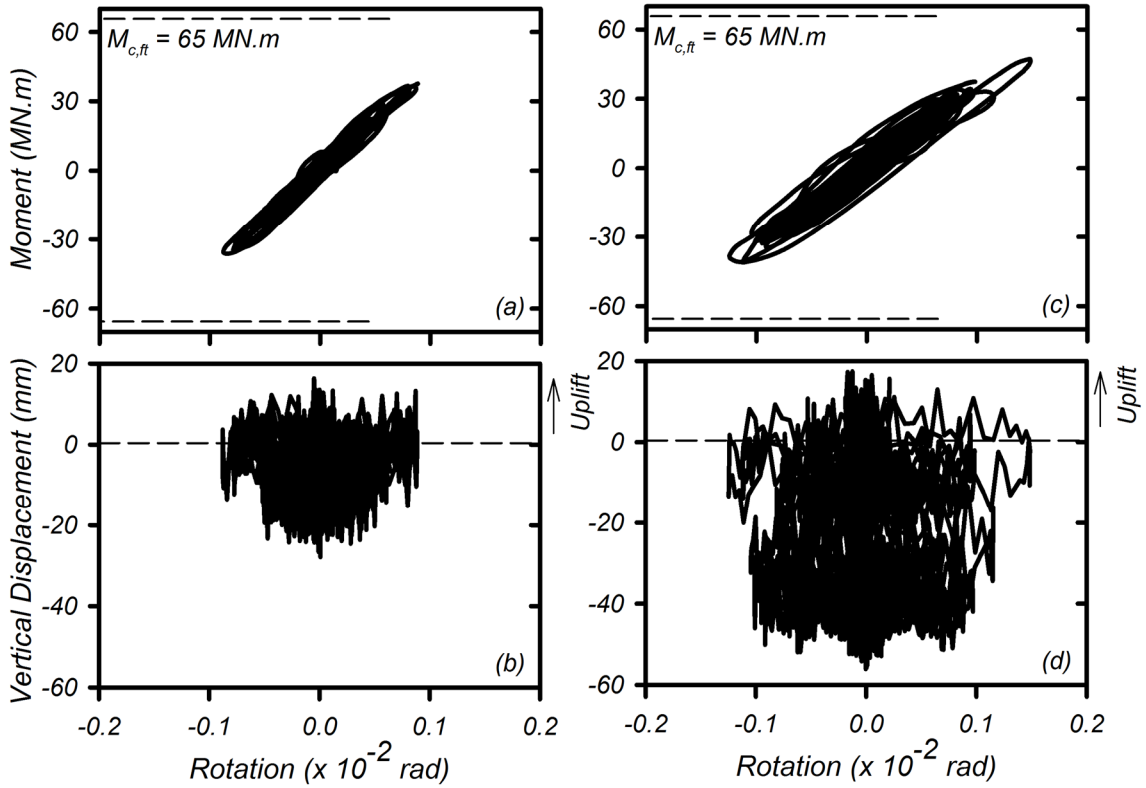

Figure C.S3. Dynamic response of the structure located on the grids of MKH04 during TCU motion with PBA = 0.33g, (a) the embedded grid (EG with A_r = 33%); (b) the floating grid (FG with A_r = 33%).

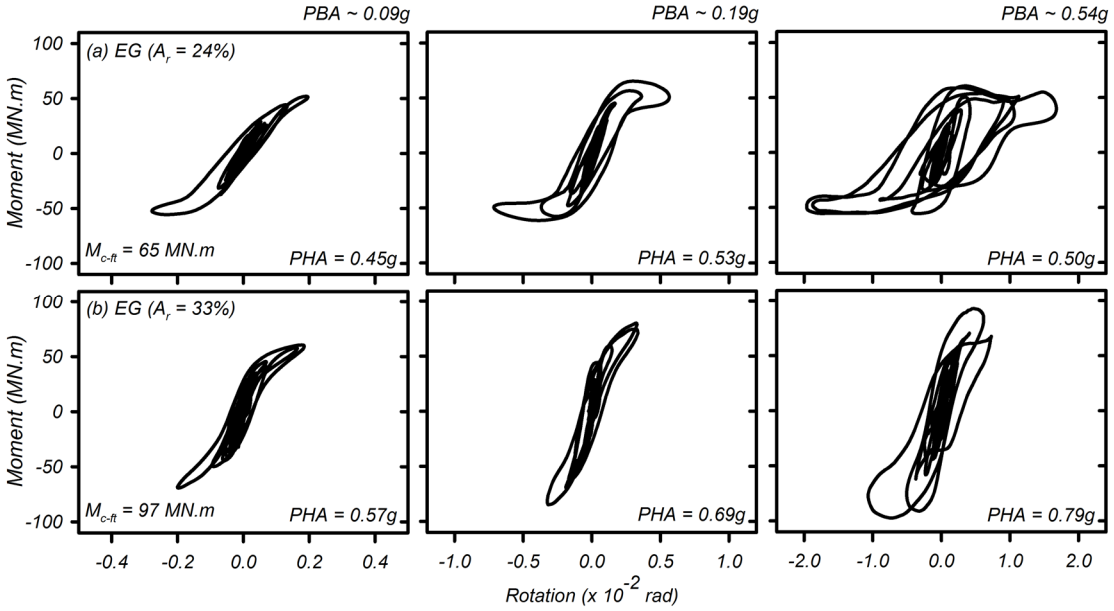

Figure C.S4. Response of SODF structure on the embedded grids during Kobe motions, (a) Embedded Grid with A_r = 24%; (b) Embedded Grid with A_r = 33%.

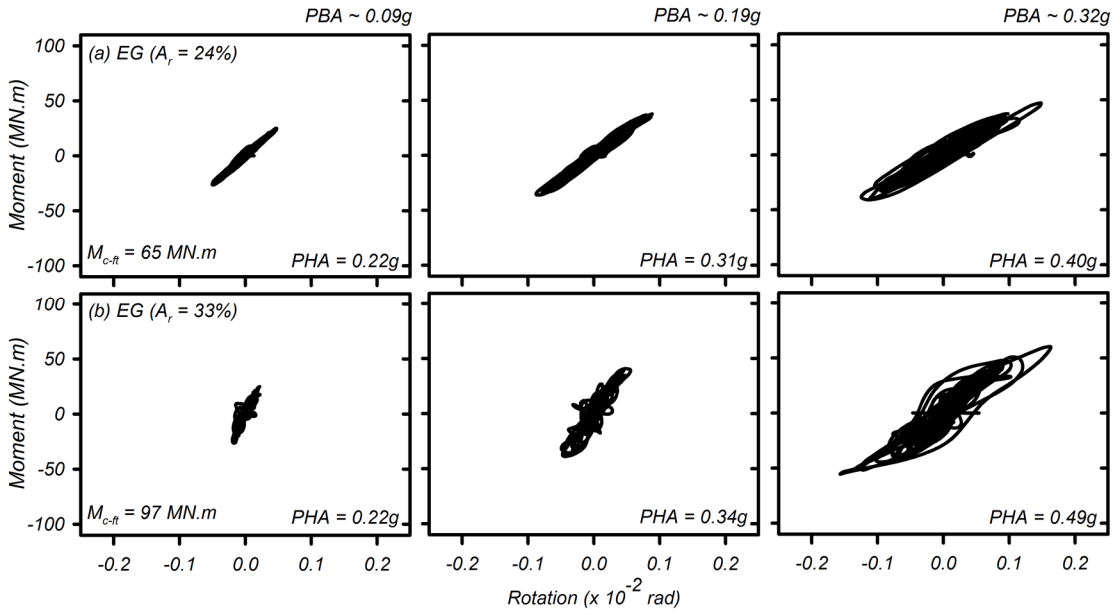

Figure C.S5. Response of SODF structure on the embedded grids during TCU motions, (a) Embedded Grid with A_r = 24%; (b) Embedded Grid with A_r = 33%.